The Fluid Flow in an Open Wet Clutch

Zur Erlangung des akademischen Grades eines
Doktors der Ingenieurwissenschaften (Dr.-Ing.)
von der KIT-Fakultät für Maschinenbau
des Karlsruher Instituts für Technologie (KIT)

genehmigte

Dissertation

von

M.Sc. Robin Leister

Tag der mündlichen Prüfung:	13.12.2022
Hauptreferentin:	Prof. Dr.-Ing. Bettina Frohnapfel
Korreferent:	Prof. Dr.-Ing. Christian Cierpka

Abstract

The present work improves the fundamental understanding of the fluid flow that passes through an open wet clutch, and its contribution to the generated drag torque and the physical process of aeration. A set of governing analytical equations is revealed from in-depth theoretical considerations, which describe the general cause-effect relations of the flow. Subsequent conversion into dimensionless quantities broadens their applicational use and allows to formulate simple – yet meaningful – interdependencies. Special emphasis is put on the role of an appropriate experimental measurement technique for such a gap-flow scenario, where recorded 3C-velocity fields allow a topology analysis within a grooved disk and uncover formerly hidden cause-effect relations in smooth and grooved disk regions. In particular, a novel Laser Doppler Velocimetry profile sensor (LDV-PS) is used to successfully measure angular-resolved 1D3C-information along the entire circumference. Circumferentially-filtered wall shear stress information is successfully extracted from the data through purpose-built data processing routines. Further advanced post-processing significantly reduces the LDV-PS inherent interplay of velocity and location-estimation uncertainty. To gain deeper insights into the unknown intra-groove phenomena the second technique Defocusing Particle Tracking Velocimetry (DPTV) is successfully applied to (locally) extract precise vortex information and fine-resolved wall shear stress values. Metrological insights are generated with the introduction of a new detection strategy and the proven flexibility of DPTV, which makes comprehensive magnification and location-accuracy studies possible. The work is completed with a flow analysis along the entire radial region of interest, and the consideration of a more complex groove geometry.

Kurzfassung

Die vorliegende Arbeit verbessert das grundlegende Verständnis der Strömung einer offenen nasslaufenden Lamellenkupplung und trägt zum Erkenntnisgewinn des Beitrags des generierten Schleppmoments und des physikalischen Prozesses des Lufteinzuges bei. Auf der Grundlage eingehender theoretischer Überlegungen wird ein Satz maßgeblicher analytischer Gleichungen aufgestellt, die die allgemeinen Ursache-Wirkungs-Beziehungen der Strömung beschreiben. Die anschließende Umrechnung in dimensionslose Kennzahlen erweitert deren Anwendungsmöglichkeiten und formuliert einfache, aber aussagekräftige Zusammenhänge. Besonderes Augenmerk wird auf die Rolle einer geeigneten experimentellen Messtechnik für ein solches Spaltströmungsszenario gelegt, wobei die Aufzeichnung von 3C-Geschwindigkeitsfeldern eine Topologieanalyse innerhalb einer genuteten Lamelle ermöglicht und bisher verborgene Ursache-Wirkungs-Beziehungen in glatten und genuteten Lamellen aufdeckt. Insbesondere wird ein neuartiger Laser-Doppler-Velocimetry-Profilsensor (LDV-PS) eingesetzt, um erfolgreich winkelaufgelöste 1D3C-Informationen entlang des gesamten Umfangs zu messen. Aus den Daten werden mit Hilfe spezieller Datenverarbeitungsroutinen erfolgreich in Umfangsrichtung-gefilterte Informationen über die Wandschubspannung extrahiert. Weitere fortschrittliche Auswerteroutinen reduzieren die mit LDV-PS verbundenen Unsicherheiten bei der Geschwindigkeits- und Ortsbestimmung erheblich. Um tiefere Einblicke in die unbekannten Phänomene innerhalb der Nut zu erhalten, wird die zweite Technik, Defocusing Particle Tracking Velocimetry (DPTV), erfolgreich eingesetzt, um (lokal) präzise Wirbelinformationen und fein aufgelöste Wandschubspannungswerte zu extrahieren. Durch die Einführung einer neuen Detektionsstrategie und die gezeigte Flexibilität von

DPTV werden messtechnische Erkenntnisse gewonnen, so dass umfangreiche Vergrößerungs- und Ortsgenauigkeitsstudien ermöglicht werden. Die Arbeit schließt mit einer Strömungsanalyse entlang des gesamten radialen Bereichs und der Berücksichtigung einer komplexeren Nutgeometrie.

Acknowledgements

At this point I would like to take the opportunity to express my appreciation and thankfulness to all the people who helped me with their support and patience on the way towards my PhD. First of all I want to deeply thank Bettina Frohnapfel for the opportunity to write the thesis in her group under her guidance. Thanks for your input and trust, your positive attitude and the fact that your door is always open (virtually and physically). Furthermore I would like to express my gratitude to Christian Cierpka for the examination of the thesis and your time and thoroughly studies of the present manuscript. I'm deeply thankful to Jochen Kriegseis who acted as my direct supervisor and introduced me not only to all laser-based techniques, but guided and helped me throughout the entire time. I am really thankful for all your time and patience enjoyed the numerous discussions which grew continuously in complexity over the last years.

I want to thank Thomas Fuchs for his input. I always enjoyed the calls we had and the inspiration you gave me. Your influence to the success of my PhD could not be underestimated. Thanks for your time and your guidance along my journey. Additionally, I'm really thankful for the measurement know-how and time Philipp Mattern invested in me and my first DPTV study.

I'm grateful to Davide Gatti and Alexander Stroh who helped me with the analytical and numerical analysis. It was always joyful to work with you. Thank you Amir Najafi for your patience with me throughout my first insights into the theoretical treatment and modeling. I really enjoyed my time at ISTM and I am grateful to all employees who enriched this time. Thank you to the members of the workshop Daniel Kissenkötter,

Heiko Bendler, Marcel Stotz, Michael Abramov and Otto Vorreiter. And thank you to my direct colleagues Andrea, Andrea, Annika, Anna, Arjun, Christian, Daniel, David, David, Erik, Francesco, Franco, Frieder, Georg, Jacopo, Joachim, Jiasheng, Jonathan, Karin, Kay, Lars, Marc, Max, Nils, Nima, Pourya, Sahba, Saskia, Sebastian, Sibela, Steffen, Tobias and Vishnu. I was and still am fascinated by the working environment you all created at ISTM. I learned alot from you throughout the entire time.

Finally I want express my deep gratitude to my parents Sabine and Reinhard and my twin brother Jonas. Thanks for all the education and passing on the values you can't learn at university. Thank you to my wife Carolin. I'm truthful happy to have you on my side. Thanks for all your love, patience and unconditional support and the encouragement throughout the entire time. This wouldn't be possible without you!

Contents

Abstract . . . . **i**

Kurzfassung . . . . **iii**

Acknowledgements . . . . **v**

1 Introduction **1**
1.1 Motivation 2
1.2 Research objectives and outline 4

2 Fundamentals **7**
2.1 Governing equations of fluid mechanics 7
2.2 Open wet clutch 9
2.2.1 Characteristics of an open wet clutch 10
2.2.2 Analytical description of gap flows 12
2.2.3 Experimental and numerical efforts 15
2.3 Optical measurement techniques for gap flow scenarios . . 16
2.3.1 Laser Doppler Velocimetry Profile Sensor 17
2.3.2 Defocusing Particle Tracking Velocimetry 21

3 Analytical consideration and dimensionless description . . **31**
3.1 Analytical derivation of velocities 31
3.1.1 Simplifications of the Navier–Stokes equations . . . 31
3.1.2 Circumferential and radial velocity results 39
3.2 Formulation of dimensionless quantities 42
3.2.1 Drag torque 43
3.2.2 Aeration condition 43

3.2.3 Benefits of dimensionless approach – the way to a direct comparison 45
3.3 Effect of grooves on aeration onset 49
3.4 Effect of grooves on the flow field 53
3.5 Concluding remarks (regarding the analytical and dimensionless consideration) 56

4 Laser Doppler Velocimetry Profile Sensor - angular-resolved experimental approach 59
4.1 Experimental procedure 59
4.1.1 Measurement principle 60
4.1.2 Experimental set-up and test rig variants 63
4.1.3 Evaluation of the third velocity component 65
4.2 Results 68
4.2.1 Uncertainty considerations for velocity, space and angle 68
4.2.2 Expected flow topology 73
4.2.3 Clutch flow measurements 75
4.2.4 Wall-shear stress determination 79
4.3 Concluding remarks (regarding LDV profile sensor technology) 82

5 Defocusing Particle Tracking Velocimetry - intra-groove analysis 85
5.1 Set-up specific background on Defocusing Particle Tracking Velocimetry 85
5.2 Experimental procedure 88
5.3 Results 92
5.3.1 Comparative particle image detection analysis 92
5.3.2 Clutch flow topology 99
5.3.3 Wall shear stress at stator 106
5.4 Concluding remarks (regarding DPTV) 109

6 Experimental fluid flow analysis - broader insights and understanding 111
6.1 Accuracy considerations and magnification range of DPTV 112

6.1.1 Measurement principle . . . 112
6.1.2 Experimental set-up . . . 113
6.1.3 Optical characteristics . . . 114
6.2 Results . . . 117
6.2.1 Particle location uncertainty . . . 117
6.2.2 Fluid mechanic accuracy considerations . . . 120
6.3 Groove geometry analysis . . . 122
6.3.1 Radial groove at the mean radius R_m . . . 122
6.3.2 Detailed groove analysis . . . 124
6.4 Concluding remarks (regarding the broader analysis) . . . 129

7 Conclusions and outlook . . . 131

Acronyms and symbols . . . 139

List of Figures . . . 147

List of Tables . . . 157

List of Publications . . . 159
Journal articles . . . 159
Conference contributions . . . 160

Bibliography . . . 163

1 Introduction

Fluid dynamics play a huge role in our everyday life. From large-scale flows in nature and the creation of weather phenomena to the smallest flow structures in sub-millimeter flows – for example some energy applications – fluid phenomena are ubiquitous and often form the predominant influence. The systematic and targeted use of energy led indisputable to wealth, innovation and progress throughout the last centuries. Plenty of decisive innovation steps direct the way to the nowadays existence of individual and consumer transport. Caused by the finite availability of energy, one rising issue is the effort to increase the energy efficiency. One major goal of the present and upcoming generations is the reduction and ultimately prevention of fossil energy consumption, since the impact on environment and nature due to its negative repercussions is locally and globally too strong to maintain on a permanent level [79, 80]. Therefore, the European Union together with the rest of the world agreed to a zero net emission of green house gases and a limitation of temperature rise in mean global temperature below 2°C, compared to pre-industrial levels and pursue the efforts to limit the temperature increase to 1.5°C [98]. Current research in all transportation sectors, like vehicles, airplanes or trains led to significant reduction of energy and thus mostly to an emission decrease of CO_2, which acts as most crucial greenhouse gas.

One trend of the recent years, which took up the aim of abating energy and material use, is the miniaturization of energy application and power trains of individual consumer transport, since it saves space, material and weight. Here, also fluid-carrying and tribological systems are taken under revision. This development leads to the fact that the dimensions of the components likewise become smaller and thus the dimensions of the acting principles of energy transfer may be located in the micro or sub-millimeter range. In this situation a micro flow is present, which is challenging to characterize with conventional flow velocimetry techniques. If a deeper insight in the acting principles is favorable, new measurement techniques need to be adapted. A flow control in micro flows consequently is in need of appropriate measurement technique, when experimental approaches should be part of the process.

1.1 Motivation

One promising structural element in the transport section, where all the previous mentioned trends are applicable, is the wet clutch. The continuous development of new hybrid and battery-driven concepts in automotive industry led to a large variety of new energy-saving strategies. One of the strategies is the optimization of the idling behavior of a wet clutch, which is presently installed in the majority of higher-class automobiles and is also nowadays often used for hybrid concepts and full-electric driven vehicle [106]. In the applied cases, it serves as structural element to transmit the torque between the engine and the wheels. In open state condition, as shown in Figure 1.1, a sub-millimeter gap forms between the disks of the drive and output unit, where a speed difference of the disks is present. This mentioned difference leads – combined with the cooling oil, which is present between the disks – to a considerable high wall-shear stress. The wall-shear stress in turn sums up to a so-called *drag torque*, which was described by LLOYD in 1974 [56]. When comparing this torque loss to the overall engine power of an automobile, it can reach a single-digit percentage ratio of loss as outlined by HOLZER [37]. Consequently, it was tried to be minimized in the following years by various research departments. Soon the problem was also adopted by applied scientific institutes and universities. The first attempts to understand the cause-effect relations and to describe the flow in general were done by e.g. KATO *et al.* [46] and

Kitabayashi *et al.* [47]. From an academic point of view, the flow can be classified as rotating disk flow with a sub-millimeter gap spacing. Since at a certain speed difference air enters the gap, caused by a fixed volumetric oil flow rate, the flow might be considered as single or two-phase flow. While somewhat contradictory approaches coexist to describe the fluid flow in an open wet clutch with analytical means [62], clutch manufacturer proved experimentally, that the introduction of surface grooves on one of the disks has a positive influence. Various different groove shapes and geometries were tested and proven to have a positive impact towards a lower drag torque [22, 42, 62, 83]. The most common method to evaluate the quantitative success of a measure are torque measurements at the output shaft, which are up-to-now the only quantification tool. However, this method serves as integral measurement technique and thus limits the elaboration of precise cause-effect relationships. Since the occurring quantity is caused by the oil, a fluid-related analysis might be beneficial to be taken into consideration.

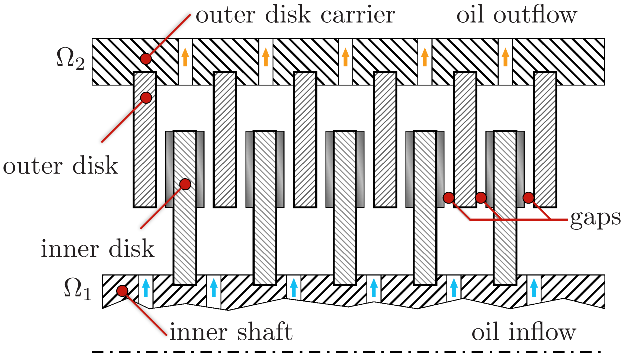

Figure 1.1: Scheme of a multi-disk wet clutch in idling state.

A recourse to already existing generic examinations of rotor-stator configurations (such as [49, 51]) can, however, only act as a starting point, due to the sub-millimeter spacing, the complex groove geometry and the fact that the circumferential flow is superimposed by a volumetric flow rate, which originates from the cooling oil, passing the clutch, as shown in Figure 1.1. All these factors limit a direct comparison strongly, if not at all completely, when searching for quantitative comparisons that already exist in literature.

A precise fluid flow analysis appears to be difficult, due to a complex geometric design, which negate a sole analytical consideration. The latter, however, can serve as starting point, since an in-depth fluid mechanic analysis and a broader way of description on the basis of dimensionless numbers is still pending for the flow in an open wet clutch. A classical and established experimental approach, which serves as another option to capture the flow velocity in the gap is limited by the sub-millimeter spacing and a restricted optical access. Additionally, the introduction of groove patterns on one disk adds complexity, since the flow topology and with this the expected wall shear stress is influenced. Numerical methods are in need of a precise definition of the boundary conditions, which is also challenging without experimental proof and an occurring two-phase flow in the gap. Thus, new innovative approaches to describe and quantify the fluid flow in an open wet clutch are demanded to gain powerful insights into the cause-effect relations between the torque, the flow and the present groove geometry.

1.2 Research objectives and outline

The major objective of the present work is consequently to analyze the fluid flow in an open wet clutch. This is done by analytical and experimental means to reach a deeper understanding into the cause-effect relations of an open wet clutch flow. One main focus of the work is the adaption and evaluation of promising experimental methods. Two laser-based optical techniques are used to gain field and profile information of the flow, which allow a topological flow discussion. The major metrological objective is a quantified statement, which technique is suitable for such a sub-millimeter gap flow scenario.

These approaches together with the theoretical treatment are used to answer the following fluid mechanical and metrological questions.

1. Up to which complexity level are analytically derived solutions valuable for a precise description of the fluid flow in an open wet clutch? Is a quantitative statement possible at which this solution deviates from the real flow scenario?
2. Which dimensionless scaling variables are relevant for the flow? Can they lead to a more general drag torque description?
3. Which experimental measurement technique can be adapted and applied to the flow? Which technique is suitable for which level of consideration?
4. Building on the results of the prior questions, what fluid-related insights can be gained with the developed experimental techniques, which topological pattern can be detected when considering complex groove geometries?

The investigation of such complex questions is broken down into varying aspects, which are identified and solved consecutively. For the first question a derivation of an analytical solution of the Navier–Stokes equation in circumferential and radial direction is needed. This only can be reached by an order-of-magnitude analysis, where several simplifications and assumptions are met. The results can be transferred to a dimensionless frame of reference, so that the drag torque and the point of aeration yield two dimensionless scaling variables. The gap flow equations can additionally be used to formulate a way to consider grooves within the analytical frame of description. With these statements, the second question can be answered. This complex of topic is evaluated in Chapter 3 of the present work. For the third question two laser-based optical measurement techniques, which in theory qualify for a successful detection of a sub-millimeter gap flow, are thoroughly tested and adapted for the open wet clutch. Chapter 4 exemplifies the use of a Laser Doppler Velocimetry profile sensor (LDV-PS), while Chapter 5 makes use of the technique called Defocusing Particle Tracking Velocimetry (DPTV). With these techniques it is – potentially – possible to extract velocity fields and wall shear stress profiles from the fluid flow. The test rig is equipped with a radial grooved disk, which serves as object of demonstration for both experimental optical techniques. The last Chapter 6 extends the groove geometries and shows the corresponding major flow pattern, whereas the technique DPTV is extended to address more complex groove geometries through the use of an incident light procedure. In this examination, the insights gained throughout all previous findings are used to answer the fourth question.

In summary, this work provides valuable information about analytical description in a dimensionless frame-of-reference and allocate measurement tool know-how to address the open wet clutch flow with experimental means. For the first time, experimental velocity profile and field information in an open wet clutch are generated and deliver valuable information to drag torque and aeration research.

2 Fundamentals

The present chapter recapitulates the source of knowledge, that is needed for the following theoretical and experimental investigations. First the fundamentals of fluid mechanics are discussed, followed by the state of research for open wet clutches. The following sections give an overview of the used laser-based optical flow measurement techniques.

2.1 Governing equations of fluid mechanics

The fundamental equations of fluid motion used throughout this work are used to describe the physical behavior of the fluid passing the open wet clutch. To model this behavior appropriately with mathematical means the fluid is described with the fundamental equations of continuum mechanics, which are the conservation of mass and momentum [92]. These two equations imply various assumptions and simplifications, for instance the state of Newtonian fluid, which introduces the (constant) dynamic viscosity μ. Furthermore, the state of incompressibility is considered, which sets the material derivative of the density ρ to zero. These simplifications can be justified for the entire one-phase flow of an open wet clutch. The simplified equations can thus be written in symbol notation as

$$\nabla \cdot \boldsymbol{u} = 0 \tag{2.1}$$

for the conservation of mass and

$$\rho\left[\frac{\partial \boldsymbol{u}}{\partial t}+(\boldsymbol{u}\cdot\nabla)\,\boldsymbol{u}\right]=-\nabla p+\mu\nabla^2\boldsymbol{u}+\rho\boldsymbol{g} \tag{2.2}$$

for the incompressible Navier–Stokes equation (NSE), which originates from the conservation of momentum [92] in combination with the material law for Newtonian fluid. Here the three-dimensional velocity vector is described as $\boldsymbol{u}=(u_1,u_2,u_3)^{\mathsf{T}}{}_{\{x_1,x_2,x_3\}}=(u_r,u_\varphi,u_z)^{\mathsf{T}}{}_{\{r,\varphi,z\}}$. The pressure is stated as p and the gravitational body force is formulated as $\boldsymbol{g}$.

An additional key quantity for the description of the fluid is the vorticity $\boldsymbol{\omega}$, which reflects the intrinsic rotation of a fluid element and can be defined as (following the formulation of [82])

$$\boldsymbol{\omega}=\nabla\times\boldsymbol{u}. \tag{2.3}$$

A transport equation for the vorticity can be derived by applying the differential operator curl to the complete Navier–Stokes equation Eq. (2.2). This yields

$$\frac{\partial\boldsymbol{\omega}}{\partial t}+(\boldsymbol{u}\cdot\nabla)\,\boldsymbol{\omega}=(\boldsymbol{\omega}\cdot\nabla)\boldsymbol{u}+\nu\nabla^2\boldsymbol{\omega}. \tag{2.4}$$

Here the kinematic viscosity ν is used, which is calculated as $\mu=\nu\rho$. This equation is used due to its positive characteristic, that the body forces – if conservative, which means $\boldsymbol{g}=\nabla\boldsymbol{f}$ – and the pressure term are eliminated compared to the NSE. This fact is proven to be useful for the analytical derivation of the NSE solutions, as evaluated and applied later throughout this work.

Vortex detection – the Γ_1-criterion

Identification and evaluation of vortical structure takes advantage of a variety of existing approaches (see e.g. [30, 32]). Particularly for experimentally derived data the vortex identification criterion as introduced by GRAFTIEAUX *et al.* [29] is promising, since this method appears more robust against small scale turbulence or measurement errors, since it integrates over a certain area S. The criterion is called Γ_1 and is defined for a certain location P_1 as

$$\Gamma_1(P_1) = \frac{1}{S} \int_{M_1 \in S} \frac{(\mathrm{P_1M_1} \times u_\mathrm{m}) \cdot n_\mathrm{e}}{||\mathrm{P_1M_1}|| \cdot ||u_\mathrm{m}||} \, \mathrm{d}S = \frac{1}{S} \int_S \sin\left(\theta_{\mathrm{M_1}}\right) \mathrm{d}S, \qquad (2.5)$$

where M_1 is a point that lies within the considered surface S and n_e the unit vector normal to the measurement plane. $\theta_{\mathrm{M_1}}$ represents the angle between the velocity vector u_m and the radius vector $\mathrm{P_1M_1}$. As visible from this detection, the value is bounded by ± 1, which is reached at the center of the vortex. The concept uses the approach, that a vortex core has a non-zero angle when averaging over a certain area. While a constant free stream velocity would yield a value of $\Gamma_1 \approx 0$. A solid-body rotation would lead to a value of $\Gamma_1 \approx \pm 1$, depending on its direction of rotation.

2.2 Open wet clutch

A multi-disk wet clutch, as shown in Figure 1.1, is as structural element part of the power train for a friction-type connection and a transmission of torque. It is able to connect two drive trains, despite the speed difference and with complete torsional moment load. [64]

A wet clutch can operate in three states: (i) in idling condition, (ii) in switching phase or (iii) in the stage of torque transmission [65]. When the clutch operates in condition (i) a residual torque occurs, which is caused by the cooling oil and the speed difference. This so-called drag torque is usually considered as loss. The potential of a torque reduction was first discovered in R & D departments of industrial companies [56], but was soon adopted from universities and research institutes with applied scientific fields. [66]

2.2.1 Characteristics of an open wet clutch

From a fluid mechanic perspective the flow in an open wet clutch can be classified as gap flow in a rotor-stator configuration. Figure 2.1a shows a simplified open wet clutch model with only two disks. The cylindrical $\{r, \varphi, z\}$-coordinate system originates in the center of the stationary plate. Relevant geometric parameters are the inner and outer radius R_1 and R_2, respectively and the gap height h, which is commonly adjusted automatically in a wet clutch. The cooling oil flow Q is commonly centrally applied and leaves the area of consideration at the outer region as indicated with red arrows in the figure. As fluid properties appear the oil density ρ and the kinematic viscosity ν, where $\mu = \nu\rho$ is valid. When considering gravitational effects, g usually acts orthogonal to the z-component. As operating parameters the angular velocity Ω and the drag torque T_s are of interest for a closer consideration. Note that Ω has the unit [1/s]. Other also common variables are the frequency f [Hz] and the rotational speed n [rpm], which can be calculated with $n = f/60 = 2\pi\Omega/60$.

One substantial characteristic of an open wet clutch is the distribution of T_s along the angular velocity Ω. At lower rotational speeds the gap between the disks is completely filled with oil. Since the volumetric flow rate Q is a given quantity and normally adjusted to a constant value, the feeding capacity of the rotating disk, due to increasing centrifugal forces, exceeds the flow rate with increasing angular velocity. At this point surrounding air from outside the disks enters the system and leads to a sudden decline of the drag torque. Figure 2.1b shows the distribution of T_s along Ω, in a schematic diagram with the point of *aeration* highlighted. The single

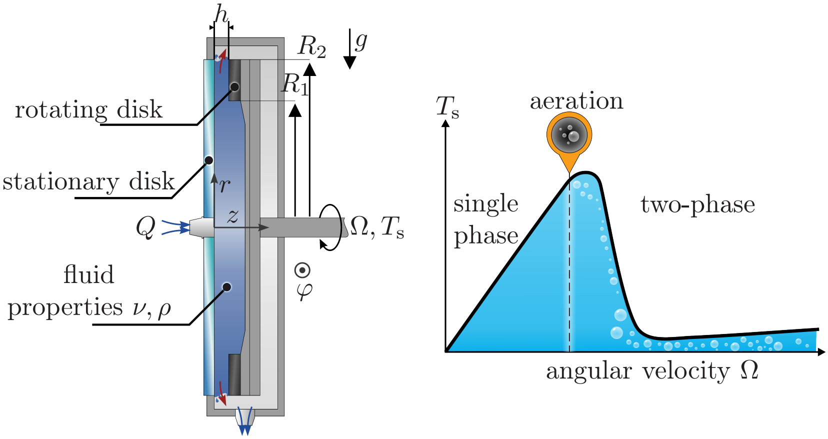
h
R_2
g
R_1
rotating disk
stationary disk
r
Q
z
Ω, T_s
fluid
properties ν, ρ
φ
T_s
aeration
single
phase
two-phase
angular velocity Ω

(a) **(b)**

Figure 2.1: (a) Scheme of an open wet clutch with the most important geometric parameters and the fluid properties. (b) Distribution of the drag torque T_s along the angular velocity Ω with the start of aeration highlighted.

phase has a characteristic linear increase up-to the start of aeration, where air enters the system, which lets the torque drop to a lower level. Consequently, the prediction and manipulation of the aeration onset to lower angular velocities is one essential drag torque minimization strategy.

Clutch manufacturers achieved this with the introduction of surface grooves on the rotor disk [65, 66]. Unfortunately, the choice of geometry parameters for the grooves mostly relies on experience, which renders the scaling of the involved parameters particularly difficult [LFMK21]. As a result, a variety of different groove patterns were introduced over the last years with partially seemingly arbitrary choices of groove designs. Figure 2.2 shows different designs, which are used in industrial applications. The introduction of surface grooves leads to a significantly earlier aeration process, but with the addition of a more complicated prediction and calculation process. While the gap flow can be described with analytical means, when no grooves are present, this becomes more complicated with a variety

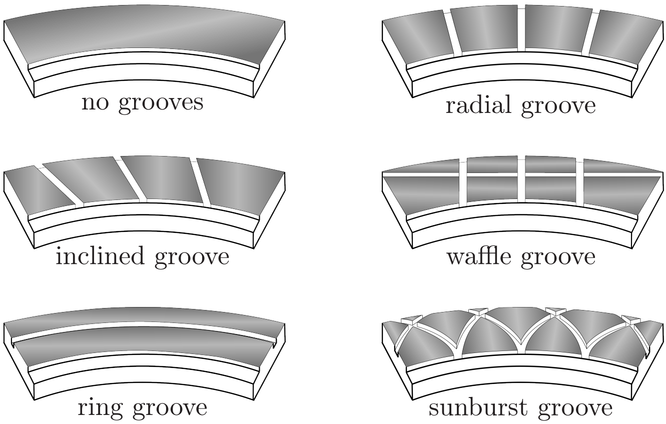

no grooves

radial groove

inclined groove

waffle groove

ring groove

sunburst groove

Figure 2.2: Different typical groove geometries as used in wet clutches.

of geometrically-complex groove patterns. At this point experimental or numerical considerations are advantageous to use. In the following the state-of-the-art is summarized for analytical, numerical and experimental investigations.

2.2.2 Analytical description of gap flows

A flow that runs through an open wet clutch can be treated as rotor-stator configuration. Depending on the gap height and the angular velocity, different kinds of flow regimes can exist depending on two dimensionless quantities [69], which are namely the gap ratio G and the rotational Reynolds number Re_r. They are expressed as:

$$G = \frac{h}{R}; \qquad Re_\mathrm{r} = \frac{\Omega R^2}{\nu}, \tag{2.6}$$

with R being a characteristic length scale for the radius. In case of an open wet clutch, this could be meaningfully represented by the outer radius R_2.

The other quantities are the same as used earlier in Figure 2.1a. DAILEY and NECE [19] proposed a graphical map, with calculational efforts to describe four different flow regimes and their corresponding demarcations and transitions as shown in Figure 2.3. The green region in this figure shows a typical open wet clutch application scenario, which only reaches Flow regime I. The flow in an open wet clutch under the absence of any grooves, can thus be described as laminar flow with merged boundary layers.

Various analytical efforts describing the drag torque and the start of aeration with analytical means were published the recent years.

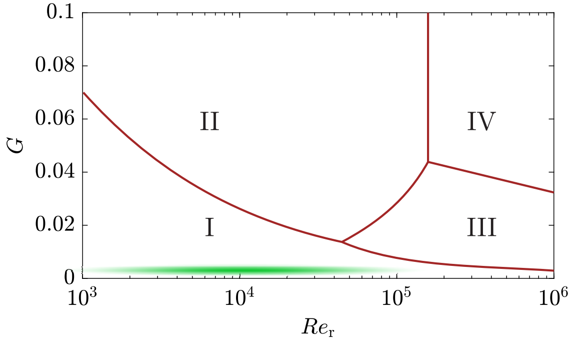

Figure 2.3: Four flow regimes as proposed by DAILY & NECE [19]. Flow regime I (laminar) and III (turbulent) have merged boundary layers, while regime II (laminar) and IV (turbulent) have separated boundary layers. The green region shows the application range for a typical open wet clutch flow. (Diagram adapted from [69].)

“One of the first suggestions was made by KATO *et al.* [46] who modified an approach of HASHIMOTO *et al.* [35], which originally was used for thrust bearings. This approach assumed a turbulent flow and calculated the drag torque with the help of an empirical formulation. YUAN *et al.* [105] used this approach to propose a model in consideration of an introduced shrinking of the oil film and a classification of the flow by use of dimensionless numbers. A turbulent flow in the gap seems however unlikely, due to a small gap ratio $G = h/R_2$ in the order of 10^{-3} and a moderate Reynolds number (see LAUNDER *et al.* [55] for more details on the classification of rotor-stator flows). KITABAYASHI *et al.* [47] assumed a laminar flow and used a laminar shear stress model to describe the drag torque characteristics in the single-phase region. While this model did not consider the onset of aeration, a new group of laminar models attempted to overcome this shortcoming. The basis of all these models is a laminar shear stress approach given as

$$\tau_{\varphi z} = \mu \frac{\partial u_\varphi}{\partial z}. \tag{2.7}$$

RAO [78] combined the shrinking of the oil film of YUAN *et al.* [105] and the laminar approach of KITABAYASHI *et al.* [47] and formed a laminar shear stress model, which is capable to predict the decrease of the drag torque in the two-phase region and provides a precise description of the laminar single-phase flow. Several new models with slightly different terms were published in the following years. HUANG *et al.* [41] modelled a hydroviscous drive with this concept and analysed the velocity profiles in the single-phase region. The model of IQBAL *et al.* [43, 44] considered the fluid and the mist contributing to the resulting torque. The most recent models and experimental validation were conducted by PAHLOVY *et al.* [70–72], where surface tension and high rotational speed differences were considered.

Due to the complex nature of two-phase flow, these models rely on a simplified description as basis for drag torque calculations, i.e. the concept of a shrinking radius, that varies from the outer to the inner radius. Although this concept is in good agreement with the measurements of the drag torque, the fluid mechanic conditions in the lubrication gap are not taken into account.

The development of an analytical model was accompanied by various attempts to measure and visualize the gap flow in a laboratory environment. The respective experimental studies however focused mainly on the generation of validation data for the analytical models. More recently, a systematic experimental investigation and a profound comparison of analytical models has been provided by NEUPERT *et al.* [62]." [LNG⁺20]

All recent literature agrees on the fact of a laminar shear-stress description and the drag torque T_s can thus be expressed as

$$T_\mathrm{s} = \iint\limits_A \mu \frac{\partial u_\varphi}{\partial z} r \,\mathrm{d}A = 2\pi\mu \int\limits_{R_1}^{R_2} \left(\frac{\Omega r}{h}\right) r^2 \,\mathrm{d}r = \frac{\pi\mu\Omega}{2\,h} \left({R_2}^4 - {R_1}^4\right). \quad (2.8)$$

2.2.3 Experimental and numerical efforts

Most experimental efforts focused on the alignment of experimental drag torque measurements with an analytical description of the problem. Different simplifications of wet clutches were used, with the aim to quantify relations and influences of e.g. disk wobbling, different oil supply strategies or geometrical dimensions. To analyze the fluid flow of an open wet clutch a simplified two-disk model with fixed gap height h is suitable, since a detailed cause-effect relationship concerning fluid-related quantities is possible and is not interfered by the various different possible influencing factors. The gained insights could then be transferred without any loss of generality to a more complex multi-disk clutch. TAKAGI *et al.* [94] measured the drag torque for a systematic variation of radial grooves and one circumferential groove and made a comparison with analytical models. The recent years such simplified experimental analysis were done in [62], where different groove designs such as waffle, radial and inclined groove patterns were tested and their corresponding drag torque distributions were analyzed. This study was complemented with a numerical analysis

during the subsequent year [61]. Numerical efforts in general mainly have the drag torque distribution as main result and thus aren't optimized for a precise fluid flow analysis. Groetsch *et al.* [33, 34] focused on a fast calculation method to contest against existing analytical models with the benefit of a more complex groove pattern, which provided some promising results. Some interesting experimental insights into the two-phase flow in a grooved rotor-stator system and the formulation of a dimensionless description of the imaging results were done by Wu *et al.* [101].
However, due to the focus on an integral value for both numerical and experimental investigations, a detailed cause-effect relationship is - up-to now - pending. The benefit of nowadays available measurement technique for micro flow applications might solve former limitations as encountered by current research efforts for open wet clutches. Thus, the following subchapter summarize potential measurement techniques for this kind of flow scenario and focuses on two laser-optical means, which were used in the present work.

2.3 Optical measurement techniques for gap flow scenarios

Gap flows with applicational use often exclude potential measurement techniques due to mandatory side conditions or limited optical access. Sub-millimeter flows especially require demanding technique, which is difficult – if not impossible – for intrusive measurement methods to provide. The flow of an open wet clutch in particular is in need of a solution to resolve the sub-millimeter spacing in combination with a resolution from the inner to the outer disk radius, which is in the order of $1-2$ centimeters.

To meet these requirements, two laser-optical techniques are presented, which act as candidating to describe the fluid flow in an open wet clutch with a sufficient precision. The first approach is called Laser Doppler Velocimetry Profile Sensor (LDV-PS) and the second Defocusing Particle

Tracking Velocimetry (DPTV). Both methods and their corresponding importance regarding the suitability for open wet clutch flows are explained in detail in the following from a theoretical perspective. The set-up-inherent details are later on recapitulated in Chapter 4 and 5 for LDV-PS and DPTV, respectively.

2.3.1 Laser Doppler Velocimetry Profile Sensor

The first measurement technique, which will be evaluated in detail in the present thesis, is based on the technique of Laser Doppler Velocimetry (LDV). So, the main principle is evaluated first, followed by the additional variant of a profile sensor.

Laser Doppler Velocimetry

LDV (also known as Laser Doppler Anemometry (LDA) from ancient Greek ἄνεμος - anemos: wind) is a non-contact, optical measurement technique, which measure the velocity of a seeded fluid by means of the Doppler effect. The light waves, which scatter on the seeding particles, need to be able to interfere and thus the light source must be able to emit polarized, monochromatic and coherent light. [3]
For this reason lasers are used for this technique. A first velocimeter based on the laser Doppler technique was introduced in 1964 by Yeh and Cummings [103]. The working principle of the most common configuration nowadays, which is referred from now on as classical LDV, is shown in Figure 2.4. The physical effect of a frequency variation, caused by a relative velocity between sender and receiver acts as main explanatory principle. [81]

In a general LDV measurement system two beams of one laser component are crossed in their beam waists forming an interference fringe pattern with parallel fringes of distance d_f in the intersection volume. Particles crossing

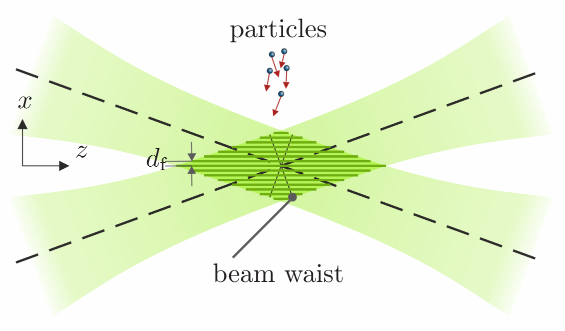

Figure 2.4: Intersection of two laser beams for the classical LDV principle with corresponding beam waists centered and a uniform spacing of the interference fringes.

the fringes in this volume scatter light at the Doppler frequency $f = u/d_\mathrm{f}$ where u is the particle-velocity component perpendicular to the fringes and d_f is the distance between two fringe maxima. To explain the occurrence of the Doppler effect, one has to consider each laser beam as separate sender. If a particle passes the measurement ellipsoid it scatters light from both partial beams. Caused by the relative velocity of the particle and the different directions the light originates, the light frequency that the particle receives is slightly shifted. The particle now acts as sender and scatters the light of both beams. The detector of the measurement technique receives an amalgamation of the scattered partial beams and is able to detect the beat frequency of the Doppler-shifted light. This frequency contains the velocity information perpendicular to the fringes. The received light signal is processed by means of a Fast Fourier Transformation and u can be determined. (An in-depth derivation can be found in [81, 96].)

Optical measurement techniques are generally classified by their ability of dimensions (D), they are able to extract and the velocity components (C) they could measure [36]. A classical LDV is a point method (zero dimensions) and is able to measure one velocity component (0D1C). Most commercially available LDV-systems combine two or three laser colors and are thus able to measure two (0D2C) or even three (0D3C) velocity components.

The exact dimensions of the beam diameter, the beam waist and the fringe distance d_f can be approximated with the Gaussian beam model and some trigonometric functions. The volume where particles are registered, usually referred to as measurement ellipsoid, is in the order of 10^{-4} m. The spatial resolution is limited by the size of the measurement ellipsoid. The laser has to be traversed to several positions to measure a velocity profile at accordingly limited spatial resolution. For macroscopic flows this resolution might be sufficient for most flows of interest. For micro flows, in contrast, the spatial filtering effect is often decisive.

The Profile Sensor function

To advance beyond these resolution drawbacks, the so-called LDV profile-sensor (LDV-PS) was introduced by Czarske [17, 18] as an extension of the conventional LDV, which has rapidly proven to be a valuable means to measure velocity profiles [11, 13] and furthermore derive acceleration information from the recorded signals [9]. Soon this technique was used for more challenging flow scenarios, such as the flow inside a hard disk drive model [90, 91] or the induced velocity of magnetic gradients on electro-deposition [53]. More recently, the LDV-PS approach was successfully applied for industry-near projects like a fuel-cell stack in [12].

With this LDV approach not only a precise velocity measurement but also a spatial detection within the measurement ellipsoid is possible (1D1C). The main difference to a conventional LDV set-up is the use of two overlapping fringe systems with different wavelengths, wherewith one velocity component and the position of particles passing through the measurement volume can be detected. The beam waist positions of the two laser systems are, therefore, shifted longitudinally away from the intersection point in opposite directions. Thus the fringes are diametrically opposed and the

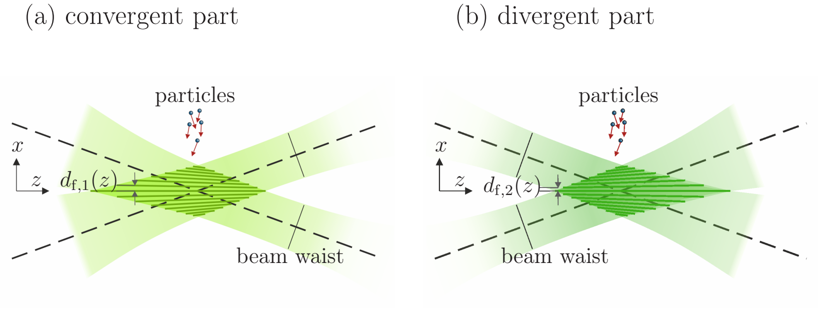

Figure 2.5: Intersection of two laser beams for both profile sensor components depicted separately ((a) convergent part and (b) divergent part) with coordinate system, beam waist positions and corresponding fringe distance as a function of z. At the profile sensor set-up these to components overlap.

fringe spacings $d_{\mathrm{f},i}$ for $i = 1, 2$ are a function of the z-position as shown in Figure 2.5 for both laser components separately. These two different colors, with their respective partial beam crossings are then overlapped.

The z-position of the particles can be determined by the quotient of the received Doppler frequencies f_i, which is given by

$$q(z) = \frac{f_2(z,u)}{f_1(z,u)} = \frac{u/d_{\mathrm{f},2}(z)}{u/d_{\mathrm{f},1}(z)} = \frac{d_{\mathrm{f},1}(z)}{d_{\mathrm{f},2}(z)}. \tag{2.9}$$

z can be found by means of a calibration function ϕ, which is achieved by different gradients of the fringe spacings $d_{\mathrm{f},i}$ over z of the two lasers by

$$z = \phi(q(z)). \tag{2.10}$$

Once the z-position of a particle is found the local fringe spacings $d_{\mathrm{f},i}$ and the resulting velocity u can be calculated. So, an integral part of the measurement process is a calibration procedure, which is normally done already by the manufacturer. However, it has to be considered that technically only velocities are measured. The z-position is only a derived quantity, which connects the corresponding accuracies.

This technique was already used for a generic open clutch model and proofed its suitability to such flow scenarios in [50], but this sensor version lacks of the acquisition of a second flow component and a bragg-shifted option, which makes the results limited for actual clutch flow topology discussions. A useful extension with two detection components and a successful demonstration of a bragg shifted version was recently published in [10]. There a back flow behind a droplet was effectively registered, which enhanced the velocity range to negative velocities, this is of particular interest, since a factual velocity of zero can't be detected due to the theoretical limitation of this method. Hence, the velocity-accuracy interplay in the low speed range is still a field, which hasn't been studied extensively, but might be of relevance for a variety of measurement applications.

2.3.2 Defocusing Particle Tracking Velocimetry

Defocusing Particle Tracking Velocimetry (DPTV) is a non-intrusive, indirect, optical measurement technique, which uses digital imaging as velocity extraction tool. Historically this technique developed among others from Particle Image Velocimetry (PIV), which constitutes nowadays one major experimental velocity measurement technique, due to its multifariousness and robustness throughout a broad field of applications from specific applicational questions to fundamental fluid mechanic research. Since its digital adaption from former analog, photographic version PIV generated the invention of various techniques and optimizations for different applications. Further information on PIV can be found e.g. in [2, 77]. Standard planar PIV with one camera is able to measure two dimensions and two velocity components (2D2C). Various other techniques have developed from this, some examples are Stereo PIV (2D3C) [75], Tomographic PIV (3D3C) [21], Holographic PIV (3D3C) [14, 28] or Micro PIV (2D2C) [58], among others. Detailed explanations of the underlying principles and a review of a broad range of PIV-techniques can be found in [77, 86].

When the velocity of a distinct particle is tracked, one speaks of Particle Tracking Velocimetry (PTV). Here also various techniques were developed e.g. 3D-PTV [57, 63], Astigmatism PTV [15, 45], Shake-the-Box [84, 85] and Defocusing PTV (DPTV) [99]. An overview of most of these PTV-techniques applied to micro fluidics can be found in CIERPKA and KÄHLER [14]. Whenever it is necessary to resolve small flow structures, that are in the order of the light sheet thickness or even smaller it is favorable to use PTV instead of PIV.

For most technical applications complex multi-angle camera perspectives are an additional hurdle, if at all applicable. Micro flows come with the complementary and inherent disadvantage of a small confined space with limited optical access and mostly a challenging calibration strategy for imaging velocimetry. For a precise extraction of meaningful velocity data via imaging optics in open wet clutches Defocusing Particle Tracking Velocimetry appears as promising technique for this kind of flow scenario, since it combines a robust but simple set-up, which has the potential to be used also in industrial environment with the power of a 3D3C velocity information in a single camera technique. The technique was introduced by WILLERT and GHARIB [99] as macroscopic defocusing approach. They used a three-pinhole mask in the aperture to generate three images of the same out-of-focus particle on the camera sensor, where the distance between the three images relate to the particle distance of the focal plane. The technique soon was adapted and developed by research groups specialized in micro applications like, Yoon and KIM [104] and PEREIRA *et al.* [73], for instance . The process of using the complete defocused image as estimate of the out-of-plane position was conducted by WU *et al.* [100]. Analogously, FUCHS *et al.* [25] determined the particle image geometry by analyzing the intensity distribution at its edges, where a fixed intensity value denoted the edge location. The main principle of this approach is extracting the depth position in the size of the defocused particle. Figure 2.6 shows this principle for two particles – one positioned at the focal plane and a second some distance away from the focal plane. The latter forms

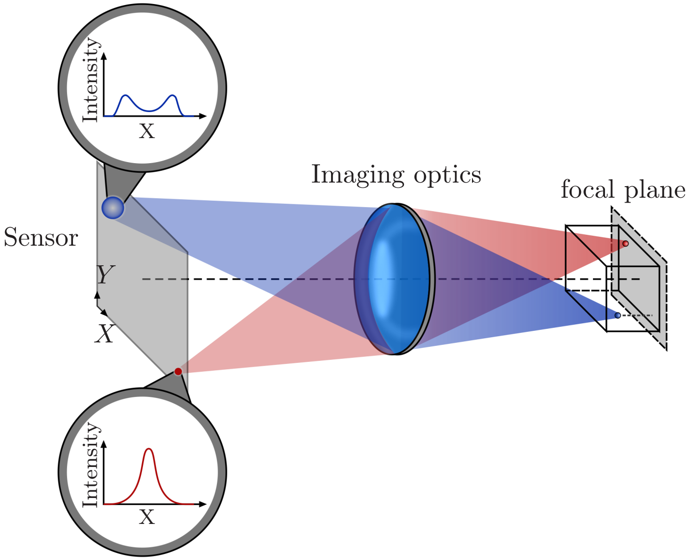

Figure 2.6: Scheme of defocusing explained with two particles. The red one is located at the focal plane and imaged sharp. The blue has a distinct distance to the focal plane and is imaged as out-of-focus particle image with a much lower peak intensity as shown in the diagrams.

an out-of-focus particle image on the sensor chip of the camera. Furthermore, the diameter of this image, in turn, contains the explicit distance information to the focal plane. Note, the intensity of the image might be several orders-of-magnitude lower, than compared to an in-focus image as the same amount of light is distributed across a substantially larger area on the camera chip.

"Olsen and Adrian [67] derived a mathematical description of the defocusing function under absence of optical aberration effects, which quantifies

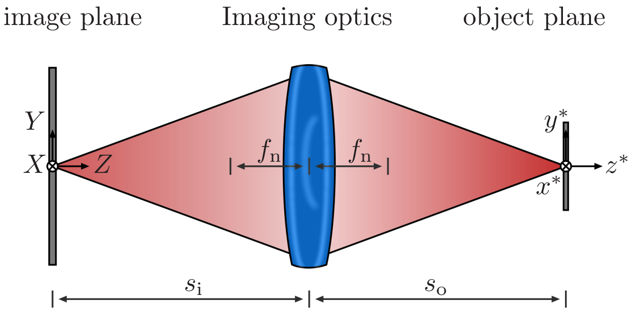

Figure 2.7: Overview of the optical geometry with image and object side coordinate system. Adapted from Olsen and Adrian [67].

the particle image diameter d_i in relation to the distance of the particle with the physical size (diameter) d_p to the focal plane as

$$d_\mathrm{i}{}^2 = \underbrace{M^2\, d_\mathrm{p}{}^2}_{\text{geometric image}} \underbrace{+\,5.95\,(M+1)^2\,\lambda^2 f_\#^2}_{\text{diffraction}} + \underbrace{\frac{M^2 z^{*2} D_\mathrm{a}{}^2}{(s_\mathrm{o}+z^*)^2}}_{\text{defocusing}}\,. \qquad (2.11)$$

The first term describes the geometric image with the magnification M. The second term exists due to the diffraction of light on the aperture of the camera, where λ appears as wave length of the light and $f_\#$ is the focal number of the objective lens. The factor of 5.95 is related to the first minimum of the Bessel function of the first kind, which is considered to model the intensity of the diffraction.” [LFMK21]

The third term is the relevant one for the defocusing. The occurring parameters are also shown in the imaging set-up as indicated in Figure 2.7. This term describes the diameter change on the image plane due to the distance z^* of the particle to the focal plane, where s_o additionally appears as the distance between the lens and the focal plane in the denominator.

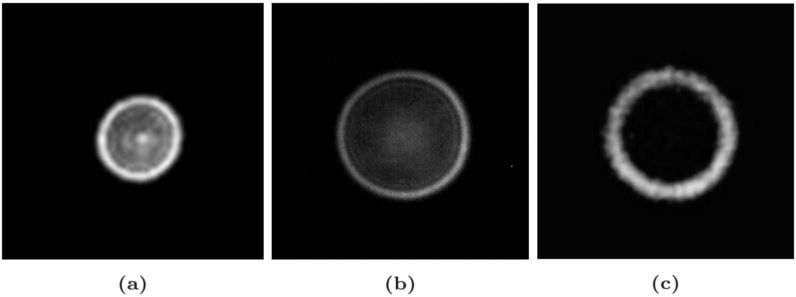

Figure 2.8: Raw images of defocused particles acquired with different focal lengths and lens types (a) 50 mm (b) 105 mm (c) Questar Longdistance microscope

“According to [67], $s_\mathrm{o} \gg z^*$ applies for any optical set-up such that the image diameter change can be approximated by

$$d_\mathrm{i}(z^*) \propto \left(\mathrm{const.} + {z^*}^2\right)^{1/2}. \tag{2.12}$$

When imaging the particles with sufficient distance Δz from the focal plane, the hyperbola can be approximated as a linear curve (see [26]), where the third term of the equation dominates.” [LFMK21]

Equation (2.12) can thus be simplified to

$$d_\mathrm{i}(z^*) \propto z^*. \tag{2.13}$$

Since each commercial lens has correcting-glass elements for minimizing a vast array of aberrations - inter alia, field cuveratURE, spherical aberration, comatic aberration - the exact intensity distribution relies on the lens and various further factors. A variety of different raw images of a defocused particle can be seen in Figure 2.8.

However, Equation (2.12) is not able to take aberrations into account, based on the simplifying nature of the assumptions met, which renders this equation to more of theoretical interest, since a direct calculation of the depth position is disabled. One means to extract a precise function for particle-location estimations is the use of pinhole matrices, which are illuminated from the back and imaged at a certain amount of different depth positions. The spherical light waves originating from the pinhole resembles the illumination of a particle with the same diameter (Babinet's principle). This technique requires to place a calibration target within the measurement domain, which is not feasible for most applicational flow scenarios with a lot of mandatory side conditions. For the present application an additional option is used, since the present open wet clutch is a wall-bounded flow with a known gap height h. The defocusing function is retroactively derived after the acquisition process while post-processing from the recorded displacements. Based on the no-slip conditions at the lower and upper boundary of the measurement volume the particle displacements at these positions are known quantities. With the help of the extracted diameters at these depth positions an extraction of the linear function can be conducted. An in-detail description of this so-called *in situ calibration procedure*, with a profound analysis of camera misalignment and field curvature compensation strategies can be found in [26].

For a general DPTV experiment a few more quantities are of need, which are explained in the following. These are partially relevant for LDA experiments as well.

Stokes number

All imaging techniques –as well as LDA-techniques – of single phase flow scenarios rely on the additive of particles, which reflect or scatter the light and are called tracer particles, since they aim to follow the movement of the fluid and can thus be traced with imaging technique. A mandatory condition to capture a precise estimate of the flow velocity is an adequate following behavior. Various flows demand different kind of tracer particles, consequently a large variety of different types were used in the past, such as: aerosols (such as oil droplets, DEHS), snow flakes [38], soap bubbles [39], woodchips [5] or fluorescent particles [48]. Small particles are beneficial for a precise following behavior, while larger particles scatter more light and are thus better visible with the imaging techniques. When designing an experiment, it is often a precision-intensity trade-off one has to face. If possible nearly all flow investigations nowadays use spherical particles as flow tracers. A mathematical description of the motion of a sphere in a flow can be done with an equation published by Basset [8]. When considering small particles this equation can be simplified assuming Stokes' law of resistance, since particle Reynolds number and relative velocity becomes small. This can usually be applied for PIV and PTV measurements in liquid with tracer particles smaller than 50 µm. The differential equation of a particle can thus be reduced to

$$\frac{\mathrm{d}u_\mathrm{p}}{\mathrm{d}t} = \frac{18\mu_\mathrm{f}}{\rho_\mathrm{p}{d_\mathrm{p}}^2}(u_\mathrm{p} - u_\mathrm{f}). \tag{2.14}$$

The subscript characters represent the designation to *fluid* and *particle*, respectively. u is the absolute velocity, μ the dynamic viscosity, ρ the density and d the diameter. To quantify the particle behavior to follow the flow the so-called Stokes number can be introduced [97], which is the ratio of the response time of a particle τ_p and the time scale of the flow τ_f, and can be quantified as

$$\mathrm{Stk} = \frac{\tau_\mathrm{p}}{\tau_\mathrm{f}} = \frac{\frac{{d_\mathrm{p}}^2\rho_\mathrm{p}}{18\mu_\mathrm{f}}}{\frac{l_\mathrm{c}}{u_\mathrm{c}}} \tag{2.15}$$

with l_c standing for a characteristic length scale and u_c for a characteristic velocity of the flow. Note that these quantities must be chosen for every experiment individually and depend on the scientific question imposed to the flow.

Particle image density

For standard PIV measurements an important quality measure while conduct and post-processing is the number of particles imaged on the sensor N_p, which is refereed to as particle image density. Classic PIV literature describe this as *source density* [1]. One possible way of normalization to describe this value, which gained popularity over the last years is the number of particles per pixel N_ppp. However, for Defocusing Particle Tracking, this factor looses some relevance, since the diameter range is not reflected in the value. To compensate this Kaehler *et al.* [52] proposed a better suiting value, which considers the ratio between the sum of the particle image areas and the full image. This value is given as (following the formulation of [6])

$$N_\mathrm{S} = \frac{1}{A_\mathrm{I}} \sum_i {A_\mathrm{p}}^{(i)} \approx N_\mathrm{p} \frac{\overline{A_\mathrm{p}}}{A_\mathrm{I}}. \tag{2.16}$$

Here, A_I is the full image area, A_p is the particle image area and $\overline{A_\mathrm{p}}$ is the mean particle image area.

Circular Hough transform

To extract the particle locations and diameters out of a raw data image, a detection algorithm must identify the particle position and the defocused ring size. Different detection algorithms were used for this task such as edge detection [26] or cross correlation [6]. The present work introduces a new detection approach, which is based on the circular appearance of the defocused particle images and is called *Circular Hough transform.* The basic principles of this detection method are briefly outlined in the following.

Originally introduced in 1959 by Paul Hough [40] the Hough transform can be applied nowadays to arbitrary geometric forms and can be described as a feature extraction algorithm in general [20]. The circular Hough transform is able to detect circular shapes in a digital image. In order

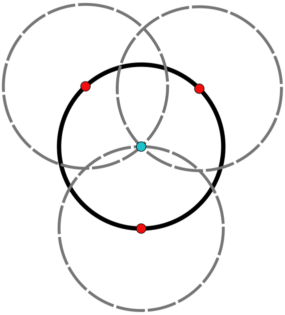

Figure 2.9: Explanation of the voting algorithm for a circular Hough transform. Each edge point (●) of the circular object to detect (—) vote with a presumed radius. All voting circles (– –) being part of the actual circular object accumulates in the center (●). Only three edge points and one radius are shown for clarity. Figure based on [4].

to realize this, the edges of an object are found by means of an gradient filter or an intensity threshold. The use of a gradient filter enables the opportunity to reduce further computational effort, since the direction of the object center can be determined. Each found edge point is now the center of a circle with the presumed radius and is voting for all pixels that lie on the radius of this circle. This is done for all detected edge points and all presumed radii, which results in the highest voting of the circular object center and given radius of the actual digital image as shown in Figure 2.9 for one radius, one particle and three exemplary edge points.

3 Analytical consideration and dimensionless description

This chapter is based on the journal publications *Non-dimensional characteristics of open wet clutches for advanced drag torque and aeration predictions* [LNG$^+$20] and *Analytical modeling and dimensionless characteristics of open wet clutches in consideration of gravity* [LNK$^+$21]. Where findings were already published in one of the named publications, this is clearly marked and indicated as related quotations. Changes within these quotations are only made for a consistent nomenclature.

3.1 Analytical derivation of velocities

The fluid mechanic insights of an open wet clutch can be described - to a certain extend - with analytical means. The present chapter summarizes the simplification of the Navier–Stokes equations and the formation of dimensionless quantities for the flow in an open wet clutch.

3.1.1 Simplifications of the Navier–Stokes equations

"In cylindrical coordinates the Navier–Stokes equations or momentum conservation for a steady flow of a Newtonian fluid in radial, circumferential and axial direction (r, φ and z component) can be seen in Equation (3.1-3.3). Note that the orientation of gravity is shown in Figure 2.1a. The

Table 3.1: Characteristic velocities and length scales for the order-of-magnitude analysis conducted in Equation (3.1-3.3).

parameter	symbol	characteristic quantity
radial flow rate	u_r	$u_r = \dfrac{q}{R}$
circumferential velocity	u_φ	ΩR
axial velocity	u_z	$u_z = u_r \dfrac{h}{R} = \dfrac{qh}{R^2}$
radial direction	R	$R = \dfrac{R_1 + R_2}{2}$
axial direction	h	h

order of magnitudes are indicated above each term. The characteristic velocities and length scales are summarized in Table 3.1. The local disk velocity ΩR is chosen as characteristic velocity along the circumferential direction, while the imposed volume flow rate per unit depth, referred to as q, is the radial velocity scale. The characteristic axial velocity follows from dimensional analysis of the continuity equation under the assumption that the gravitational force does not cause significant loss of axial symmetry in azimuthal velocity, i.e. that the term $\frac{1}{R}\frac{\partial u_\varphi}{\partial \varphi}$ can be neglected.

$$
\begin{aligned}
\textcircled{r}: \quad & \overbrace{u_r\frac{\partial u_r}{\partial r}}^{\mathcal{O}\left(\frac{q^2}{R^3}\right)} + \overbrace{\frac{u_\varphi}{r}\frac{\partial u_r}{\partial \varphi}}^{\mathcal{O}\left(\frac{\Omega q}{R}\right)} - \overbrace{\frac{u_\varphi^2}{r}}^{\mathcal{O}\left(\Omega^2 R\right)} + \overbrace{u_z\frac{\partial u_r}{\partial z}}^{\mathcal{O}\left(\frac{q^2}{R^3}\right)} \\
&= -\frac{1}{\rho}\frac{\partial p}{\partial r} + \overbrace{\nu\frac{\partial}{\partial r}\left[\frac{1}{r}\frac{\partial}{\partial r}(r u_r)\right]}^{\mathcal{O}\left(\frac{\nu q}{R^3}\right)} + \overbrace{\frac{\nu}{r^2}\frac{\partial^2 u_r}{\partial \varphi^2}}^{\mathcal{O}\left(\frac{\nu q}{R^3}\right)} \\
&\quad - \overbrace{\frac{2\nu}{r^2}\frac{\partial u_\varphi}{\partial \varphi}}^{\mathcal{O}\left(\frac{\nu \Omega}{R}\right)} + \overbrace{\nu\frac{\partial^2 u_r}{\partial z^2}}^{\mathcal{O}\left(\frac{\nu q}{R h^2}\right)} + g_r,
\end{aligned}
\tag{3.1}
$$

$$
\begin{aligned}
\textcircled{φ}: \quad & \overbrace{u_r\frac{\partial u_\varphi}{\partial r}}^{\mathcal{O}\left(\frac{q\Omega}{R}\right)} + \overbrace{\frac{u_\varphi}{r}\frac{\partial u_\varphi}{\partial \varphi}}^{\mathcal{O}\left(\Omega^2 R\right)} + \overbrace{\frac{u_r u_\varphi}{r}}^{\mathcal{O}\left(\frac{q\Omega}{R}\right)} + \overbrace{u_z\frac{\partial u_\varphi}{\partial z}}^{\mathcal{O}\left(\frac{q\Omega}{R}\right)} \\
&= -\frac{1}{\rho r}\frac{\partial p}{\partial \varphi} + \overbrace{\nu\frac{\partial}{\partial r}\left[\frac{1}{r}\frac{\partial}{\partial r}(r u_\varphi)\right]}^{\mathcal{O}\left(\frac{\nu \Omega}{R}\right)} + \overbrace{\frac{\nu}{r^2}\frac{\partial^2 u_\varphi}{\partial \varphi^2}}^{\mathcal{O}\left(\frac{\nu \Omega}{R}\right)} \\
&\quad + \overbrace{\frac{2\nu}{r^2}\frac{\partial u_r}{\partial \varphi}}^{\mathcal{O}\left(\frac{\nu q}{R^3}\right)} + \overbrace{\nu\frac{\partial^2 u_\varphi}{\partial z^2}}^{\mathcal{O}\left(\frac{\nu \Omega R}{h^2}\right)} + g_\varphi,
\end{aligned}
\tag{3.2}
$$

$$\textcircled{z}: \quad \overbrace{u_r \frac{\partial u_z}{\partial r}}^{\mathcal{O}\left(\frac{q^2 h}{R^4}\right)} + \overbrace{\frac{u_\varphi}{r} \frac{\partial u_z}{\partial \varphi}}^{\mathcal{O}\left(\frac{\Omega q h}{R^2}\right)} + \overbrace{u_z \frac{\partial u_z}{\partial z}}^{\mathcal{O}\left(\frac{q^2 h}{R^4}\right)} = -\frac{1}{\rho}\frac{\partial p}{\partial z}$$

$$+ \overbrace{\nu \left[\frac{1}{r}\frac{\partial}{\partial r}\left(r \frac{\partial u_z}{\partial r}\right)\right]}^{\mathcal{O}\left(\frac{\nu q h}{R^4}\right)} + \overbrace{\frac{\nu}{r^2}\frac{\partial^2 u_z}{\partial \varphi^2}}^{\mathcal{O}\left(\frac{\nu q h}{R^4}\right)} , + \overbrace{\nu \frac{\partial^2 u_z}{\partial z^2}}^{\mathcal{O}\left(\frac{\nu q}{R^2 h}\right)} , \qquad (3.3)$$

In order to obtain the relevant dimensionless numbers, the order of magnitudes of Equation (3.1) and (3.2) are normalized by the order of magnitude of their fifth term of the right hand side of the respective equation and Equation (3.3) is divided by the order of magnitude of the fourth term of the equation. The resulting dimensionless numbers are given as order-of-magnitude factors in Equation (3.4-3.6). Here, $\alpha = \frac{q}{\Omega R^2}$, $Re_\mathrm{g} = \frac{h^2 \Omega}{\nu}$ and $Fr = \frac{\Omega^2 R}{g}$ were introduced for further simplification. α is the ratio of the characteristic radial and circumferential velocity, while Re_g and Fr

are the gap Reynolds number and the Froude number based on the radius as characteristic length, respectively.

$$
\begin{aligned}
\textcircled{r}: \quad & \overbrace{u_r \frac{\partial u_r}{\partial r}}^{\mathcal{O}(\alpha Re_\mathrm{g})} + \overbrace{\frac{u_\varphi}{r}\frac{\partial u_r}{\partial \varphi}}^{\mathcal{O}(Re_\mathrm{g})} - \overbrace{\frac{u_\varphi^2}{r}}^{\mathcal{O}\left(\frac{Re_\mathrm{g}}{\alpha}\right)} + \overbrace{u_z \frac{\partial u_r}{\partial z}}^{\mathcal{O}(\alpha Re_\mathrm{g})} \\
& = -\frac{1}{\rho}\frac{\partial p}{\partial r} + \overbrace{\nu \frac{\partial}{\partial r}\left[\frac{1}{r}\frac{\partial}{\partial r}(r u_r)\right]}^{\mathcal{O}\left(\frac{h^2}{R^2}\right)} + \overbrace{\frac{\nu}{r^2}\frac{\partial^2 u_r}{\partial \varphi^2}}^{\mathcal{O}\left(\frac{h^2}{R^2}\right)} \\
& \quad - \overbrace{\frac{2\nu}{r^2}\frac{\partial u_\varphi}{\partial \varphi}}^{\mathcal{O}\left(\frac{h^2}{\alpha R^2}\right)} + \overbrace{\nu \frac{\partial^2 u_r}{\partial z^2}}^{\mathcal{O}(1)} + \overbrace{g_r}^{\mathcal{O}\left(\frac{Re_\mathrm{g}}{Fr\,\alpha}\right)} \quad ,
\end{aligned}
\tag{3.4}
$$

$$
\begin{aligned}
\textcircled{\varphi}: \quad & \overbrace{u_r \frac{\partial u_\varphi}{\partial r}}^{\mathcal{O}(\alpha Re_\mathrm{g})} + \overbrace{\frac{u_\varphi}{r}\frac{\partial u_\varphi}{\partial \varphi}}^{\mathcal{O}(Re_\mathrm{g})} + \overbrace{\frac{u_r u_\varphi}{r}}^{\mathcal{O}(\alpha Re_\mathrm{g})} + \overbrace{u_z \frac{\partial u_\varphi}{\partial z}}^{\mathcal{O}(\alpha Re_\mathrm{g})} \\
& = -\frac{1}{\rho r}\frac{\partial p}{\partial \varphi} + \overbrace{\nu \frac{\partial}{\partial r}\left[\frac{1}{r}\frac{\partial}{\partial r}(r u_\varphi)\right]}^{\mathcal{O}\left(\frac{h^2}{R^2}\right)} + \overbrace{\frac{\nu}{r^2}\frac{\partial^2 u_\varphi}{\partial \varphi^2}}^{\mathcal{O}\left(\frac{h^2}{R^2}\right)} \\
& \quad + \overbrace{\frac{2\nu}{r^2}\frac{\partial u_r}{\partial \varphi}}^{\mathcal{O}\left(\frac{\alpha h^2}{R^2}\right)} + \overbrace{\nu \frac{\partial^2 u_\varphi}{\partial z^2}}^{\mathcal{O}(1)} + \overbrace{g_\varphi}^{\mathcal{O}\left(\frac{Re_\mathrm{g}}{Fr}\right)} \quad ,
\end{aligned}
\tag{3.5}
$$

$$\begin{aligned}
\textcircled{z}:\quad & \overbrace{u_r \frac{\partial u_z}{\partial r}}^{\mathcal{O}(\alpha Re_{\mathrm{g}})} + \overbrace{\frac{u_\varphi}{r}\frac{\partial u_z}{\partial \varphi}}^{\mathcal{O}(Re_{\mathrm{g}})} + \overbrace{u_z \frac{\partial u_z}{\partial z}}^{\mathcal{O}(\alpha Re_{\mathrm{g}})} = -\frac{1}{\rho}\frac{\partial p}{\partial z} \\
& + \nu \overbrace{\left[\frac{1}{r}\frac{\partial}{\partial r}\left(r \frac{\partial u_z}{\partial r}\right)\right]}^{\mathcal{O}\left(\frac{h^2}{R^2}\right)} + \overbrace{\frac{\nu}{r^2}\frac{\partial^2 u_z}{\partial \varphi^2}}^{\mathcal{O}\left(\frac{h^2}{R^2}\right)}, + \nu \overbrace{\frac{\partial^2 u_z}{\partial z^2}}^{\mathcal{O}(1)}, \qquad (3.6)
\end{aligned}$$

Based on the relevant dimensionless numbers in the governing equations, simplifications can now be performed. The following assumptions can be applied to this flow:

(i) $h/R \ll 1$,

(ii) $Re_{\mathrm{g}} \ll 1$,

(iii) $Re_{\mathrm{g}} \gg \alpha$,

The first assumption is valid for nearly all gap flow scenarios, especially when considering sub-millimeter gaps. The second assumption can also be considered to be of general validity for the application at hand, since the typical region for an angular velocity ranges at $0 < n < 3000$. The third assumption depends on the magnitude of Ω and can be considered to hold true in the present case since aeration typically occurs at high circumferential speed. The role of the Froude-number Fr deserves a separate consideration. With the three assumptions described above, the three partial differential equations Equation (3.4-3.6) reduce to

$$-\overbrace{\frac{{u_\varphi}^2}{r}}^{\mathcal{O}\left(\frac{Re_\mathrm{g}}{\alpha}\right)} = -\frac{1}{\rho}\frac{\partial p}{\partial r} + \nu \overbrace{\frac{\partial^2 u_r}{\partial z^2}}^{\mathcal{O}(1)} - \overbrace{g\cos\varphi}^{\mathcal{O}\left(\frac{Re_\mathrm{g}}{Fr\,\alpha}\right)} \tag{3.7}$$

$$0 = -\frac{1}{r\rho}\frac{\partial p}{\partial \varphi} + \nu \overbrace{\frac{\partial^2 u_\varphi}{\partial z^2}}^{\mathcal{O}(1)} + \overbrace{g\sin\varphi}^{\mathcal{O}\left(\frac{Re_\mathrm{g}}{Fr}\right)} \tag{3.8}$$

$$0 = -\frac{1}{\rho}\frac{\partial p}{\partial z} + \nu \overbrace{\frac{\partial^2 u_z}{\partial z^2}}^{\mathcal{O}(1)} . \tag{3.9}$$

In order to solve this system of partial differential equations with analytical methods, further assumptions need to be taken. All partial derivatives of the pressure could in theory depend on the other spatial coordinates, which renders an integration impossible. A common way to overcome this issue is the consideration of vorticity transport, which again includes three equations, one for each spatial direction. Considering the already introduced simplifications these equations in r and φ-direction can be written as:

$$0 = \overbrace{\frac{\nu}{r}\frac{\partial^3 u_z}{\partial z^2 \partial \varphi}}^{\mathcal{O}\left(\frac{\alpha\, h^2}{R^2}\right)} - \overbrace{\nu \frac{\partial^3 u_\varphi}{\partial z^3}}^{\mathcal{O}(1)}, \tag{3.10}$$

$$\overbrace{-\frac{1}{r}\frac{\partial {u_\varphi}^2}{\partial z}}^{\mathcal{O}\left(\frac{Re_\mathrm{g}}{\alpha}\right)} = \overbrace{\nu \frac{\partial^3 u_r}{\partial z^3}}^{\mathcal{O}(1)} + \overbrace{\nu \frac{\partial^2 u_z}{\partial z^2 \partial r}}^{\mathcal{O}\left(\frac{h^2}{R^2}\right)}. \tag{3.11}$$

An order-of-magnitude analysis with the above-listed assumptions (i-iii) and a partial integration along z of both equations yields an additional integration term, which is no function of z.

$$0 = -\nu \frac{\partial^2 u_\varphi}{\partial z^2} + f_r(r, \varphi) \tag{3.12}$$

$$\frac{{u_\varphi}^2}{r} = \nu \frac{\partial^2 u_r}{\partial z^2} + f_\varphi(r, \varphi) \tag{3.13}$$

A simple term-wise comparison with Equation (3.7 -3.8) yields the conclusion that the pressure gradient in r-direction is not a function of z. The same holds for the pressure gradient in φ-direction. So Equation (3.7) and (3.8) can be integrated over z assuming a constant pressure gradient along z.

Following the initial assumption that $\frac{1}{R}\frac{\partial u_\varphi}{\partial \varphi}$ in the continuity equation can be neglected, the pressure gradient in φ-direction exactly balances with the gravitational force in that direction. In other words, the first term and third term on the right hand side of Equation (3.8) are equal and thus cancel in the equation. Overall, the order-of-magnitude analysis along with the introduced assumptions results in a differential system, which can be written as:

$$-\frac{{u_\varphi}^2}{r} = -\frac{1}{\rho}\frac{\partial p}{\partial r} + \nu\frac{\partial^2 u_r}{\partial z^2} - g\cos\varphi \tag{3.14}$$

$$0 = \nu\frac{\partial^2 u_\varphi}{\partial z^2} \tag{3.15}$$

$$0 = -\frac{1}{\rho}\frac{\partial p}{\partial z} + \nu\frac{\partial^2 u_z}{\partial z^2}. \tag{3.16}$$

These equations are similar to the earlier findings [LNG⁺20], but the gravitational force in the r-component now appears as additional term." [LNK⁺21]

3.1.2 Circumferential and radial velocity results

Equations (3.14) – (3.16) present an analytically solvable equation system, since the pressure gradient $\frac{\partial p}{\partial r}$ is not a function of z. The results for the circumferential and radial velocity, which are needed for further considerations can be determined to

$$u_\varphi(r,z) = \Omega r\frac{z}{h} \tag{3.17}$$

$$u_r(r,\varphi,z) = \frac{\Omega^2 rh}{12\nu}\left(z - \frac{z^4}{h^3}\right) - \frac{h}{2\mu}\frac{\partial p}{\partial r}\left(z - \frac{z^2}{h}\right) - \frac{gh}{2\nu}\cos\varphi\left(z - \frac{z^2}{h}\right). \tag{3.18}$$

The pressure gradient in r-direction, which is unknown up-to now, can be determined due to the fact that the supplied volumetric flow rate Q is a known quantity. An integration of the radial velocity along the axial and circumferential component leads to

$$Q = \text{const.} = \int_0^{2\pi} \int_0^h u_r r \, \mathrm{d}z\mathrm{d}\varphi = -\frac{\pi h^3}{6\mu}\frac{\partial p}{\partial r} + \frac{\pi r^2 h^3 \Omega^2}{20\nu}. \tag{3.19}$$

The component of the pressure gradient can be written as

$$\Leftrightarrow \frac{\partial p}{\partial r} = -\frac{6\mu Q}{\pi h^3 r} + \frac{3\rho\Omega^2 r}{10}. \tag{3.20}$$

Figure 3.1 shows the extracted normalized velocities for the radial and circumferential direction for the physical values summarized in Table 3.2. Five different angular velocities are chosen, which lead to five lubrication Reynolds numbers $Re_\mathrm{l} = \frac{R_2 h \Omega}{\nu}$. The φ–direction features a linear Couette flow for all angular velocities with the corresponding boundary condition of ΩR_2 at $z/h = 1$. The radial velocity depicts a sole Poiseuille flow at $Re_\mathrm{l} = 0$, where only the second term and the gravitational term of Equation (3.18) takes effect. With increasing lubrication Reynolds number the centrifugal forces acting - due to the upper plate rotating - increase as well. At $Re_\mathrm{l} = 121$ the pressure gradient changes its sign and at $Re_\mathrm{l} = 182$ the partial derivative in z–direction changes sign at $z/h = 0$, which leads to a flow in negative r–direction. These two conditions are important criteria for the ongoing aeration process. Their relevance and physical meaning will be analyzed in the following section.

These analytical solutions as stated in the Equations (3.17–3.18) and depicted in Figure 3.1 form the baseline for all prospective in-depth investigations and serve as benchmark for numerical and experimental efforts. In the following the results will be brought to a dimensionless frame of reference and the different aeration conditions are analyzed on the basis of their physical plausibility.

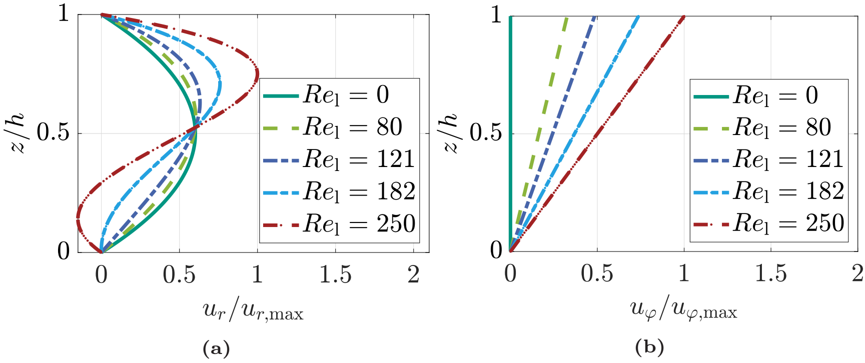

Figure 3.1: Velocity components at $r = R_2$ for the parameters shown in Table 3.2 (a) normalized radial velocity, (b) normalized circumferential velocity. (Figure adapted from [LNG+20].)

Table 3.2: Quantities of corresponding physical values for all relevant open clutch parameters. (Table adopted from [LNK+21].)

parameter	symbol	physical value	dimension
inner radius	R_1	$8.25 \cdot 10^{-2}$	[m]
outer radius	R_2	$9.375 \cdot 10^{-2}$	[m]
volume flow rate	Q	$1.667 \cdot 10^{-5}$	[m^3/s]
density	ρ	850	[kg/m^3]
dyn. viscosity	μ	0.0136	[Pa s]
kin. viscosity	ν	$16 \cdot 10^{-6}$	[m^2/s]
gap height	h	$450 \cdot 10^{-6}$	[m]
angular velocity	Ω	$0 < \Omega < 314$	[1/s]
grav. acceleration	g	9.81	[m/s^2]

3.2 Formulation of dimensionless quantities

"As shown in Figure 2.1a eight parameters influence the flow in an open wet clutch. A dimensional analysis (further explanation e.g. [102]) reduces these interdependencies to six dimensionless quantities, which are namely given as:

$$G = \frac{h}{R_2} \qquad \text{gap ratio,} \tag{3.21a}$$

$$\beta = \frac{R_1}{R_2} \qquad \text{radii ratio,} \tag{3.21b}$$

$$Re_\mathrm{l} = \frac{R_2 h \Omega}{\nu} \qquad \text{lubrication Reynolds number,} \tag{3.21c}$$

$$Q^* = \frac{Q\nu}{\Omega^2 {R_2}^2 h^3} \qquad \text{dimensionless flow rate,} \tag{3.21d}$$

$$\zeta_\mathrm{m} = \frac{T_\mathrm{s}}{\frac{\rho}{2} {R_2}^5 \Omega^2 \left(1 - \beta^4\right)} \qquad \text{moment coefficient,} \tag{3.21e}$$

$$Fr = \frac{\Omega^2 R_2}{g} \qquad \text{Froude number.} \tag{3.21f}$$

Small values of G identify flows in the gap flow category. For an open wet clutch, this value is typically in the order of $10^{-3} - 10^{-2}$. The radii ratio β serves as auxiliary parameter for the drag torque calculation, since the most significant amount of torque is generated between these two radii. The lubrication Reynolds number Re_l is ideally suited to describe the dimensionless torque as discussed in section 3.2.1. The dimensionless flow rate Q^* will serve as key parameter for the aeration condition in section 3.2.2. Finally, the moment coefficient ζ_m characterizes the drag torque as a function of Ω, or Re_l in a dimensionless consideration. Here the geometrical parameter β is already added, which reduces the calculation effort later on. With the help of these dimensionless numbers the formulation of the drag torque and aeration condition can be rewritten in a form which does not depend on the physical size and speed of a particular test rig.

3.2.1 Drag torque

The drag torque T_s as key factor for open clutch flow discussion is calculated by

$$\begin{aligned} T_\mathrm{s} &= \iint\limits_A \mu \frac{\partial u_\varphi}{\partial z} r \,\mathrm{d}A = 2\pi\mu \int\limits_{R_1}^{R_2} \left(\frac{\Omega r}{h}\right) r^2 \,\mathrm{d}r \\ &= \frac{\pi\mu\Omega}{2\,h}\left({R_2}^4 - {R_1}^4\right) \end{aligned} \tag{3.22}$$

With the use of this equation the moment coefficient Equation (3.21e) can be rewritten to

$$\zeta_\mathrm{m} = \frac{\pi}{Re_\mathrm{l}}. \tag{3.23}$$

Thus, the dimensionless reformulation provides a simple formulation to directly estimate the drag torque. This formulation is particularly valuable for the comparison of set-ups with different geometrical dimensions. Instead of using a $T_\mathrm{s} - \Omega$ diagram, which is normally done, a dimensionless $\zeta_\mathrm{m} - Re_\mathrm{l}$ diagram allows a direct comparison of data gained with different geometrical or fluid parameters.

3.2.2 Aeration condition

An aeration condition that is frequently used to mathematically describe the start of aeration is the sign change of the pressure gradient (e.g.[41, 44]). This state occurs normally at the outer radius first, since the pressure is lower at this point. This condition results in a formulation of the critical angular velocity $\Omega_{\mathrm{c,I}}$ for the aeration start.

$$\frac{\partial p}{\partial r}\left(r = R_2,\ \Omega = \Omega_{\mathrm{c,I}}\right) \overset{!}{=} 0 = -\frac{6\mu Q}{\pi h^3 r} + \frac{3\rho {\Omega_{\mathrm{c,I}}}^2 r}{10} \tag{3.24}$$

This expression, in which dimensional geometrical and flow parameters appear explicitly, can be further shortened and simplified to one simple equation through the introduction of dimensionless numbers.

The dimensionless formulation is given by

$$Q^* = \frac{Q\nu}{{\Omega_{\mathrm{c,I}}}^2 {R_2}^2 h^3} = \frac{\pi}{20}. \tag{3.25}$$

Since now the gravitational force is part of the calculations an additional downside of this aeration condition takes effect. This model can't resolve the role of gravity to a different start of aeration, since the pressure gradient in r-direction is axis symmetric in φ-direction.

An aeration formulation that is more likely from a fluid mechanics perspective is the occurrence of back flow of the radial velocity, which is in a normal pipe flow equal to the sign change of the pressure gradient, but due to additional force components not in this flow case. This condition will be introduced as second aeration model. Given the applied boundary conditions the reverse flow will occur at $z = 0$. The mathematical formulation yields

$$\begin{aligned}\frac{\partial u_r}{\partial z}\left(z = 0,\ r = R_2,\ \Omega = \Omega_{\mathrm{c,II}}\right) &\overset{!}{=} 0 \\ &= \frac{{\Omega_{\mathrm{c,II}}}^2 R_2 h}{12\nu} - \frac{h}{2\mu}\frac{\partial p}{\partial r} - \frac{gh}{2\nu}\cos\varphi \end{aligned} \tag{3.26}$$

with the formulation of the pressure gradient (Equation 3.20) and the reformulation with the help of the dimensionless flow rate Q^* and the Froude number Fr this equals

$$\begin{aligned} 0 &= \frac{{\Omega_{\mathrm{c,II}}}^2 R_2 h}{12\nu} - \frac{3Q}{\pi h^2 R_2} - \frac{3\rho {\Omega_{\mathrm{c,II}}}^2 R_2 h}{20\mu} - \frac{gh}{2\nu}\cos\varphi \\ \Leftrightarrow \frac{1}{45} &= \frac{Q\nu}{h^3 {R_2}^2 {\Omega_{\mathrm{c,II}}}^2 \pi} - \frac{g\cos\varphi}{6{\Omega_{\mathrm{c,II}}}^2 R_2} \\ \Leftrightarrow \frac{\pi}{45} &= Q^* - \frac{\pi}{6}\cos\varphi\frac{1}{\mathrm{Fr}}. \end{aligned} \tag{3.27}$$

This aeration model in fact supports gravitational effects as well as a localization of the aeration start. If a test rig is placed as indicated in Figure 2.1a the aeration starts at the highest point of the disk. This might be beneficial information for experimental investigation, since a detailed localization can be investigated easier in terms of optical access and image resolution.” [LNK$^+$21]

3.2.3 Benefits of dimensionless approach – the way to a direct comparison

“A simple example is chosen to demonstrate the benefit of the dimensionless approach in the following. Figure 3.2 depicts the drag torque for three geometric parameter combinations in terms of gap height h, volumetric flow rate Q and outer radius R_2. For all three parameter combinations it is possible to calculate the corresponding slope of the drag torque and the point, where aeration occurs, according to Equation (3.22) and Equation (3.25), respectively. Consequently, this leads to three different slopes and three different aeration points. Converted to the above-derived dimensionless quantities the three different parameter combinations collapse onto a single curve in a $\zeta_{\mathrm{m}} - Re_{\mathrm{l}}$ diagram according to Equation (3.23); see Figure 3.3a.

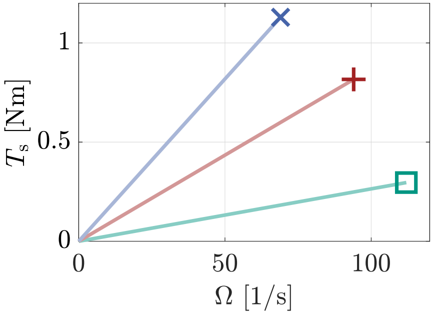

Figure 3.2: Drag torque T_s as a function of angular velocity Ω for three different, arbitrary chosen parameter combinations: (Figure adapted from [LNG+20].)
🟦 : $h = 250\ \mu\text{m}, Q = 1$ l/min, $R_2 = 0.09375$ m;
🟥 : $h = 350\ \mu\text{m}, Q = 3$ l/min, $R_2 = 0.1172$ m;
🟩 : $h = 450\ \mu\text{m}, Q = 5$ l/min, $R_2 = 0.1406$ m.

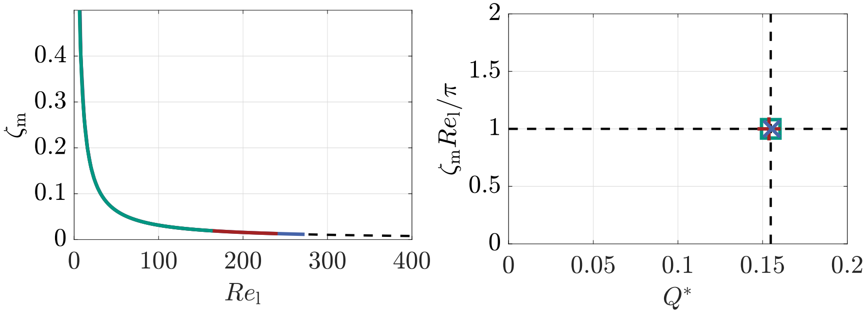

(a)

(b)

Figure 3.3: (a) dimensionless quantities moment coefficient ζ_m over Reynolds number Re_l (b) Product $\zeta_m Re_l/\pi$ over Q^* of the parameter combination used in Figure 3.2. (Figure adapted from [LNG+20].)

The markers in Figure 3.2 represent the points at which aeration occurs according to Equation (3.25). For the chosen different parameter combinations this happens at three different values of Ω. Similarly normalized, all points collapse for a non-dimensional critical flow rate $Q^*_{\text{crit}} = \frac{\pi}{20} \approx 0.157$, as shown in Figure 3.3b. On the ordinate of this diagram the combined quantity $\zeta_m Re_l/\pi$ is plotted. Since the analytical relations in Figure 3.3

are valid for the idealized flow situation where all applied simplifications are fully justified, it is expected that experimental or numerical results might show some deviations. Note, however, that the order of magnitude for maximum drag torque before aeration onset can likewise be captured with any existing model [16, 41, 43, 70, 78]. So the dimensionless approach isn't limited to a specific model." [LNG+20]

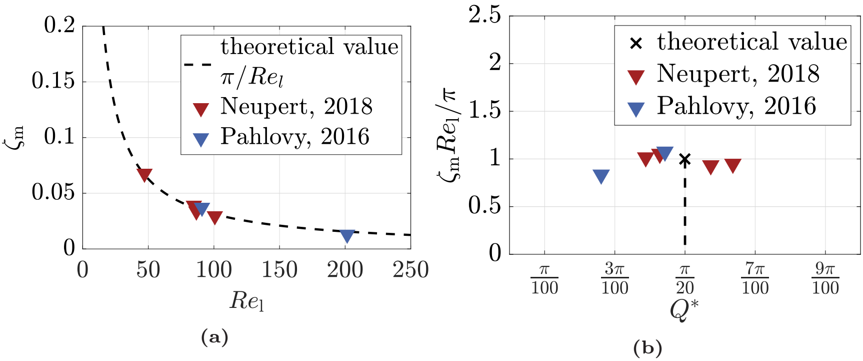

Figure 3.4: (a) Dimensionless formulation of the point of aeration (maximum of corresponding drag torque curve) in a dimensionless representation for experimental data acquired by [62, 71]. All experimental data lie in the vicinity of the analytically derived theoretical value π/Re_l. (b) Experimental data of the aeration start in comparison to the theoretical value of Q^*_crit. Here the data deviates significantly. (Figure adapted from [LNG+20].)

"Another benefit is the possibility to compare different experimental drag torque measurements obtained on test rigs with different geometric dimensions. The markers in Figure 3.4 indicate the point of aeration from different publications. All considered experimental data [62, 71] match the theoretical prediction according to Equation (3.23) in the $\zeta_\mathrm{m} - Re_\mathrm{l}$ diagram (Figure 3.4a), which retroactively also verifies Equation (3.22) as to be an appropriate drag-torque prediction. Figure 3.4b shows the product of $\zeta_\mathrm{m} Re_\mathrm{l}/\pi$ over the normalized flow rate Q^*. The theoretical value for aeration is placed at $\pi/20$, if the above-outlined assumption of a sign change of the pressure gradient as to coincide with the aeration onset is considered. The values are in the same order-of-magnitude, but deviate considerably from the theoretical value.” [LNG$^+$20]

An additional benefit of the dimensionless description is the possibility of a fast and easy error calculation. In all former analytical drag torque models the influence of gravity is neglected with no proper, quantitative explanation (e.g. [16, 71]). Considering Equation (3.27) the influence of gravity can be quantified and a possible error regarding the expected deviation of the dimensional value Ω can be calculated. For a possible error evaluation a new quantity can be introduced, which acts as quantified criterion. This quantity is called Γ, represents the ratio between the second and the first term of equation (3.27), and can be expressed as

$$\Gamma = \frac{\frac{\pi}{6\,\mathrm{Fr}}\cos\varphi}{Q^*} = \frac{R_2 h^3 \pi g \cos\varphi}{6Q\nu}. \tag{3.28}$$

It has to be emphasized, that the angular velocity Ω is no longer an influential factor, so the influence of gravitation is no function of a slow or fast rotating clutch. A small value of Γ results in a dominant term of Q^*, which means the gravitational influence can be neglected. This value is beneficial for an a priori check-up, whether the accepted error is e.g. 1% or 0.1% in further calculations.

The second possibility to quantify the role of gravity with the help of Equation (3.27) is a calculation of the aeration start with and without gravitational term. This leads to two slightly different $\Omega_{\mathrm{c,II}}$. A direct comparison might be desired information for clutch manufacturers, since it transforms the results back to the physical space. When using the values of Table 3.2 this difference would result in a value of $\Delta\Omega_{\mathrm{c,II}} = 5.9$.

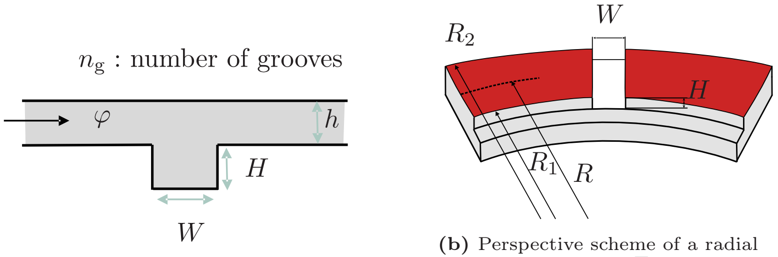

(a) Groove segment of a radial groove: ▨ area A; – wetted perimeter P

(b) Perspective scheme of a radial groove segment; ☐ grooved area A_groove, 🟥 ungrooved area A_disk.

Figure 3.5: Geometric dimensions and designation of the disk and groove. (Figure adopted from [LNG+20].)

3.3 Effect of grooves on aeration onset

“The fact that grooves can yield an aeration onset at lower circumferential speed as compared to a flat disk, has been discussed by various authors as has been recently summarized by Neupert *et al.* [61, 62], for instance.

Figure 3.5 shows a radially grooved disk, which comprises the relevant geometrical parameters. Pahlovy *et al.* [70] introduce the equivalent gap height value for a grooved disk as

$$h_\mathrm{eq,pah} = h + H\, a_\mathrm{g} = h + H \frac{A_\mathrm{groove}}{A_\mathrm{disk}}. \tag{3.29}$$

Here, a_g is the ratio of the grooved and ungrooved surface area and H is the height of the groove. The equivalent gap height $h_\mathrm{eq,pah}$ is thus a weighted mean of the grooved and ungrooved areas. This leads consequently to an earlier aeration onset. Even tough the modeling approach shows promising results in comparison with experiments for a specific groove geometry, it is not capable to capture the complex non-linear behavior of different types of grooves as examined by Neupert *et al.* [62]. Especially the expected effect of the change of groove ratio H/W (where W is the groove width) cannot be considered properly with this approach as shown later.

Inspired by these earlier efforts, an alternative formulation of the equivalent gap height is introduced in the following, which builds upon the hydraulic-diameter concept.

The forces that act on an infinite fluid volume moving from the inner to the outer radius of an open clutch can be divided into separate constitutive components. For a smooth disk this summation of forces can be modelled based on the simplified Navier–Stokes equations discussed earlier. The point of aeration is mainly a balance between inertia, centrifugal and frictional forces. The introduction of grooves moves this balance to another equilibrium state. Increasing the cross-sectional through-flow area at the same pressure gradient reduces the frictional forces on one hand. Frictional forces are, on the other hand, increased with a greater wetted perimeter.

The analytical solution based on the assumptions for smooth disks are not suitable for grooved surfaces, since they cannot consider the complex flow phenomena in the grooves, such as e.g. helical and/or vortical structures inside the grooves [LK19]. A profound analysis of the underlying fluid flow must be done by experiments or numerical simulations. Nevertheless, for a first and fast approximation an adapted version of the model for smooth walls might be able to deliver acceptable results. An easy way to capture a complex geometry in fluid mechanics is the concept of hydraulic diameter, originally introduced for turbulent flow in ducts with a non-circular cross-section (see e.g. [87]). The hydraulic diameter for the present flow can be calculated with the cross sectional area A at the mean radius R and the wetted perimeter of the cross-section P

$$D_{\mathrm{hy}} = \frac{4A}{P}, \tag{3.30}$$

where

$$A = 2\pi R h \;\text{ and }\; P = 4\pi R; \qquad R = \frac{R_1 + R_2}{2}.$$

For an ungrooved disk this value gives $D_{\mathrm{hy}} = 2\,h$. For a radially grooved disk A and P both change such that the equivalent gap height can be defined as

$$h_{\mathrm{eq}} = \frac{D_{\mathrm{hy}}}{2} = \frac{2A}{P} = \frac{h\pi\left(R_1 + R_2\right) + n_{\mathrm{g}}HW}{\pi\left(R_1 + R_2\right) + n_{\mathrm{g}}H}. \tag{3.31}$$

Reorganisation of Equation (3.31) leads to

$$h_{\mathrm{eq}} = \frac{h + H\frac{A_{\mathrm{groove}}}{A_{\mathrm{disk}}}}{1 + \frac{H}{W}\frac{A_{\mathrm{groove}}}{A_{\mathrm{disk}}}}. \tag{3.32}$$

The direct comparison with Equation (3.29) as suggested by PAHLOVY *et al.* [70] indicates that the numerators of both approaches are identical. However, differences exist in the denominator, where the present model formulation introduces a non-linear influence of the groove height. Figure 3.6 shows the direct comparison of these two approaches, Equation (3.29) and Equation (3.32), to indicate the influence of the modified denominator i.e. the impact of the hydraulic diameter. Figure 3.6a and 3.6b depict h_{eq} as a function of groove height H for constant groove width W and vice versa, respectively. Figure 3.6c and 3.6d represent slightly more complex variation scenarios. The third diagram shows a variation of W and H, while the product of these two quantities is constant. For the fourth diagram the frictional area is set constant, so the number of grooves n decreases with increasing width W. The latter two cases are chosen, to provide comparability to the systematic experimental study of NEUPERT *et al.* [62].

The advantages of the hydraulic diameter approach becomes obvious from the latter two cases (Figs. 3.6c and 3.6d). For a constant product of groove height and width the model based on Equation (3.29) does not predict a change in drag torque, whereas the new approach, Equation (3.32), offers a systematic dependency, which is in agreement with the experimental findings. This different character also holds for a constant frictional area,

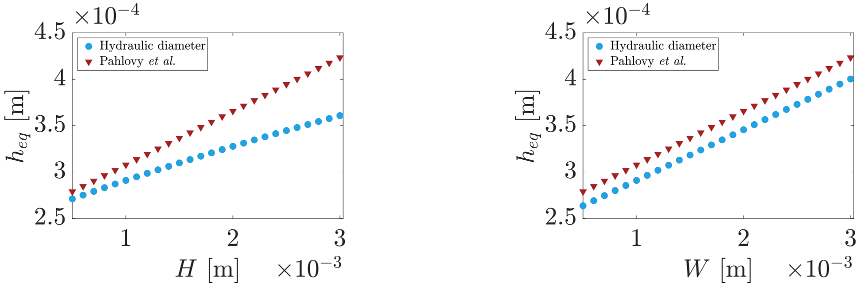

(a) $W = 1$ mm; $n_\mathrm{g} = 32$

(b) $H = 1$ mm; $n_\mathrm{g} = 32$

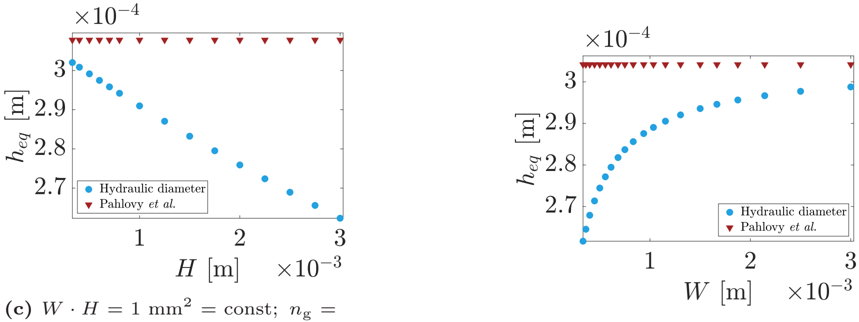

(c) $W \cdot H = 1\ \mathrm{mm}^2 = \mathrm{const}$; $n_\mathrm{g} = 32$

(d) $H = 1$ mm; $A_{disk} = \mathrm{const.}$

Figure 3.6: A systematic comparison of both evaluated models with different parameters. ● : present approach using hydraulic diameter concept; ▼ : approach of PAHLOVY *et al.* [70] (Figure adopted from [LNG+20].)

which is the fourth case.” [LNG+20]

These results give a precise insight of the open wet clutch flow with no grooves and a first, yet accurate, indication for aeration start with groove patterns. For further in-depth analyses and precise investigations pertaining to the fluid flow with complex groove pattern analytical-derived solutions have their clear limitations. At this point numerical or experimental methods must take over. However, the derived equations can indicate valuable directions, which lead to a more systematic choice of beneficial groove patterns. One of these insights is explained in the following and might be crucial knowledge, when first designing a groove geometry.

3.4 Effect of grooves on the flow field

“The shape of the grooves and their specific design did not reach a fundamental understanding from the fluid mechanics point of view and is currently often a choice of experience for a clutch manufacturer. In general, the addition of a groove pattern locally increases the cross section through which the fluid can pass on its way from the inner to the outer radius. The interplay of different force components, like inertia, centrifugal and frictional force is shifted to another equilibrium due to the presence of grooves.” [LNK+21]

“This holistic view on the groove geometry is discussed under certain aspects in the following, to achieve an insight that seems appropriate to the level of detail of analytical solutions. For the following analysis, it is assumed that the overall flow pattern can be described with the analytical solution derived for a smooth disk even when grooves are applied to the rotating disk. Figure 3.7 shows the radial and relative circumferential velocity, u_r and u_φ extracted from the analytical solution, where the gravitational term is neglected. Note that for the circumferential velocity a change of the reference frame to a disk-fixed coordinate system took place. Thus in the figure, the rotating disk features a relative velocity of 0.

Figure 3.8 shows the velocity at different heights in the vicinity of the moving disk ($\Omega = 10$), where a potential groove would be placed. For visual aspects a $x - y$ coordinate system is used and only a region of $\varphi \in [-10°; 10°]$ is plotted. Despite the fact that the velocities are localized at ● 0.7 z/h, ● 0.8 z/h and ● 0.9 z/h, all share a similar direction. Thus, when considering a fluid particle, which starts from the inner radius and moves to the outer radius, the actual height does not affect the shape of the streamlines/path lines significantly. This fact is supported by Figure 3.8d, where the streamlines of the above-stated heights are shown. The streamlines start at $r = R_1$ and the corresponding height. A given angular velocity consequently produces similar streamlines for the near-wall region.

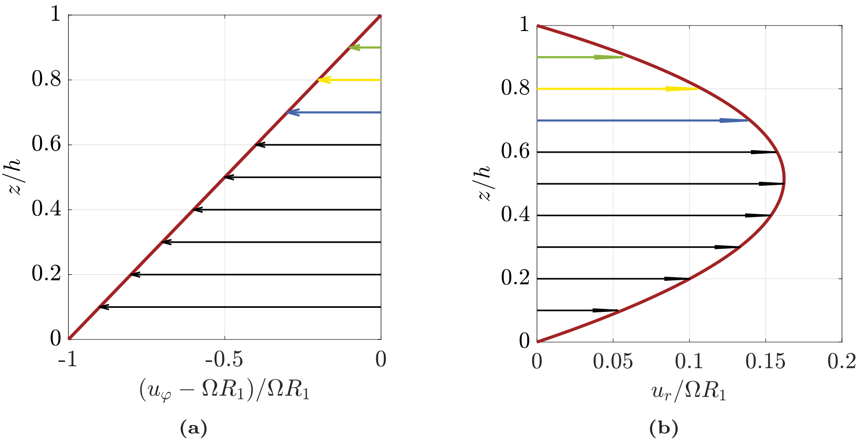

Figure 3.7: (a) normalized circumferential velocity in a disk-fixed frame of reference (b) normalized radial velocity; The velocity values at $0.7 - 0.9\ h$ are color coded to fit to Figure 3.8. (Figure adopted from [LNK$^+$21].)

Under the assumption that the flow with and without grooves are similar, a potential successful groove shape can be modeled to follow the shape of the streamlines in the disk-near region. An ideally minimum deviation from this path could be reached if the groove shape, that is also moving with the rotating disk, has the same shape than the streamlines/path lines. This shape has the benefit that the introduction of a groove does not disturb the streamlines, which leads to an outflow without losses and, thus, to an earlier aeration. However, the exact shape is only valid for the considered parameter combination and operating point ($\Omega = 10$). This in fact could be used as benefit, since an accurate fine-adjustment is possible for a desired operating point. For further investigations, into a detailed aeration prediction the analytical concept, with its strong simplifications is not the right concept. Here experimental or numerical tools must take over, especially when the groove height and width changes along the radius to reach a minimum deviation from the streamlines of a disk without grooves. For future groove design a check of the expected aeration point and the corresponding streamline curvatures might be of interest to reach a drag

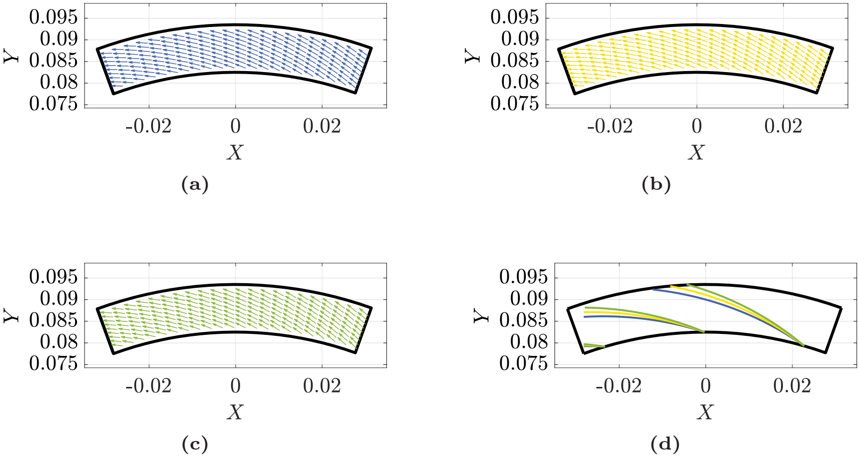

Figure 3.8: Normalized relative velocity $u_\varphi - \Omega r$ and u_r for different heights above the rotating disk. ((a) ● 0.7 z/h, (b) ● 0.8 z/h and (c) ● 0.9 z/h) The colors correspond to the z/h-levels in Figure 3.7. (d) streamlines originating at $r = R_1$ and the corresponding normalized height. (Figure adopted from [LNK+21].)

reduction at the desired operation condition, which is valuable knowledge in early-stage designing process for a clutch disk manufacturer. With this information also already existing groove designs, like waffle, sunburst or group-parallel, can be cross-checked of their suitability in each specific scenario of application with its individual needs. The general groove design of a backward curved groove, however, serves as starting point for a future in-depth analysis.” [LNK+21]

3.5 Concluding remarks (regarding the analytical and dimensionless consideration)

The dimensionless quantities give a strong building set to analyze and compare experimental, numerical and analytical efforts. The analytical approach produces some meaningful insights, into the cause-effects of the fluid flow of an open wet clutch with no grooves applied. These effects are the dominant velocity distribution, the following shear stress and drag torque calculations as well as the fluid mechanic-based aeration consideration, which follows from the radial velocity distribution. “The simplifications required to reach an analytically integrable partial differential system for open wet clutch flows in consideration of gravitational forces have been outlined in detail. Two dimensionless key factors are the gap Reynolds number Re_g and the ratio of radial flow compared to circumferential flow α. Both quantities need to be small in order to reach the concluded simplifications. The consideration of the gravitational force impacts only the radial velocity component. With this force component an aeration will occur earlier, based on the aeration condition of a reverse flow at the stationary disk. Six dimensionless numbers are identified, that enable a fast calculation of drag torque and aeration without solving complex equations. The dimensionless drag torque can be rewritten to $\zeta_\mathrm{m} = \frac{\pi}{Re_1}$, while the aeration onset based on a reversed flow at the stationary disk can be described via $Q^* - \frac{\pi}{6}\frac{\cos\varphi}{Fr}$. The aeration thus starts at $\varphi = 0$ when gravitation acts on a test rig in upright position. The consideration of grooves on the surface of the rotating disks is done via a holistic view by means of streamlines in the vicinity of $z/h = 1$. A backward curved along the radius r is suggested, since the groove shape follows the streamlines in this case. This information, despite the simplicity of the considered approach, provides a valuable guideline for clutch pattern design beyond existing engineering tools.” [LNK$^+$21]

The analytical approach together with the dimensionless description leads unequivocally to deeper insights and a better understanding of the fluid flow in an open wet clutch, such as the dominant flow velocity and a comparison tool, which is independent from the present geometry of a specific experiment. However, the treatment is limited to a consideration without grooves or a model assumption of grooves and, therefore, a simplification of the ongoing phenomena. For further insights into cause-effect relations, that are groove-pattern dominated numerical or experimental efforts need to take over. This is why, the following chapters present two experimental approaches, that shed light into the flow of an open wet clutch with grooves. The insights from the present chapter such as the formulation of a suitable Reynolds number, the analytically-derived velocity distribution and the backward curved streamline are going to help as classification and comparison tool.

4 Laser Doppler Velocimetry Profile Sensor - angular-resolved experimental approach

This chapter is based on the journal publication *On the Applicability of LDV Profile-Sensors for periodic Open Wet Clutch Flow Scenarios* [LPK22]. Where findings were already published, this is clearly marked and indicated as related quotations. Changes within these quotations are only made for a consistent nomenclature.

The current chapter tests the capabilities of a LDV profile sensor on an open wet clutch test rig with radial grooves. The fundamentals for the given approach have been already recapped in Chapter 2. The current chapter introduces the test-rig relevant details and set-up specific characteristics of this novel technique and focuses on the applicability specifics of the measurement principle. As far as possible only application-inherent fundamentals are recapitulated here.

4.1 Experimental procedure

First the measurement concept and set-up is explained, followed by an accuracy consideration and the fluid mechanic results, that could be extracted with this technique.

4.1.1 Measurement principle

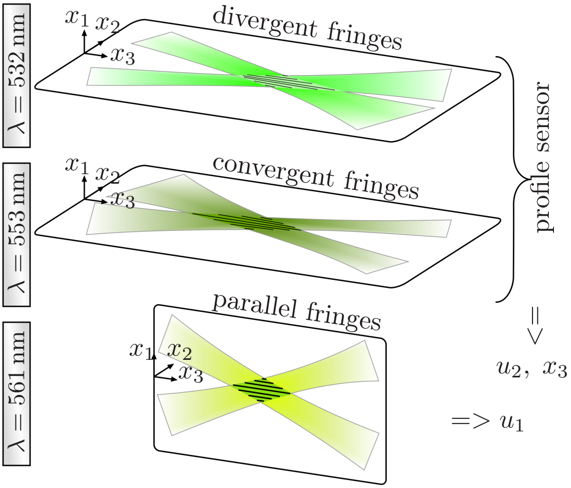

Figure 4.1: Equipment of the used LDV-PS. The first two components provide one velocity component and the spacial information, the third component with parallel fringes provides a second velocity component. (Figure adopted from [LPK22].)

“The main difference of a profile sensor compared to a conventional LDV set-up is the use of two overlapping fringe systems with different spatial gradients, wherewith one velocity component and the position of particles passing through the measurement volume can be detected. The beam waist positions of the two laser systems are, therefore, shifted longitudinally away from the intersection point in opposite directions. Thus, the fringes are diametrically opposed and the fringe spacings $d_{\mathrm{f},i}$ for $i = 1, 2$ are a function of the x_3-position as illustrated in Figure 4.1, where the complete used LDV-system is decomposed for the different laser beams. The x_3-position of the particles can be determined by the quotient q of the received Doppler frequencies f_i which is given by $q(x_3) = f_2/f_1 = d_{\mathrm{f},1}(x_3)/d_{\mathrm{f},2}(x_3)$, if the velocity u_1 is equal to u_2. x_3 can then be found by means of a calibration function. Once the x_3-position of a particle is found the local fringe spacings $d_{\mathrm{f},i}$ and the resulting velocity u can be calculated retroactively. Therefore, the calibration procedure is of major importance for the measurement process, which is normally done already by the manufacturer. According to [18] the uncertainty of the position can be stated as

$$x_3{}^{\sigma} = \sqrt{2}\frac{\partial x_3}{\partial q}\frac{f^{\sigma}}{f}. \tag{4.1}$$

A possible location error depends on the slope of the calibration function q and the ratio of frequency uncertainty f^{σ} and the frequency f. Possible measurement errors are a low Signal-to-Noise ratio (SNR), a undersampled burst signal or – in case of a industry-near application – vibrations of the test rig.

For the conducted experiments an *ILA R&D* 1D2C-LDV Profile Sensor with two Nd:YAG lasers ($\lambda = 532\,\mathrm{nm}$ and $\lambda = 553\,\mathrm{nm}$) and an additional laser in a general LDV set-up ($\lambda = 561\,\mathrm{nm}$) to determine a second velocity component are employed as shown in Figure 4.1. The two lasers featuring the profile sensor functionality detect the circumferential velocity and the general LDV set-up detects the radial and axial velocity. All components are Bragg-shifted with a frequency of 5 MHz (40 MHz native modulation with downsampling) and the focal length of the applied front lens of the sensor is 160 mm. Additional profile-sensor parameters are summarized in Table 4.1. The calibration quotient q together with the fringe distances for the used LDV sensor is depicted in Figure 4.2. For the velocity measurements the coincidence mode of the LDV-sensor was enabled, resulting in the measurement of only those particles, that were registered with all three laser components. Each channel's validation option must be met in order to lead to a valid coincidence signal. Moreover, the position limit of the profile sensor (600 µm) must be satisfied.

Table 4.1: Parameters of the LDV–PS used for this study.

	laser component 1	laser component 2
wavelength	532 nm	553 nm
power	150 mW	150 mW
$d_f(x_3 = 0)$	1.25 µm	1.90 µm
$\dfrac{\partial q}{\partial x_3}$	0.000083 1/µm	

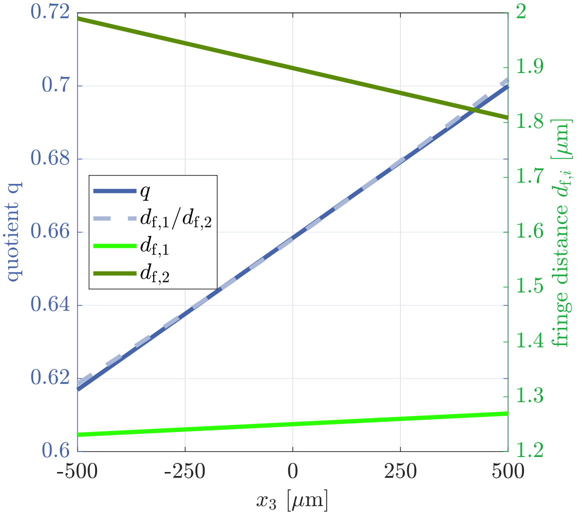

Figure 4.2: The linearized calibration curve q, used for this LDV profile sensor together with the associated fringe spacings $d_{f,i}$ over x_3 for both spanned fringe patterns. (Figure adopted from [LPK22].)

4.1.2 Experimental set-up and test rig variants

The set-up for all conducted experiments is an open wet clutch facility, which comprises a single-stage rotor-stator configuration as shown in Figure 4.3. The stator plate serves as optical access with anti-reflection coated float glass window to guarantee a low distortion of the inbound and scattered light. As rotating counterpart an interchangeable disk construction serves the purpose to operate different groove patterns or non-grooved clutch plates. For a repeatable and precise movement of the rotating disk unit a *nanotec ST11018L8004* stepping motor was used. Angular-resolved measurements are enabled due to a *WL100L-F2231* light barrier sensor.

For the uncertainty quantification of the LDV-PS system the test rig is equipped with *variant A*, according to Figure 4.3. A wire of diameter $d_\mathrm{w} = 10\,\mu\mathrm{m}$ is mounted on the rotating plate at different rotational velocities. The sensor is tilted to face the wire orthogonal and the stationary housing of the test-rig with the glass plate is removed. The set-up for these studies is shown in Figure 4.3a and aims to mimic a particle at exactly the same angular and lateral position, as well as a known and constant velocity. Similar test set-ups were conducted by [18] and are carried out during the calibration of the LDV-PS at the manufacturer. This set-up is referred to as *wire set-up* or *variant A* below.

The flow structure investigation, as actual test scenario, is progressed with a radially-grooved rotor disk and oil in between the gap of the rotor and stator, as sketched and referred to as variant B in Figure 4.3. The clutch is operated at an angular velocity of $\Omega = 12.6\,1/\mathrm{s}$, which equals a low-to-moderate circumferential disk velocity (according to [42], for instance) and corresponds to an expected disk velocity of $u_\varphi = 1.1\,\mathrm{m/s}$ at the mean radius $R_\mathrm{m} = (R_1 + R_2)/2$. The inner and outer radii of the disk are $R_1 = 82.5$ and $R_2 = 93.75\,\mathrm{mm}$. The disk features 32 evenly distributed radial grooves with a bottom groove width of $W = 1.35\,\mathrm{mm}$ and height of $H = 0.97\,\mathrm{mm}$. The gap between rotor and stator is adjusted to $h = 320\,\mu\mathrm{m}$. The measurement ellipsoid length is adjusted to 600 µm and traversed in

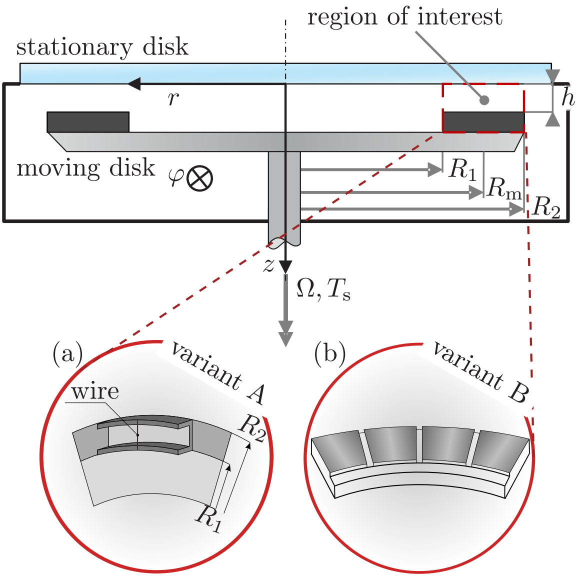

Figure 4.3: Scheme of an open clutch with all relevant parameters and the region of interest for the LDV investigation and both conducted experimental set-ups; (a) wire for uncertainty conducts, (b) radial groove for flow measurement. (Figure adopted from [LPK22].)

200 µm steps through the gap along the sensor axis. Despite full coverage of the entire gap with the ellipsiod, the traversing appears necessary, since the measuring region in z-direction spans a length of $h + H = 1.29\,\mathrm{mm}$ at the groove locations. The adjustments of the ellipsoid length resulted from the findings of the conducted wire experiment as will be elaborated further below. The radial position of the measurement ellipsoid for both inclination angles was located at the mean radius R_m and validated with the expected disk velocity.

The applied white mineral oil ($\rho_\mathrm{o} = 850\,\mathrm{kg/m^3}$, dynamic viscosity $\mu = 0.0136\,\mathrm{kg/ms}$, refractive index $n_\mathrm{r} = 1.4$) has been seeded with silver-coated hollow glass spheres ($d = 14\,\mu\mathrm{m}$; $\rho_\mathrm{p} = 1700\,\mathrm{kg/m^3}$), which corresponds to a characteristic time scale of $\tau_\mathrm{p} = 1.36 \times 10^{-6}\,\mathrm{s}$ and a Stokes number of

$S_k = 0.0047$, considering the gap height as characteristic length scale. The gap and the inner part of the clutch was filled with oil to ensure a single-phase flow through the gap, but no additional external volumetric flow rate was applied. The corresponding gap Reynolds number as already discussed by [19] results in $Re_\mathrm{g} = \Omega h^2/\nu = 0.08$. The corresponding lubrication Reynolds number is $Re_\mathrm{l} = \Omega R_\mathrm{m} h/\nu = 22.0$, which is considered for the present flow scenario (cp. also [LNG+20]).

4.1.3 Evaluation of the third velocity component

To extent the velocity-component measurement and also to avoid influential light reflections, the sensor is tilted forwards and backwards to an angle of $\alpha_1 = 30°$ compared to the z-axis. The x_3-axis as indicated in Figure 4.1 is rotated with $\pm 30°$ compared to the z-axis of the test rig as indicated in Figure 4.4. This way of measurement enables particle detection in proximity to the disk where normally the reflected light limits the detection of the particle's Mie scattering. Additionally, this enables the retroactive determination of the third flow component, which would otherwise be impossible to capture with an LDV sensor and this complex geometric set-up. The two considered sensor positions as used for the flow measurements are shown in Figure 4.4.

While the circumferential velocity component u_φ is measured with the profile sensor lasers and directly with either sensor positions I and II, both components u_r and u_z are combined in the second conventional recorded velocity component perpendicular to the sensor axis in the $r - z$-plane. According to the sensor orientations, this second component is referred to as $u_{2,\mathrm{p\,I}}$ and $u_{2,\mathrm{p\,II}}$, for sensor orientation I and II, respectively; see Figure 4.4. The difference of $2\alpha_1 \geq 60°$ has been recommended for the extraction of two velocity components by [60] and [68]. A summary of the different sources contributing to error propagation are summarized by [96]. Several additional influences are caused by the test rig and the inclination of the sensor. These circumstances lead to a change of the interference

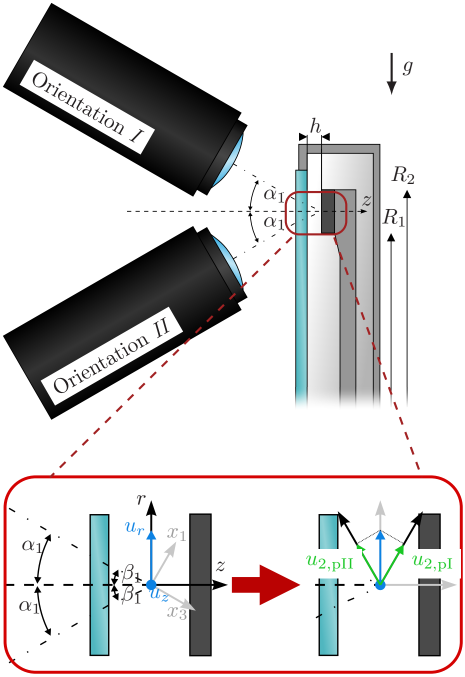
Orientation I
Orientation II
g
h
R_2
R_1
z
α_1
α_1
r
u_r
x_1
β_1
β_1
u_z
x_3
z
α_1
α_1
$u_{2,\mathrm{pII}}$
$u_{2,\mathrm{pI}}$

Figure 4.4: LDV set-up scheme with both orientations for the LDV-PS ($\alpha_1 = 30°$). The insert explains the conversion from the measured signal to the $\{r, \varphi, z\}$-system. The dominant u_r-component is positive (blue arrow) and the u_z-value tends towards zero (indicated as blue dot). u_φ is pointing orthogonal to the sketch plane. (Figure adopted from [LPK22].)

pattern for all components. The calibration curve as shown in Figure 4.2 could not be directly applied to the output z-position but some systematic deviation must be corrected to reach meaningful results. The main sources of deviation are summarized in the following. First, the glass plate lead to a shift of the actual sensor position in comparison to a purely geometric consideration as e.g. outlined by [89]. Second, the refractive index of the oil (and the glass plate) leads to an angular deviation, which must be addressed accordingly via a calculation with the law of refraction. The

Table 4.2: Orientation of the LDV-PS system against the z-axis to measure and/or determine the velocity components u_φ, u_r and u_z at the desired perimeter.

orient.	angle	meas. quantities	calc. quantities
I	30°	u_φ and $u_{2,\mathrm{p\,I}}$	u_r and u_z
II	−30°	u_φ and $u_{2,\mathrm{p\,II}}$	u_r and u_z

z-position of each detected particle is thus corrected. Additionally, the velocity information is transformed and corrected.

Table 4.2 shows the measured and calculated velocity components for clarity. The detected velocities of the second component can be divided into the radial and axial velocity according to

$$u_{2,\mathrm{p\,I}} = \cos\beta_1\; u_r + \sin\beta_1\; u_z \tag{4.2a}$$

$$u_{2,\mathrm{p\,II}} = \cos\beta_1\; u_r - \sin\beta_1\; u_z. \tag{4.2b}$$

As such, the measured velocities of each particle can be split into the radial and axial velocity component, which are then expressed as:

$$u_r = \frac{u_{2,\mathrm{p\,I}} + u_{2,\mathrm{p\,II}}}{2\cos\beta_1} \tag{4.3a}$$

$$u_z = \frac{u_{2,\mathrm{p\,I}} - u_{2,\mathrm{p\,II}}}{2\sin\beta_1}. \tag{4.3b}$$

Note that the refractive-index matched angle $\beta_1 = \arcsin(\sin\alpha_1/n_\mathrm{r})$ is applied in Equation (4.2) and Equation (4.3) to account for the fluid properties of the chosen oil.

Equation set (4.3) directly emphasizes the interplay between the consecutively recorded data sets, where any possible error comprised in the results from either sensor orientation, can immediately affect both determined velocity components u_r and u_z. Consequently, the quality of both calculated velocity components relies on both measured orientations.

The conversion from Equation (4.2) to Equation (4.3) is illustrated in the insert of Figure 4.4, which displays the smooth part of the gap without grooves for clarity." [LPK22]

4.2 Results

Since the aim of this study is a profound statement about the applicability of the used LDV-PS for shear-flow scenarios in thin rotor-stator gaps, two main interests are pursued for the analysis of the flow measurements. First, as already mentioned in section 4.1.1 the spatial uncertainty is a function of the ratio of both measured frequency uncertainties of the LDV-PS, so a detailed look for different velocities seems mandatory, but as yet remains pending for the profile sensor. For the present investigations such analysis, however, is of utmost importance, since a broad velocity range is present at the same time. So the findings of this section, in turn also influence the way the fluid flow experiments are executed.

4.2.1 Uncertainty considerations for velocity, space and angle

"For the spatial uncertainty study the mentioned $d_{\mathrm{w}} = 10\,\mu\mathrm{m}$ wire and *variant A* of the set-up was used; see Figure 4.3a. The uncertainty of z-direction is directly linked to the profile sensor function, while the φ-coordinate is allocated to the recorded LDV signals from the timing unit of the encoder. For this experiment the sample rate was fixed at 50 MHz and the signal window was set to 8K. The higher velocities could have been sampled with a smaller signal window, however all velocities are present

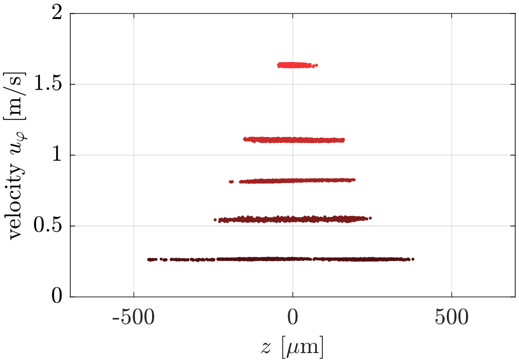

Figure 4.5: All measured wire velocities and positions for a constant record length. Higher velocities meet the expected spatial uncertainty, lower velocities reveal more location estimation scatter, thus requiring a broader sample size. (Figure adopted from [LPK22].)

in the gap flow, so fixed values for these quantities fulfill the applicational requirements. A more precise detection for the low velocities would be easily manageable with further extension of the sample rate and the signal window for each specific velocity range.

Figure 4.5 shows all detections of the wire for five different velocities and their calculated spatial locations. A clear trend to increasingly scattered location estimation is observed for lower velocities. Table 4.3 shows this variation of the results in terms of the standard deviation σ. Approximately 1500 wire detections have been recorded for each velocity to ensure statistical significance of the data evaluation process. Possible sources for the occurring scatter are a low signal-to-noise ratio of the light signal caused by strong reflections within the sub-millimeter gap; an unadjusted signal window for low velocities, which leads to an undersampled frequency signal and vibrations caused by the test rig in this slightly rough industry-related scenario. The uncertainty can be systematically diminished with a high number of overall detections in the low velocity regime, which will be considered for the flow measurements. As a result from the above insight –

Table 4.3: All measured wire velocities with corresponding standard deviations of location and velocity.

velocity u_φ [m/s]	z^σ [µm]	${u_\varphi}^\sigma$ [m/s]
0.27	185	0.0042
0.55	129	0.0042
0.82	82	0.0046
1.11	80	0.0059
1.64	19	0.0057

the measurements of the fluid flow have been partitioned into measurement ellipsoid lengths of 600 µm, as already indicated in the previous section, thus matching every velocities range with suitable parameters. This partially compensates the high uncertainty for low velocities.

An additional determination strategy arises from the scattered data of Figure 4.5 in terms of possible averaging methods. In principle averaging in space or velocity is possible, where either the determination of the velocity statistics can be performed for a given spatial binning of the data, or – vice versa – the location statistics can be determined for preset velocity bins. For low velocities definitively an average over certain velocity bins make sense, since this quantity varies much less compared to the spatial distribution. Additionally, a velocity averaging doesn't coop with this strong change in uncertainty, which improves the averaging results in general. Averaging in space appears suitable, when the velocity is high enough and the possible arising error can be considered as small enough for the examined flow. For more complex flows and flows with a non-injective functional space-velocity relationship (e.g. local maxima/minima) more elaborated evaluation strategies appear suitable. Particularly, the application of fitting functions and/or advanced averaging methods, which e.g. combine velocity and spatial averaging relative to the occurring gradients, can be envisioned. In the present context the flow in the groove reveals a local velocity maximum slightly higher than the rotational velocity of the disk and thus only a weakly-pronounced gradient in z-direction, as further elaborated below. Consequently, a 4^{th}-order polynomial has been chosen to approximate the velocity distribution.

Since the spatial location as the most crucial quantity is discussed sufficiently, the following part focuses on all velocity and spatial components that were conducted with *variant A* of the set-up and are essential for the considered flow scenario. Figure 4.6 shows multiple histograms of all extracted results for a nominal angular velocity of $\Omega = 12.57$ 1/s in detail. To compare the possible errors and their propagation, the standard deviation of the stepping motor was specified by the variation of the light barrier signal, which was additionally fed into the LDV software. The mean frequency and corresponding standard deviation results in $f_\mathrm{m} = 1.9951 \pm 0.00015\,\mathrm{Hz}$, which corresponds to a standard-deviation contribution of $u^{\sigma}_{\varphi,\,SM} = 0.000083\,\mathrm{m/s}$ of the stepper-motor variation within the u_φ-histogram.

As shown in Figure 4.6a and 4.6b the circumferential and radial velocities were detected with low uncertainties, as expected for LDV systems. Although the u_φ-component features the *profile sensor* function with four partial laser beams, the velocity uncertainty is within the same range as for the u_r velocity, which is provided by a classical LDV system (cp. Figure 4.1). An expected higher velocity in the groove of 5% compared to the disk velocity, as uncovered by [LFMK21], equals a $\Delta u_{\varphi,\mathrm{OS}}$ of 0.055 m/s in this flow scenario, which is around 10 times higher than the standard deviation. In conclusion this quantity for clutch flow pivotal element is expected to be resolved accordingly even for fairly low disk velocities which were chosen in this study.

Figure 4.6c presents the uncertainty distribution of the phase angle φ. Here only six different values with a difference of $\Delta\varphi_\mathrm{theo} = 0.029°$ of the

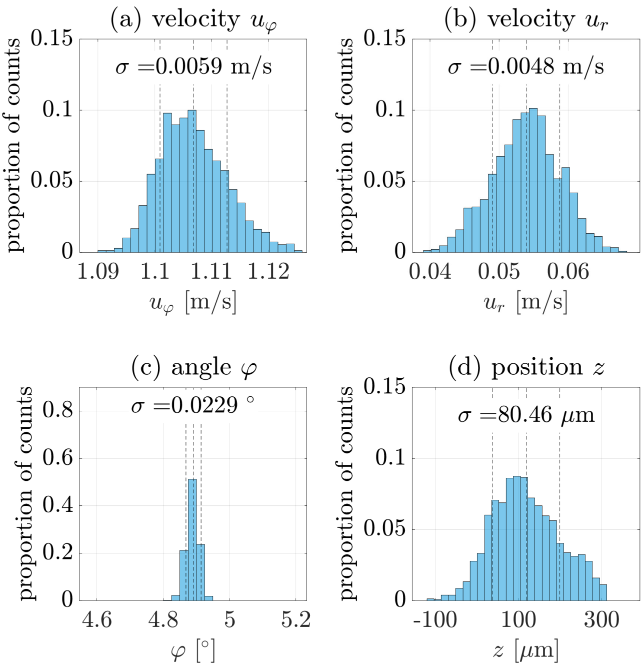

Figure 4.6: Proportion of counts for the most important quantities received for the wire experiment (diameter $d_\mathrm{w} = 10\,\mu\mathrm{m}$, nominal angular velocity $\Omega = \partial\varphi/\partial t = 12.57$ 1/s, radial position on the disk $R_\mathrm{m} = 88.1\,\mathrm{mm}$). (a) circumferential velocity u_φ; (b) radial velocity u_r; (c) circumferential angle φ; (d) spatial position z within the gap. (Figure adopted from [LPK22].)

10 µm wire have been distinguished, which renders a possible theoretical uncertainty of $\Delta\varphi_\mathrm{theo}R_\mathrm{m} = 44.6\,\mu\mathrm{m}$. Compared to the groove width W as characteristic length scale in circumferential direction the relative uncertainty is $\Delta\varphi_\mathrm{theo}R_\mathrm{m}/W = 0.033$. Hence, approximately 30 different positions can be distinguished within the groove, which leads to a sufficient resolution for the given flow scenario.

The constant z-position of the 10 µm diameter wire has been detected with a standard deviation of $z^\sigma = 80.46$ µm at a wire velocity of 1.11 m/s; see

Figure 4.6d. This measure indicates only limited uncertainty, when compared to the gap height of $h = 320\,\mu\mathrm{m}$ as characteristic length scale in z-direction. The relative uncertainty of $z^\sigma/h = 80.46\,\mu\mathrm{m}/320\,\mu\mathrm{m} = 25\%$ for the 1300 registered burst from the wire, emphasizes the necessity to further evaluate the required sample number. For the given problem, a relative uncertainty of 5% is considered sufficiently accurate, which corresponds to an absolute error of 16.0 µm. Consequently, more than 97 individual measurements are required assuming a Gaussian error distribution." [LPK22]

Since this number is rather low, this result was further cross-checked with a t-distribution, which is qualified for low sample experiments [93]. The outcome of this test leads to the exact same result of 97 independent data points. This kind of *in-operando* evaluation can also serve as ad-hoc procedure during the measurement procedure to determine the required number of registered particles to achieve sufficiently accurate results.

The above findings and insights demonstrate an unrestricted applicability of the LDV-PS for the desired area of application with regard to the general measurement uncertainty – given a sufficient amount of data points is detected regarding the scattering of the measured quantities, as the measured values show even Gaussian distributions. In the following part, now the revealed velocity information of the clutch flow measurements is analyzed in detail to gain a deeper insight into the cause-effect relations of the considered open wet clutch flow. To do so, first the expected flow topology is stated.

4.2.2 Expected flow topology

To characterize the obtained velocity data the following subsection discusses the expected flow for the smooth part of the disk and the region,

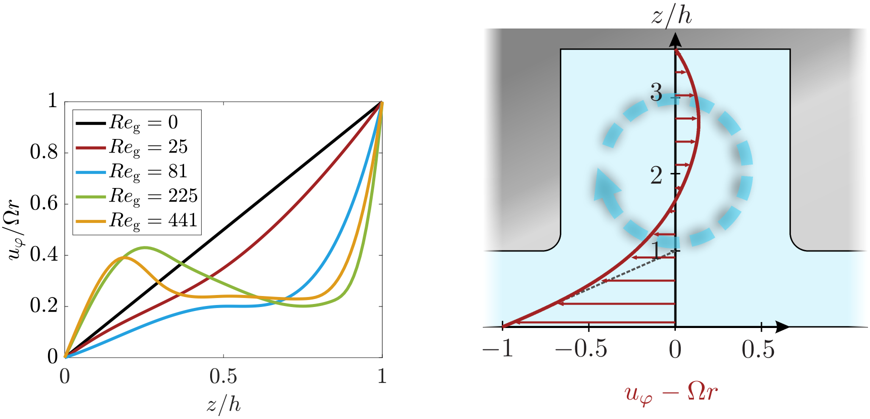

(a) **(b)**

Figure 4.7: (a) Gap profile of normalized circumferential velocity for various gap Reynolds numbers Re_g. Adapted from Lance & Rogers [54]. (b) Sketch of the expected velocity profile (in a disk-fixed coordinate system) in the radial groove. The cavity roller as principle of explanation is added for clarity. The dashed line shows the linear Couette flow as comparison.

where the groove is present. As already shown in Chapter 3 for the analytical consideration a linear velocity profile in circumferential direction seems plausible for a smooth gap.

To extend the already found linear interrelation Figure 4.7a shows the Reynolds-dependent normalized gap profile of circumferential velocity. Various gap Reynolds-numbers $Re_g = \Omega h^2/\nu$ are depicted in the diagram. Lance & Rogers [54] found a self-similar solution, which oversimplifies the different regions as already shown in Figure 2.3, but offers deeper insights into the flow profiles of the circumferential velocity. For the clutch flow, however, the expected flow velocity of a linear Couette-like flow seems adequate.

For the groove part Figure 4.7b shows the expected circumferential flow velocity as shown in [LK19]. The velocity is plotted in the middle of the groove in a disk-fixed coordinate system. A so-called cavity roller is present in the groove and causes the flow to locally increase above the disk velocity in the groove's rear part. At lower z-values this vortex accordingly leads to lower velocities compared to the linear Couette-like flow to fulfill continuity.

4.2.3 Clutch flow measurements

"Figure 4.8 shows the detected particles (blue dots) in a $z-u_\varphi$-diagram for $\varphi \in [7°, 11.25°]$, corresponding to a smooth region of the disk sufficiently displaced from the groove. The dashed black line shows a linear profile for comparison. The revealed linear Couette-like velocity profile is characteristic for the smooth regions of the clutch gap at low rotational velocities as elaborated by [54], for instance. Moreover, the superimposed red bullets show the respective standard deviation z^σ of the location estimations from the wire experiment for the tested velocities, as summarized in Table 4.3.

Figure 4.9 provides an overview of the detected particles and determined quantities within one of the 32 groove-to-groove sections. Particularly, the spatial distribution across the section is shown in Figure 4.9a in a normalized $\varphi - z$ coordinate system for all particles. The physical dimensions of the gap and the groove are illustrated for clarity. The φ-coordinate can be resolved sufficiently precise, so that the start and end of the groove, namely $\varphi R_\mathrm{m}/W = 0$ and $\varphi R_\mathrm{m}/W = 1$, can be located. The origin of the φ-coordinate is set to the left side of the groove and normalized with R_m/W, for further clarity. In addition, the detected particles in the groove region appear color-coded along the φ-coordinate, to distinguish different slices of the flow for further (color-coded) evaluation of the averaged velocity profiles.

Particle velocities and locations across the gap and in the groove are shown in Figure 4.9b in a normalized $z - u_\varphi$ coordinate system, which comprises particles from both the smooth and the grooved parts. As before, the rotor velocity of ΩR_m can be identified in the diagram such that particles within

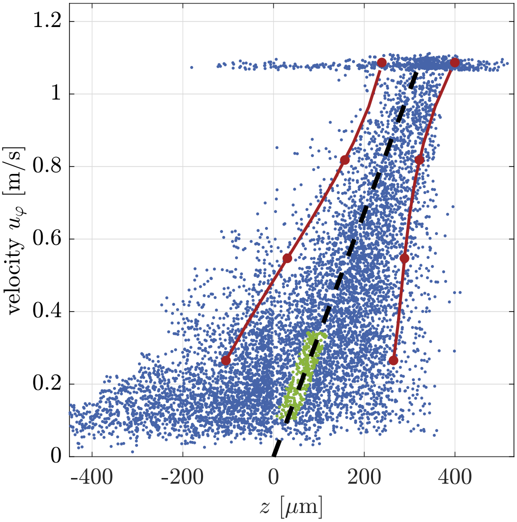

Figure 4.8: Velocity component u_φ and z-position of all detected particles of the flow measurements in the smooth part of the gap flow (●) superimposed to the standard deviation z^σ for different velocities u_φ of the conducted wire experiment (●). The green particles (●) indicate the region, which is considered for the wall shear stress measurements in subsection 4.2.4. (Figure adopted from [LPK22].)

this small velocity band were excluded for subsequent average-velocity calculations. The particle distributions demonstrate that the velocity in the groove region is well below ΩR_m at the gap-groove interface and then advances beyond the rotor velocity well in inside the groove cavity. This intra-groove vortex system has already been identified by [LFMK21] and was referred to as *cavity roller*. The corresponding velocity field becomes particularly obvious from the color-coded angular-averaged velocity profiles inside the groove.

The mean velocities arise from a fitting function of higher order, which originates at $(0, 0)$. A simple piece-wise averaging would lead to a inaccurate representation of the flow, so a more complex combination seems suitable for this flow scenario.

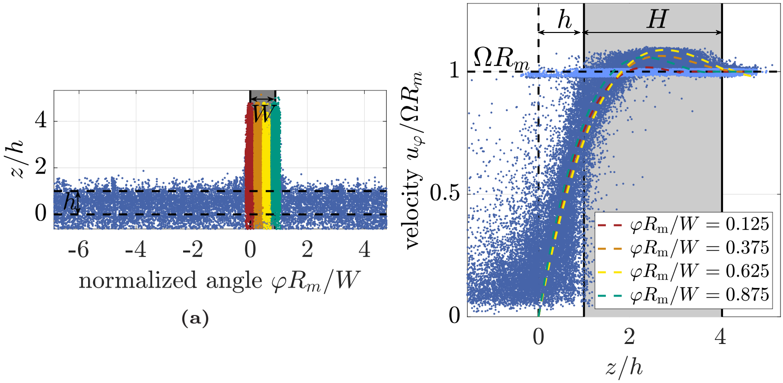

(a)

(b)

Figure 4.9: (●) Registered particles across circumference and in the gap region; (a) particle locations for one section $\varphi = 7° - 18.25°$. The particles in the groove are color coded and the dimensions W (groove width) and h (gap height) are added for comparison. The dashed lines show $z/h = 0$ and $z/h = 1$. (b) $u_\varphi(z)$ velocity profile for all registered particles within the groove section and fitted profiles for the four color-coded slices of Figure 4.9a. Additionally added: groove width W, groove height H, gap height h and the dashed line at ΩR_{m}. (●) Detections originating from the rotor are excluded for further calculations. (Figure adopted from [LPK22].)

Figure 4.10 provides a comprehensive flow-field overview of all three velocity components for the selected groove-to-groove section in a normalized $\varphi - z$ coordinate system, showing each velocity component separately as contours. For visual purposes only one periodic section of the 360°-distribution with 32 grooves is shown. The circumferential velocity component is shown in Figure 4.10a and reveals a *Couette-like* flow in nearly the complete gap. This insight is valuable information for clutch manufacturers, which up-to-now was missing in literature. The findings now substantiates existing clutch flow models with experimental data (cp. e.g. [44]). Interestingly, the *Couette-like* distribution is only disturbed in vicinity of the groove. A reasonable approach for further in-detail studies might therefore focus on the region in the range of one groove width W up- and downstream of the groove (i.e. $\varphi R_{\mathrm{m}}/W \in [-1, 2]$) for the influence of radial grooves.

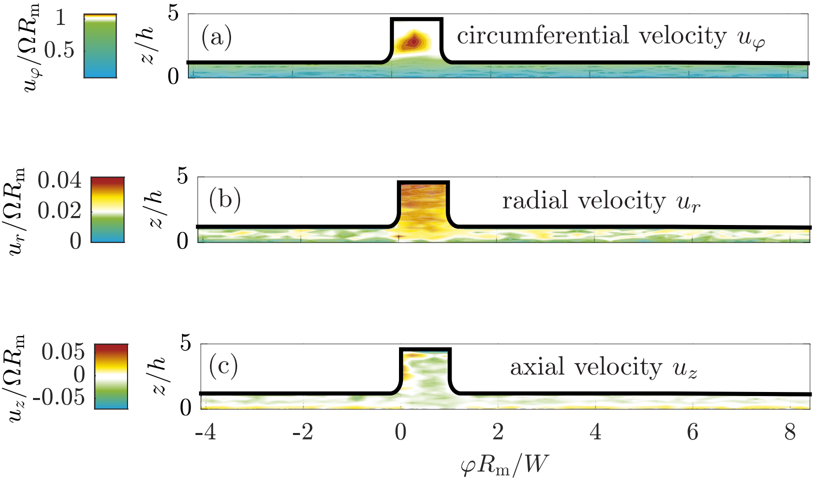

Figure 4.10: Overview of the selected flow field. Contours in a $\varphi - z$ coordinate system of normalized circumferential, radial and axial velocity components, namely u_φ, u_r, u_z. (Figure adopted from [LPK22].)

An additional aspect of the flow-structure investigation is the slightly higher circumferential velocity in the groove compared to the disk velocity. This region belongs to the above-mentioned occurrence of the cavity roller, which results from the fact that the radial groove of the present investigation is oriented perpendicular to the shear-flow direction in the gap. The cavity vortex is not limited to the groove but expands into the gap. In accordance with earlier observations by [LFMK21] the highest circumferential velocity can be found in the groove's rear part and has a value of 6% above ΩR_m. As a counterpart of a higher velocity at the groove's bottom, fluid with lower velocity than ΩR_m expands into the anterior part of the groove (cp. color-coded profiles in Figure 4.9b).

The conversion of the second recorded component u_2 from two consecutive measurements into radial and axial velocity components u_r and u_z

via equation set (4.3) has been successfully applied, such that either component can be evaluated separately. The angular-resolved radial velocity component is shown in Figure 4.10b. The values are located in the range of 0 and 0.04 ΩR_{m}, with values of the smooth gap region in the lower range. The velocity at the rotor and stator tends towards zero, while the values in the middle of the gap shows slightly higher velocities. This finding supports the fact that a radial outflow is present due to moderate centrifugal forces of the rotor, which for the given parameters counteracts the flow induced by gravitational forces. An additional valuable information is the higher radial outflow velocity in the groove, which is about twice as high than the smooth-gap counterpart. The highest values of around $3-4\%$ of the disk velocity can be found in the posterior part of the groove. This is in consistency with the centrifugal forces, since also the highest values of circumferential velocity is detected in this part. The findings support the fact that the radial flux is mainly dominated by the flow in vicinity of the groove and should be focused on predominantly for aeration predictions of open wet clutches.

Finally, Figure 4.10c reveals the axial component, as likewise calculated from the equation set (4.2). The determined velocities largely range around zero in the smooth part of the gap. As for the groove region, however, clear patches of non-zero velocity can be identified, which are comparable in magnitude to the observed circumferential velocity deviations from ΩR_{m} inside the groove. These maxima are indeed mandatory to fulfill continuity of the cavity vortex. The highest velocity is located on the left side of the groove, which indicates a clockwise rotation of the cavity roller in the diagram.

4.2.4 Wall-shear stress determination

The potential benefit lies in the angular resolved manner of the LDV-PS, so that the influence of the respective groove patterns and correspondingly occurring flow patterns can be quantified along the entire circumference.

To evaluate this foot print on the resulting drag torque, only the circumferential component is to be considered for the wall shear stress (WSS, τ_{w}) calculations, which leads to

$$\tau_{\mathrm{w}} = \mu \left. \frac{\partial u_{\varphi}}{\partial z} \right|_{z=0} \tag{4.4}$$

for the given rotor-stator shear flow. The idealized linear Couette-flow assumption in fact is an oversimplification that can be applied for very low rotational velocity components and small gap heights, as already elaborated by [19] and recently confirmed experimentally by [LFMK21] for the given clutch flow scenario. Even though an ideal rotational Couette flow, consequently, is not present in this gap flow scenario – neither in the smooth part, nor the groove – the linearized profile nonetheless serves as reference, which is defined as

$$\tau_{\mathrm{w,\,lin}} = \mu \frac{\Omega R_{\mathrm{m}}}{h}. \tag{4.5}$$

To account for the mildly non-linear character of the velocity profile while maintaining a robust estimate for the WSS, a linear fit of the circumferential velocity u_{φ} in proximity of the stator in the range $z \in [70; 100]\,\mu\mathrm{m}$ has been chosen for the determination of τ_{w}. Since the velocity is low in this region and the scatter around the mean velocity is accordingly strong compared to higher velocities, a direct extraction of the WSS might be heavily biased by location-estimation outliers; see Figure 4.8. To overcome this issue, the standard deviation as occurs for higher velocities has been chosen as robust filter margin around the linear Couette-approximation, to eliminate these outliers from velocity fluctuations. Consequently, the data were filtered with a validation margin of $\pm 19\,\mu\mathrm{m}$ in z-direction compared to $\tau_{\mathrm{w,\,lin}}$, to avoid a biased result. Figure 4.8 shows this region visualised with green data points for an easier comprehension. The extracted data points are binned to $\varphi R_{\mathrm{m}}/W = 0.5$ sections. Despite good overall angular

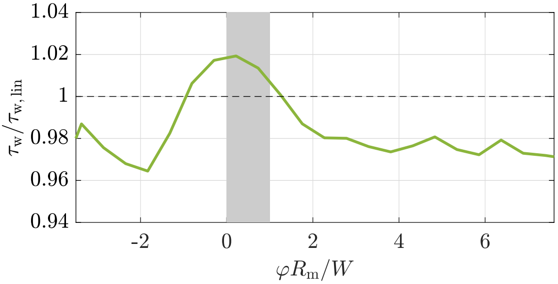

Figure 4.11: Angular resolved wall shear stress (WSS) distribution (—). The WSS for the smooth part of the gap is around 3% lower, compared to the WSS of an ideal linear profile (– –). The WSS in the vicinity of the groove (■) is significantly higher, due to the edge and the cavity roller. (Figure adopted from [LPK22].)

resolution of $\Delta\varphi = 0.029°$ and preserved full resolution over the disk revolution, this binning appears rather coarse in comparison with the groove width W. Consequently, the formerly hidden complete groove-to-groove picture of WSS, comes at the price of (circumferentially) low-pass filtered extraction of intra-groove structures and resulting variations of WSS in terms of accordingly diminished $\partial\tau_{\mathrm{w}}/\partial\varphi$ resolutions.

Figure 4.11 shows the extracted normalized and angular-resolved WSS τ_{w}. In accordance with earlier findings by [LFMK21] the WSS values are found to be around 3% on average below the linearized $\tau_{\mathrm{w,\,lin}}$ in the smooth region of the gap, far enough from the groove. Assuming a constant value in this part the uncertainty of the WSS yields $\sigma = 1.29\%$, which – due to the lack of an additional reference experiment – can only serve as an estimate. Despite the relatively high uncertainty the higher value in the region of the groove can be resolved accordingly. The values are found to be 2% above the reference value of $\tau_{\mathrm{w}}/\tau_{\mathrm{w,\,lin}} = 1$, which – even though circumferentially low-pass filtered – preserves the observed trends from [LFMK21]. The highest value appears at the left side of the groove, which confirms the above-stated recommendation to consider the up- and downstream proximity of the groove in the range $\varphi R_{\mathrm{m}}/W \in [-1, 2]$ to study the influence of radial grooves on the WSS and, thus, the impact on overall drag torque.” [LPK22]

4.3 Concluding remarks (regarding LDV profile sensor technology)

The present chapter evaluates the applicability of an angular-resolved and Bragg- shifted laser Doppler velocimetry profile sensor for open wet clutch flow scenarios. The technique is a promising approach to extract velocity and wall-shear stress estimations of the flow. “The location-estimation uncertainty revealed a standard deviation in z-direction of 19 µm at 1.6 m/s. For the data processing of particles with very slow velocities it turned out that a determination of location estimates for individual velocity bins out-performs the velocity estimation for spatial bins. The resulting flow maps for all three velocity components reveal the flow topology in the gap and the revolving grooves along the rotor circumference, which is mainly comprised of a Couette-like shear flow in the gap and cavity roller forming superimposed to significant radial fluxes in the radially oriented grooves. Since the particles have been detected with an uncertainty of 0.029° – corresponding to 44.6 µm for this flow scenario – 30 different spatial positions in the groove can be distinguished in circumferential direction.” [LPK22] This resolution provides confidence for accurate topology analyses by means of LDV-PS, however lacks of an in-detail intra-groove analysis. ”As a final remark, the results of this study clearly emphasize the suitability of LDV-PS as a candidate technique for industry-relevant flow-diagnostics applications. Moreover, due to the fact of an angular-resolved detection, the LDV-PS measurement technique serves as highly-suitable means to uncover the global picture of the flow topology and moreover track the WSS across the circumference. In cases where higher spatial resolution is required the LDV-PS results might be supplemented with inherently more precise techniques, such as defocusing particle tracking velocimetry

(DPTV), for instance. Complementary application of both LDV-PS and DPTV is, therefore, considered as a landmark combination to provide substantial additional value for open clutch flow scenarios and moreover to rotor-stator gap flows in general." [LPK22]
To tackle the problem of a higher spatial resolution complementary the next chapter introduces DPTV as means to extract velocity and WSS data in and around a radial groove.

5 Defocusing Particle Tracking Velocimetry - intra-groove analysis

This chapter is based on the journal publication *Flow-structure identification in a radially grooved open wet clutch by means of defocusing particle tracking velocimetry* [LFMK21]. Where findings were already published, this is clearly marked and indicated as related quotations. Changes within these quotations are only made for a consistent nomenclature.

The fundamentals for the given approach have been already recapped in Chapter 2. Only application-inherent fundamentals and specific technical details are recapitulated here, which are necessary for an understanding of the results.

5.1 Set-up specific background on Defocusing Particle Tracking Velocimetry

As already outlined in Section 2.3.2 “defocusing information of the particle images allows for the determination of the spatial particle location along the optical axis, a principle that has long been practiced in particle imaging since its introduction by [99]. DPTV is a straightforward technique that only requires a simple planar PIV equipment to determine the volumetric flow field. While Defocusing PTV is not a standard technique – there is no commercial software available – it is a powerful method for applications where planar PIV is not suitable. Whenever it is necessary to resolve flow structures with dimensions on the order of the light sheet thickness or even smaller, it is necessary to conduct three-dimensional (3D) flow velocimetry. Naturally, multi-camera approaches, such as 3D-PTV [63] and tomographic PIV [21], are employed in such cases, since these are well-established and assessed techniques. However, when it comes to technical applications, the geometries of the domains can become more complex, vibrations can occur, and the accessibility of the measurement area may be limited. Such challenging measurement environments might leave the DPTV approach as the only remaining option to derive reliable velocity information at all." [LFMK21]

Recall from Section 2.3.2 that the particle location along the optical axis – in this set-up the z coordinate – is coded in the geometry of the particle image, more specifically in the diameter. This concept has already been visualized in Figure 2.6 to emphasize the relation between the distance of a particle to the focal plane and the resulting particle image diameter. "Closer to the focal plane the particle image diameter becomes smaller, whereas if the particle is located further away from the focal plane, the particle image diameter increases. In x and y direction the particle location is determined by the sensor location of the particle image center, provided that the scaling function does not change along z. For macroscopic objective lenses and small measurement depths as well as for micro objective lenses this is a valid assumption; for macroscopic experiments at larger measurement depths the particle x and y location becomes a function of the sensor location and the particle z location, or the particle image geometry, respectively, as outlined by FUCHS *et al.* [25].

The particles used in the present study have a mean diameter of $d_\mathrm{p} = 9.84\,\mu\mathrm{m}$ and a standard deviation of the diameter of $\sigma = 0.26\,\mu\mathrm{m}$. Figure 5.1 shows d_i in pixel on the sensor chip calculated according to equation (2.11). The gray lines visualise the uncertainty of the diameter, as 3σ-deviation. It can be concluded from the narrow margin between the lines, that the influence of the physical particle-size deviation and its variation along the z location have no significant influence on the image diameter

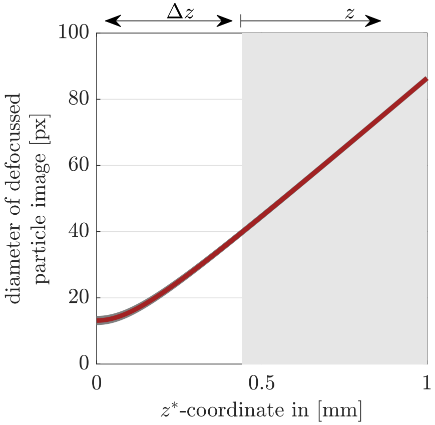

Figure 5.1: Visualisation of Eq. (2.11) for the input parameters of the present particle imaging approach. The red curve shows the image diameter d_i of the mean particle diameter as function of z^*. Physical particle-size deviations are emphasized as a dark gray 3σ margin. This margin vanishes for reasonable distance to the focal plane. (Figure adopted from [LFMK21].)

estimation for reasonable distance to the focal plane. In practice, the focal plane is located outside of the measurement volume in the direction closer to the camera to ensure sufficient accuracy for the approximated linear relation between the particle image diameter and the particle z^* location and furthermore to eliminate any influences of the particle diameter.

Equation (2.11) does not take optical aberrations into account, which renders a direct application of this function for particle-location estimations impossible. For objective lenses with large magnifications, in particular, spherical aberrations have a strong influence on the defocusing function. One means to determine this function is the use of pinhole matrices that are imaged at distinct z positions along the measurement domain, since the pinhole images form the same diffraction pattern as particles of the same diameter (Babinet's principle). In the present clutch-flow application it is not feasible to place a calibration target within the domain. Instead, the defocusing function is derived from the displacements of the recorded particle images, where the particle image diameters at the upper and lower boundary of the measurement volume are estimated on the grounds of the no-slip condition. Since the particle image diameter is considered to change linearly with the particle z location within the volume boundaries (see above), the particle location relative to the gap height can be immediately scaled using the known height h of the bounded measurement volume. This yields a simple linear relation between the particle z location and its particle image diameter d:

$$z = s^Z \, d, \tag{5.1}$$

where s^Z is the slope of the defocusing function. A more detailed description of the *in situ* calibration procedure – including methods on how to compensate a camera misalignment and field curvature – is outlined in [26].

The actual displacement of the particle images is determined by a simple nearest neighbour tracking algorithm, since the particle image density is fairly low due to the relatively large defocused particle images. Along with the sensor location X and Y of the particle image, the available diameter estimate is directly used for the third spatial location component, allowing for the connection of corresponding particle image pairs in 3D space.

5.2 Experimental procedure

All experiments were conducted at an open wet clutch facility, which provides optical access through the stator plate and a circumferential window in the clutch housing, see Figure 5.2. The stator plate is made from anti-reflection coated float glass to ensure a high quality, low distortion optical access to the measurement domain. Its rotating counterpart can be exchanged to test different groove patterns or non-grooved rotor clutch plates. The clutch was operated at an angular velocity of $\Omega = 20.1$ 1/s with a constant moderate radial volumetric flow rate of 1.0 l/min to ensure

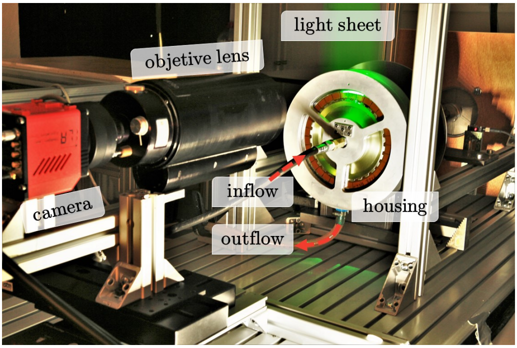

Figure 5.2: Picture of the experimental set-up comprised of the clutch model, laser light source and imaging equipment. (Figure adopted from [LFMK21].)

a single-phase flow. Repeatability of the experiments in terms of constant rotor speed and reasonably accurate phase resolution for the present case of a grooved rotor disk is ensured by an *ADDA TFC 80A-2* motor in combination with a *WL100L-F2231* optical sensor.

The clutch was operated with a white mineral oil (density $\rho_o = 850\,\mathrm{kg/m^3}$, dyn. viscosity $\mu = 0.0136\,\mathrm{kg/ms}$ at $40°C$, CAS No: 8042-47-5), which was seeded with fluorescent particles with a mean diameter of $d_\mathrm{p} = 9.84\,\mathrm{\mu m}$ (density $\rho_p = 1510\,\mathrm{kg/m^3}$, particle response time $\tau_p = 0.6\,\mathrm{\mu s}$, emission wave length $\lambda_e = 584$ nm) to avoid reflections. The measurement volume was illuminated using an *ILA_ 5150* light-sheet optics in front of a *Quantel Evergreen* Nd:YAG laser ($\lambda = 532\,\mathrm{nm}$, $70\,\mathrm{mJ/pulse}$, pulse distance $\Delta t = 80\,\mathrm{\mu s}$). The particles were recorded in double-frame mode once per revolution, using an *ILA.PIV.sCMOS* camera (sensor size 2560×2160 pixel, 16 bit) equipped with a *Questar QM 100* long-distance microscope.

Note that the Defocusing PTV equipment is identical to a standard 2D planar PIV setup, where the only difference is the distinct offset between light sheet and focal plane. Here, the small focal depth of the *Questar* ensured a large defocusing sensitivity and in turn a good spatial resolution

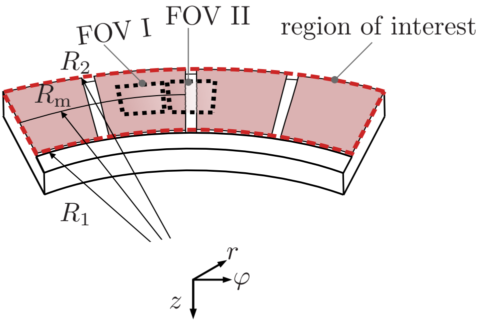

Figure 5.3: Location of the two fields of view. FOV I is located midway between two grooves. FOV II captures the groove region. In radial direction, the center of the FOVs is aligned with R_m. (Figure adopted from [LFMK21].)

along the optical axis. As indicated in Figure 5.3 phase-triggered experiments at two fields of view (FOV) have been conducted to compare the flow in the smooth part of the gap (FOV I) with the impact of a radially grooved cavity in the disk surface on the flow field (FOV II). A total number of 2000 image pairs was recorded for each FOV and magnification.

The optical set-up for FOV I and II has a magnification of $M = 7.0$ and a reproduction scale of 0.92 µm/pixel. This configuration provides a defocusing sensitivity of $s^Z = 11.6$ µm/pixel, which corresponds to a 1 pixel diameter change of the particle image for a particle location change of 11.6 µm along the optical axis in z direction. Additionally, a smaller magnification of $M = 4.2$ with 1.55 µm/pixel reproduction scale and $s^Z = 19.71$ µm/pixel defocusing sensitivity was used for FOV II to account for the larger depth of the measurement volume in the cavity and to provide a broader view on the cavity/gap interaction of the flow.

Starting from a diameter of around 50 pixel at the transparent stator wall, the chosen magnifications yield particle image diameter increases of around 30 and 50 pixel along the gap height of $h = 0.54$ mm for FOV I and FOV II, respectively. To avoid confusion, all upcoming diagrams provide information on the chosen magnification. The boundary conditions for the particle image diameter calibrations are (a) $u_\varphi(z = 0) = 0$ at the stator wall, (b1) $u_\varphi(z = h) = \Omega r$ at the smooth part the rotating disk (FOV I) and (b2) $u_\varphi(z = h + H) = \Omega r$ within the groove of the disk (FOV II).

The clutch facility was operated with a real industry-used rotor disk to ensure a realistic and meaningful test scenario. The inner and outer radii of the chosen disk are $R_1 = 82.5$ mm and $R_2 = 93.75$ mm, respectively. The 32 equidistantly distributed grooves lead to a groove-to-groove distance of 17.3 mm in circumferential direction at the mean disk radius R_m, where the latter also denotes the approximate center line of the chosen FOVs; see Figure 5.3. The corresponding gap Reynolds number for the given quantities is $Re_h = \Omega h^2/\nu = 0.36$ [see e.g. 54], where $\nu = \mu/\rho$ is the kinematic viscosity. Likewise, the lubrication Reynolds number for the given problem is $Re_l = \Omega R_m h/\nu = 59.7$, which is commonly used for tribology and (mixed) lubrication problems [cp. 31, 95]. According to [54], a *Couette-like* velocity profile in circumferential direction can be expected in gaps of smooth rotor-stator configurations for gap Reynolds numbers $Re_h < 1$, which holds for FOV I of the present set-up. Note however, that even such low Re_h lead to slightly curved velocity profiles, which reveal increasing velocity gradients towards the rotor [54].

Figure 5.4 shows a detailed sketch of the radial groove geometry, also containing the origin of the coordinate system with the coordinates r, φ, and z. In the present application the z direction also corresponds to the optical axis and represents the particle location along the gap height h with its origin $z = 0$ at the stator glass plate (cp. also Figure 5.1). The radially oriented clutch grooves have a width of $W = 1.35$ mm in circumferential direction and a height of $H = 0.97$ mm in axial direction.

5.3 Results

5.3.1 Comparative particle image detection analysis

Deriving the spatial particle location from its particle image geometry is a crucial step for the single camera 3D DPTV velocimetry technique, since the uncertainty of the particle location estimation is directly connected to the accuracy of the particle image geometry determination. In microfluidics, where objective lenses with relatively large spherical aberrations are used, the auto-correlation function, defining the particle image boundary by a fixed correlation value, has shown to yield the best results for the geometry determination, as proven by [15]. The latter study showed that a Gaussian fit is not suitable to determine the particle image geometry, since the particle image intensity distribution is not Gaussian-like, even though the peak intensity is still in the center of the particle image. Another micro imaging approach to determine the particle image dimensions was outlined by [7], where the particle images are cross-correlated with a

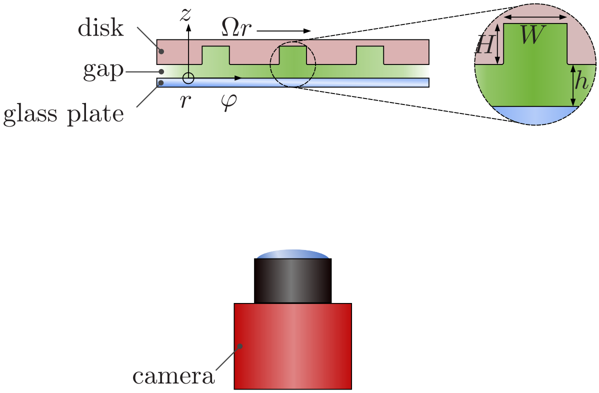

Figure 5.4: Sketch of the measurement volume between the glass plate (stator) and the radially grooved rotating disk; the relevant geometry parameters are added to the sketch. (Figure adopted from [LFMK21].)

set of reference images, recorded at well-known positions along the optical axis, to estimate their spatial location.

However, the significance of spherical aberrations is not as pronounced for macroscopic imaging, since the deviation from the ideal spherical wave front of a point source of light due to the aberration becomes small.

As a consequence, the peak intensities of the particle images are not located in the center anymore. Instead the highest intensity appears at the outer rim of the particle image, which was first employed by [100] to estimate the particle image diameter. Analogously, [25] determined the particle image geometry by analysing the intensity distribution at its edges, where a fixed intensity value denoted the edge location. This method was later refined for the *in situ* calibrated defocusing approach, where a normalized intensity value, accounting for local intensity variations and noise, defined the particle image edge [see 26].

The optical set-up used in this investigation can be categorized between the microscopic and macroscopic set-ups that were introduced in the previous paragraphs. Figure 5.5 clearly illustrates that the highest intensity of the particle images is at their outer diffraction ring, while compared to the investigation of [26] the outer ring spreads over several pixels rather than forming a sharp edge; note that the intensity is inverted in the figure. To account for this particle image appearance during geometry determination, [LK19] successfully demonstrated the application of the Hough transform [40], which is an efficient method to detect circular shapes.

The remainder of this section addresses the comparison of the algorithms of [LK19] and [26], where the latter has so far only been employed for a generic lab experiment and remains yet to be testified in more realistic and complex technical applications. From here on, the approaches will be referred to as *circle detection* [LK19] and *edge detection* [26] approach, and will be compared in terms of their performance (i.e. the amount and local distribution of detected particle images), peak locking effects, and the uncertainty of the particle image geometry determination.

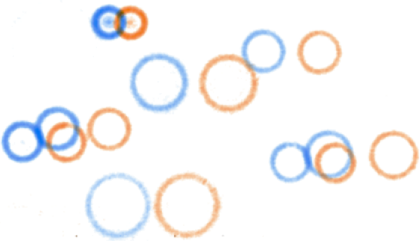

Figure 5.5: Random double frame raw image, color-coded and inverted for clarity. blue: frame 1; orange: frame 2. The circle pairs directly indicate larger particle displacements with increasing distance from the focal plane. (Figure adopted from [LFMK21].)

The total number of detected particle pairs in FOV I is 12,860 for the circle detection method and 14,718 the edge detection approach. The estimated particle image diameters and particle image displacements are shown in Figure 5.6. The detected particle image diameters are indicated in 5.6a for three particle images at different locations z in the gap. Obviously, the circle detection identifies the intensity maximum as the characteristic diameter of the ring-type pattern, whereas the edge detection considers the outer rim of the bright pattern for the diameter determinations. This systematic difference leads to correspondingly two different slopes for the respective diameter/displacement transfer functions of the *Couette-like* flow in FOV I as plotted in Figure 5.6b, which accordingly reveals a steeper slope for the edge detection algorithm.

Therefore, the particle displacement rather than the image diameter is considered for the direct comparison of detection occurrences along the gap as shown in Figure 5.6c. Both histograms show decreasing detection rates for increasing particle displacements, where a sudden steeper drop in detection rate for the circle detection is salient for the largest particle displacements. Recall that zero displacement occurs at the stator wall, which is closer to the focal plane. As such, the negative slope of the detection rate can be attributed to the decreasing signal to noise ratio (SNR) of the particle images, since the light intensity emitted by the particle spreads

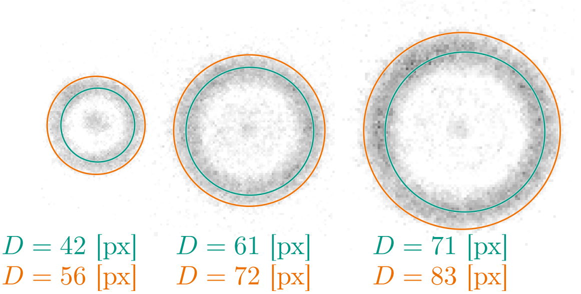

(a) Three particle images at different locations z in the gap; detected circle diameters of either approach are added.

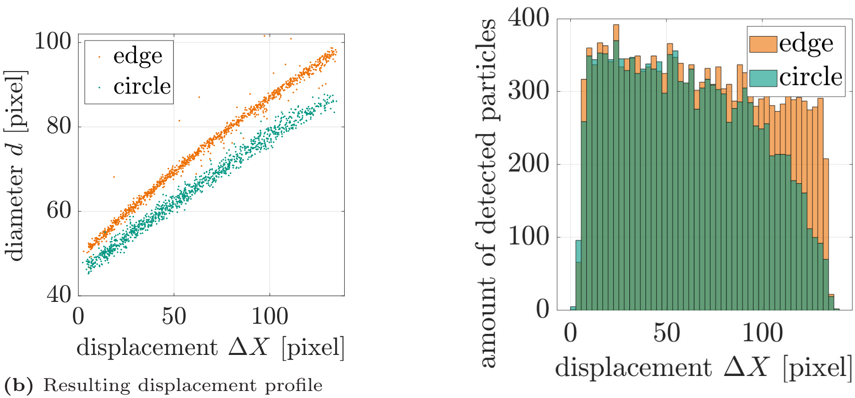

(b) Resulting displacement profile ΔX for image pairs of varying diameters d; only the center part of the FOV is considered to limit the number of displayed pairs

(c) Occurrence distribution of the data shown in Figure 5.6b for displacement bins of 2.8 pixels, SNR reduction for increasing distance from the focal plane

Figure 5.6: Processed displacements ΔX and diameters d of FOV I for both circle 🟩 and edge 🟧 detection approaches (M=7). (Figure adopted from [LFMK21].)

over a larger sensor area, i.e. more pixels. The histograms consequently indicate similar performances of either approach for small and moderate image diameters but also reveals that the circle detection approach requires a higher SNR as compared to the edge detection approach.

The most important uncertainty quantity for DPTV is the accuracy of the particle image diameter determination, denoting the particle location in z direction. One means to approach the diameter determination uncertainty is the evaluation of the estimated particle image diameter change between the double frames.

The undisturbed gap flow above the smooth parts of the disk only propagates in circumferential and radial directions. Thus, in case of FOV I the flow in z direction is expected to be zero and so is the change of the particle image diameter. However, between the two frames, the diameter of a particle image does change due to the uncertainty of the diameter determination, which among others can be influenced by parameters such as the inhomogeneity of the illumination, the image noise, and the signal to noise ratio (SNR) of the particle images. Therefore, the standard deviation of all estimated diameter changes is calculated yielding the following values:

The circle detection approach leads to a particle image diameter determination uncertainty of $2\sigma = 2.39$ pixel. The edge detection method yields an uncertainty of $2\sigma = 0.97$ pixel, lying in the same range as compared to the macroscopic optical set-ups of [26, 27], where values in the range of $2\sigma = 0.79 - 1.03$ pixel were reported for the diameter determination uncertainty. This provides evidence that the comprehensive uncertainty assessments of DPTV that were presented in those publications also apply for this clutch flow experiment. To convert this particle image diameter determination uncertainty into a measure of the achievable resolution in z direction for the present clutch flow experiment, the 2σ particle image diameter uncertainty is multiplied with the slope of the defocusing function, 12.88 µm/pixel.

The resulting localization uncertainty of a particle along the optical axis then yields $2\sigma_z = 12.5$ µm, which corresponds to a relative uncertainty of 2.3% at $h = 0.54$ mm measurement volume depth. Even though this number indicates that the flow within the gap can be well resolved despite the strong velocity gradients it has to be emphasized that σ_z directly affects the derived velocity estimate w in z direction. Translated into a velocity uncertainty the 2σ particle image diameter uncertainty yields a value of 0.15 m/s of each measured velocity, which is around 10% relative to ΩR_m and about 100% relative to the maximum $|\overline{w}|$ value in the groove area. Consequently, more than 100 individual velocity measurements are required to reach an uncertainty of $\sigma_{\overline{w}}$ <1% relative to ΩR_m for the averaged velocity $\overline{w}$ at a certain location.

The issue of peak-locking needs to be suppressed in order to avoid bias errors of the measured velocities and its derivatives, as outlined by [76] and [77]. Figure 5.7 shows the sub-pixel distribution of the particle image diameters d as well as the displacement ΔX in sensor X direction. Both diagrams demonstrate that either diameter determination method does not lead to any peak-locking issues. Note however that peak-locking normally appears if the particle images are small and/or strong intensity gradients are present. In this imaging set-up, the particle image intensity distribution is not particularly steep at the edge (cp. Figure 5.6a), as compared to the set-up with a much lower magnification used by [26].

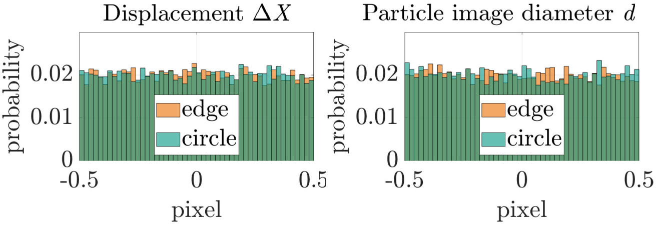

Figure 5.7: Sub-pixel distribution of diameter d and displacement ΔX of the registered particle images for both circle 🟩 and edge 🟧 detection approaches ($M = 7$). (Figure adopted from [LFMK21].)

To conclude this comparative analysis, it can be stated that both evaluation strategies lead to unbiased accurate results with slightly different diameter estimates for the given particle image. This difference leads to accordingly different transfer functions between image diameter and location in the measurement volume. However, these slope differences are compensated by means of the *in situ* calibration procedure with the well-known boundary conditions, such that both approaches yield to quantitative velocity fields in the clutch gap.

The edge detection is found to be more robust in terms of decreasing SNR, leading to a higher particle detection rate for large particle images. Therefore, the remainder of the present work will entirely build upon the edge detection results to analyze the observed flow phenomena in detail. In those cases where the diameter estimate itself is the desired information, however, the Hough-based circle detection algorithm is recommended.

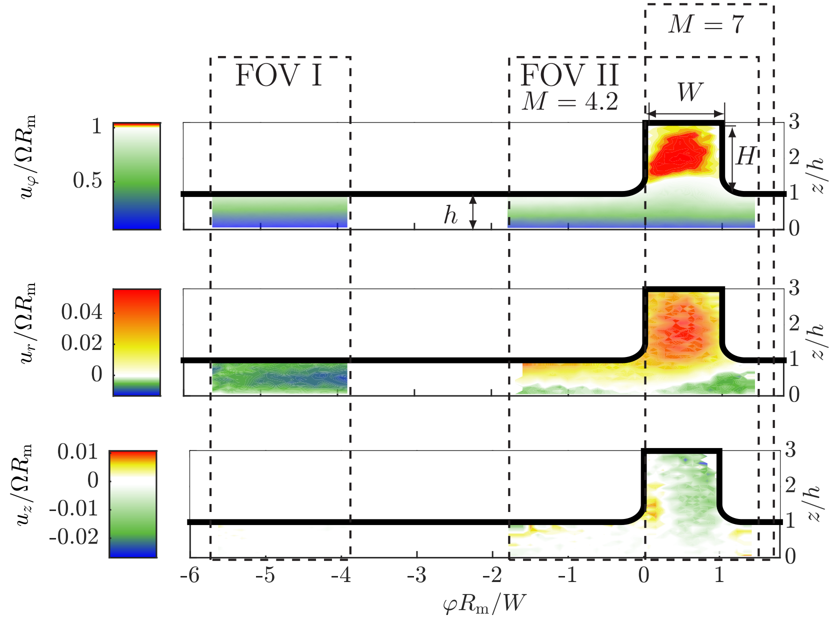

Figure 5.8: Overview of the recorded flow fields: Contours of radially averaged components of normalized circumferential, radial and axial velocity (u_φ, u_r and u_z) are shown for FOV I ($M = 7.0$) on the left and FOV II ($M = 4.2$) on the right. White contour color is chosen for $u_\varphi = \Omega R_\mathrm{m}$, $u_r = 0$ and $u_z = 0$. (Figure adopted from [LFMK21].)

5.3.2 Clutch flow topology

Figure 5.8 provides an overview of the flow situation in the clutch gap; furthermore, it illustrates the distance between the two FOV positions in circumferential direction, where the left part shows FOV I ($M = 7.0$) representing the smooth, ungrooved gap region. The right side of the figure features the velocity information for FOV II ($M = 4.2$ and $M = 7.0$), i.e. the flow in the grooved region of the gap and in particular within the gap. The contours denote the radially averaged values of the normalized circumferential, radial, and axial velocities (u_φ, u_r, and u_z) in the $\varphi - z$

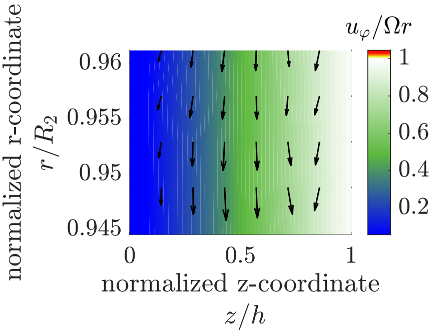

Figure 5.9: Flow field in the $r - z$ plane of the gap in the smooth region of FOV I. A quasi-*Couette-like* flow is superimposed with vectors of additional radial velocity contributions ($M = 7$). (Figure adopted from [LFMK21].)

plane; it is expected to see the main topological flow patterns in this particular plane. Note that the white contour color corresponds to a zero contribution in the case of u_r and u_z, such that changes in the flow direction are indicated more clearly. For the circumferential direction the white contour color denotes the angular disk speed ΩR_m, to better visualize how the flow velocity exceeds the angular speed within the groove.

First, the flow in the ungrooved gap region is analyzed in more detail. In accordance with [54], the flow in that area can be considered *Couette-like*, since the velocity profile is close to being linear, as already discussed earlier and being indicated in Figure 5.9. The radial velocity u_r in this gap part is completely negative – i.e. it is facing towards the clutch center – with a value that is two orders of magnitude lower than the rotational speed. In z direction, the velocity can be considered to be zero. Altogether, the velocity profiles seem to indicate that the groove influence decays quickly, since the measurement location lies only 5 grooves widths downstream of the groove. [62] consider this to be a valuable and important information for the clutch design process. The inward facing radial flow stands in contrast to previous studies with analytical solutions (e.g. [41]), where the maximum of the generally positive (outward facing) radial velocity profile was found to be close to the rotor disk, which was considered to be a result

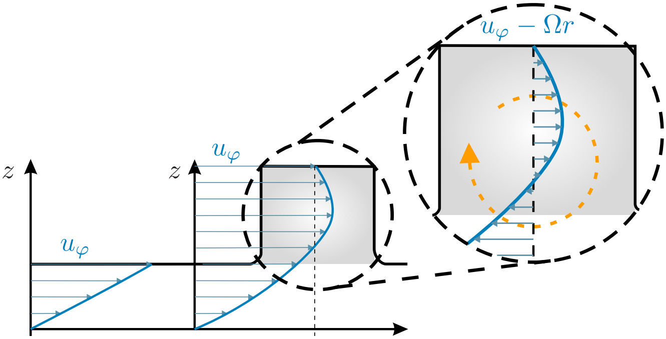

Figure 5.10: Sketch of the expected flow topology for intra-groove velocity in circumferential direction in lab-fixed (i.e. stator-fixed) and rotor-fixed frames of reference. The expected velocity maximum $u_{\max} > \Omega r$ is caused by a cavity vortex in the groove. (Figure adopted from [LFMK21].)

of the influence of the centrifugal forces on the *Poiseuille-like* velocity profile. However, it has to be noted that the latter study used a smooth rotor-stator configuration without grooves. For the present experiment without aeration, the fact of the inward facing radial velocity hints at a significant interaction between the grooves and the smooth parts of the rotor-stator gap. Now, the more complex part of the clutch flow – in the vicinity of the grooves – is characterized in more detail. The Defocusing PTV measurement uncovers formerly unknown velocity information in the groove region allowing for a thorough flow analysis. Figure 5.10 provides a conceptual look at the expected flow topology in the $\varphi - z$ plane inside and above the groove, for both the stator-fixed and rotor-fixed frames of reference. From left to right the sketch illustrates (1) the linear profile, (2) the velocity profile exceeding the rotational speed Ωr within the groove, and (3) the emergence of a cavity roller, as a result of the overspeed. At the rotor disk surface, where the no-slip condition applies, the velocity matches the rotational speed Ωr. In the smooth gap region the velocity yields the rotational speed at $z = h$ and in the grooves at $z = h + H$, respectively. This flow topology concept along with the cavity roller, shown in Figure 5.10, was described earlier in [LK19].

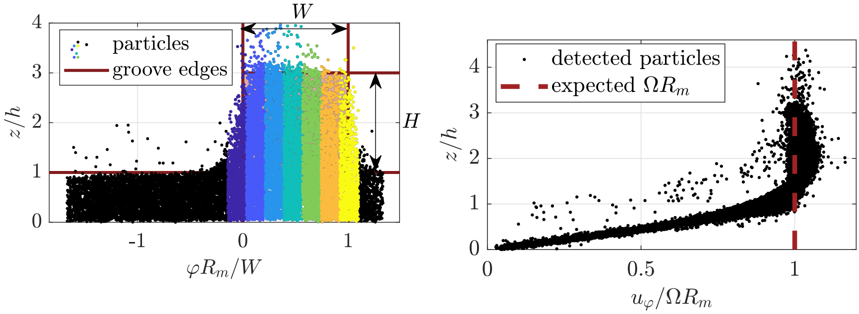

(a) particle locations **(b)** $u_\varphi(z)$ velocity profile

Figure 5.11: (a) Detected data points in a $\varphi - z$-coordinate system. Groove edges and gap height are indicated with vertical and horizontal green lines, respectively; colored particles in the groove region are further converted to separate velocity profiles per color (see Figure 5.12); (b) corresponding velocity information $u_\varphi(z)$ for all detected particle-image pairs for FOV II (M=4.2). (Figure adopted from [LFMK21].)

To fully capture the flow topology in the vicinity of the groove and in particular the interaction between the grooved and the smooth gap region, an experiment with a magnification of $M = 4.2$ was conducted, providing a broader picture of the flow as compared to the $M = 7.0$ experiments.

Two different approaches can be taken to determine the actual groove position from the recorded images. One approach is based on a proper orthogonal decomposition (POD), introduced by [59], that is originally intended as a means to remove background reflections from recordings. Applying the POD to the raw images clearly indicates the position of the groove edges, since the light reflections of the groove edges produce a distinct background pattern. Using this information, $\varphi = 0$ was defined to be situated at the left edge of the groove. Another approach for detecting the groove location is by looking at the spatial distribution of the detected particles. Figure 5.11a shows this spatial particle distribution; it becomes apparent that the grooves of the rotor disk, that is made from a porous material, do not feature sharp edges. In fact, they have a curvature of 0.3 mm that is sharply resolved by the estimated particle locations.

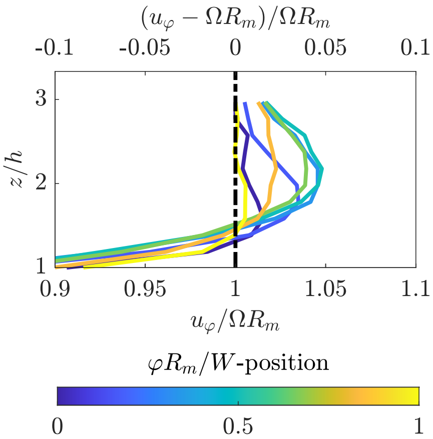

Figure 5.12: Normalized velocity profiles $u_\varphi(z)$ in the rotor-fixed frame of reference for various normalized circumferential locations $\varphi R_\mathrm{m}/W$ inside the groove of the rotor (M=4.2); color coding identical to Figure 5.11. (Figure adopted from [LFMK21].)

In addition to the particle distribution, Figure 5.11b shows a plot of all measured $u_\varphi(z)$ values in the large FOV. Independent of the measurement location, the variation of $u_\varphi(z)$ close to the stator $(z < 0.5)$ stays rather small. Above $z > 0.5$, the velocities start to spread more, and this is due to the modification of the velocity profile within groove cavity. A closer look at the local circumferential velocity in the groove cavity is given in Figure 5.12, where the color indicates the location of the velocity profile , which is provided in 5.11a. Along the gap width, the overspeed, which is the cause for the cavity roller, has the largest value in the groove center, exceeding the rotational speed Ωr by up to 5%. In gap height direction, the velocity maximum is located in the center at $z/h \approx 2$. Towards the edges of the groove cavity the velocity maxima become smaller, and from the left to right in gap width direction, the location of the maxima seem to shift from smaller z/h values to larger values. However, this observation is not quite true for the yellow profile, representing the right edge of the cavity. Furthermore, what becomes evident from the profiles in Figure 5.12 is that in the groove region the flow is decelerated. Thus, the rotational speed of the rotor is reached only above $z/h > 1.2$ and not at $z/h = 1$ like in the case of a *Couette-like* flow.

Figure 5.13 enables a more comprehensive analysis of the cavity roller, showing the vector field of the circumferential and the axial velocity components in the rotor-fixed frame of reference, whereas the radial velocity component is shown as background contours. Furthermore, the Γ_1-criterion as introduced by GRAFTIEAUX [29] has been applied to the velocity field to extract the vortex-center location of the roller. The center of the vortical structure is identified for $\Gamma_1 \approx 1$ at $(\varphi\Omega/W,\ z/h) = (0.33,\ 1.5)$, which is a downstream shift relative to the cavity center at $(\varphi R_m/W,\ z/h) = (0.5,\ 2)$. Both vortex center and Γ_1-isolines are added to Figure 5.13 for clarity.

This finding is in accordance with a previous cavity roller topology investigation by [88], where is was also found that the roller center moves in direction to the gap/cavity interface (in this study located at $z/h = 1$) and towards the trailing edge in circumferential direction, which corresponds to $\varphi R_m = 0$ in this study. Thus, the roller is not limited to the cavity – i.e. above $z/h = 1$ – but it reaches into gap region inducing the above-mentioned deceleration of u_φ in the vicinity of the groove. This is a key information derived from the present quantitative experiments, since current analytical models for drag torque analyses of open wet clutches oversimplify or even neglect this impact as recently summarised by [LNG$^+$20].

Looking at Figure 5.8 again, the interaction between the inward facing flow, with distance to the groove, and outward facing flow, in the groove vicinity, can be analysed in more detail. The magnitude of the radial flow reaches at maximum 5% of the disk speed ΩR_m. The clear separation of the volumetric flow rate Q into a negative radial flux in the groove and a positive flux within the groove does not hold true. Instead, the positive radial flow spreads out from the groove into the gap, reaching further downstream from the forward facing cavity edge.

A quantification of the spatial extent of this gap flow modification is given in Figure 5.13 in terms of a so-called *separatrix* [see e.g. 23, 74, for more

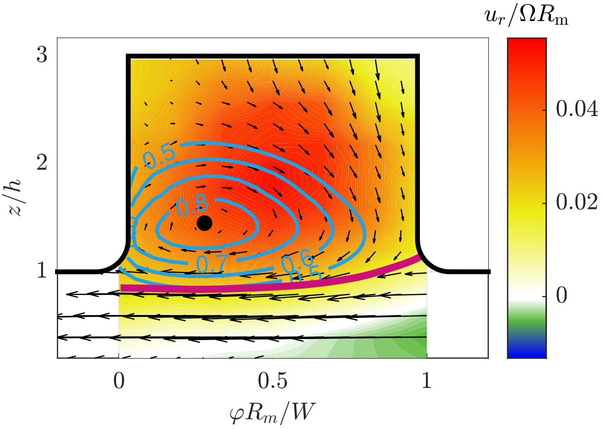

Figure 5.13: Cavity roller in the rotor-fixed frame of reference. Contours of radial velocity u_r are superimposed by Γ_1-isolines (—) and vectors of $u_\varphi - \Omega R_\mathrm{m}$ and u_z. (●) indicates the Γ_1 vortex-center location. A separatrix (—) originated at the backward facing edge is added to indicate the separation of the gap- and cavity-flow domains ($M = 4.2$). (Figure adopted from [LFMK21].)

details on flow topology]. This *separatrix* is drawn from the half-saddle of the backwards facing edge. Obviously, the separatrix does not enclose the fluid inside the cavity but rather drifts into the gap in a flow region of positive radial velocity as an effect of the displacement by the roller.

As mentioned before, the volume flow rate Q was adjusted such that no air entered the gap. Despite the absence of aeration, the appearance flow reversals are a new observation, since the aeration onset is commonly assumed to occur before flow reversals as outlined e.g. by [41]. Thus, it is of utmost importance to thoroughly examine the wall shear foot print of the observed flow patterns on the stator disk in so as to provide an appropriate estimate of the effect on the overall drag torque of the clutch.

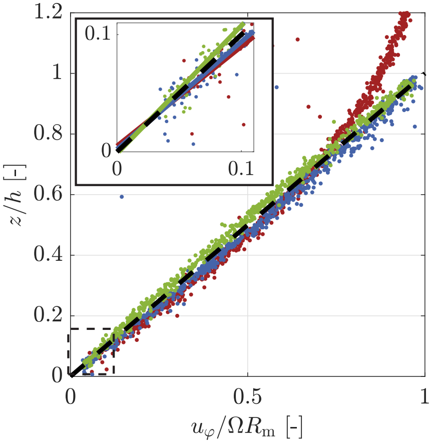

Figure 5.14: Comparison of measured velocity profiles from different circumferential locations with the ideal linear profile (- -). Ungrooved region of FOV I at $\varphi R_\mathrm{m}/W = -4.97 \pm 0.11$ (●); ungrooved region of FOV II immediately next to the groove at $\varphi R_\mathrm{m}/W = 1.47 \pm 0.11$ (●); center part of the groove (FOV II) at $\varphi R_\mathrm{m}/W = 0.67 \pm 0.11$ (●). The insert emphasizes the different slopes of $u_\varphi(h)$ in vicinity above the stator plate and indicates the linear approximation for the WSS estimate ($M = 7$). (Figure adopted from [LFMK21].)

5.3.3 Wall shear stress at stator

In general, the wall shear stress (WSS, τ_w) is an essential quantity for the scaling analysis of near wall flow statistics and turbulence modeling. For technical devices such as the present open wet clutch flow, a detailed knowledge of the WSS is of particular importance, since it has significant influence on the performance of the device in terms of adverse drag torque effects. Since radial fluxes and corresponding velocity gradients $\partial u_r/\partial z$ do not contribute to the drag torque T_s, only the circumferential component $\partial u_\varphi/\partial z$ is considered and the WSS at the stator is accordingly defined as

$$\tau_\mathrm{w} = \mu \frac{\partial u_\varphi}{\partial z}\bigg|_{z=0} \tag{5.2}$$

for the given problem.

Today's torque models for clutch design commonly treat the WSS as a global parameter without local information to account for grooves or distributed surface structures. The direct comparison of velocity profiles at different locations along the perimeter, as shown in Figure 5.14, indicates that this global estimate in fact is an oversimplification of the flow scenario under the presence of grooves, since all curves deviate at least slightly (yet significantly) from the ideal linear profile. In fact, the curvature u_φ changes from $\partial^2 u_\varphi / \partial z^2 > 0$ measured in FOV I midway between the grooves (●: $\varphi R_\mathrm{m}/W = -4.97 \pm 0.11$), to $\partial^2 u_\varphi / \partial z^2 < 0$ in the vicinity of the groove in FOV II (●: measured directly before the groove; measured in the groove center, ●: $\varphi R_\mathrm{m}/W = 0.67 \pm 0.11$). As a consequence, there has to be a variation in the local WSS. In this WSS estimation approach, τ_w is determined by a linear fit of $u_\varphi(z)$ in proximity of the stator $(z/h < 0.1)$. The estimated values are normalized with the ideal WSS $\tau_\mathrm{w,lin} = \Omega r/h$ of an ideal linear Couette profile. Note that $\tau_\mathrm{w,lin}$ increases with increasing radial position r of the measurement.

The local values of the normalized WSS, calculated as

$$\tau_\mathrm{w}^* = \frac{\tau_\mathrm{w}}{\tau_\mathrm{w,lin}} = \frac{\mu h}{\Omega r} \left. \frac{\partial u_\varphi}{\partial z} \right|_{z=0}, \tag{5.3}$$

are shown in a combined diagram in Figure 5.15. For FOV I, values in radial direction are plotted (- · -), and for FOV II across the groove in the circumferential direction (- -). The WSS values are found to be around 4% below the reference value of the linear profile for the smooth gap flow between the grooves (FOV I). Assuming a constant normalized WSS τ_w^* in radial direction, the measured values can be used to calculate the uncertainty of the WSS estimation, yielding $2\sigma = 1.01\%$. However, it has to be emphasized that this uncertainty measure can only provide the order of magnitude of the uncertainty. A reference experiment with a well-known WSS distribution is required for a precise quantification of the uncertainty.

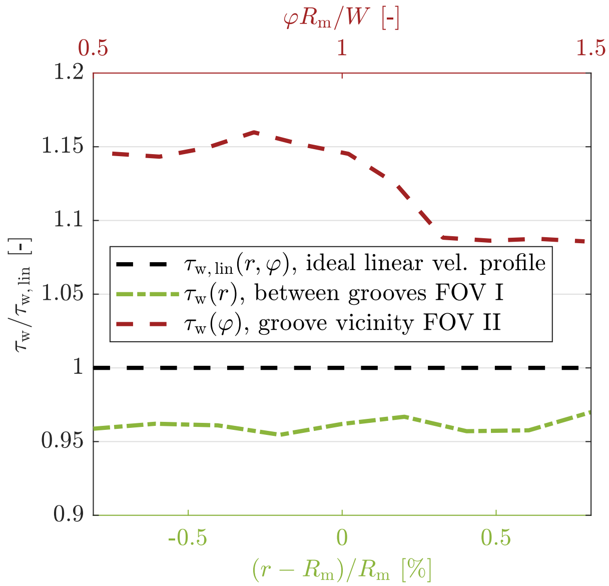

Figure 5.15: The wall shear stress (WSS) increases by up to 15 % in the vicinity of the groove (red line, FOV II), as compared to the WSS of an ideal linear profile. Unlike that, the WSS in the ungrooved gap area, represented by FOV I (green line), lies around 4 % below that of the ideal linear reference ($M = 7$). (Figure adopted from [LFMK21].)

In contrast to FOV I, the circumferential WSS distribution along $\varphi R_\mathrm{m}/W$ reveals a range of WSS values from 9% to 15% above the reference of $\tau_\mathrm{w}^* = 1$. This increase reflects the flow profile modification due to the cavity roller, which extends considerably into the gap and, therefore, slightly displaces the faster fluid towards the stator wall (recall the separatrix of Figure 5.13). Together with the identification of the cavity roller, the determination of the local drag torque is the most important result of this study, since it serves as a first step into a better understanding of the interaction between the grooves and the resulting drag torque.

5.4 Concluding remarks (regarding DPTV)

"Particle imaging for industrial applications is often challenging, in particular if the flow of interest has limited optical access and requires a volumetric analysis. The *in situ* calibrated DPTV approach as used in the present study has proven to be a robust and reliable 3D3C velocimetry technique with only one camera, which allows for a comprehensive analysis of the flow in an open wet clutch.

The diameter of the recorded particle images were determined with an edge detection algorithm and a Hough-transform approach that both were compared in terms of different performance measures. Both strategies revealed no signs of peak-locking and an uncertainty assessment confirmed that the accuracy of a previous, generic lab experiment can be met, yielding a spatial resolution of around 12.5 µm for the in-plane velocities along the optical axis. Such a high resolution turned out to be essential to discover the complex flow structures that are associated with technical applications like in this grooved open wet clutch, which can be described as complex, wall-bounded, sub-millimetre shear flow problem. Since to date no rigorous analysis of the velocity in open wet clutches was done to enlighten the cause-effect relations of aeration, the present Defocusing PTV investigation for the case of a radially grooved clutch-disk geometry uncovers several insightful flow patterns.

The results demonstrate that the velocity of the shear flow in circumferential direction follows a *Couette*-like profile in a sufficiently large distance from the grooves." [LFMK21] The general shape could be estimated with the findings gained in Chapter 3. However, it was found that the linearity is an oversimplification of the flow scenario under the presence of grooves. "The intra-groove analysis uncovers a formerly hidden vortical structure, which is similar to a cavity roller. A further topological analysis of the roller demonstrated that the vortex extends into the gap and consequently displaces the gap flow. Moreover, a characteristic separatrix indicates that considerable amounts of fluid are fed into the gap from the groove. An evaluation of the underlying radial fluxes clearly shows that the majority of the volumetric flow rate passes the clutch through the grooves in positive radial direction. These positive fluxes are also convected into the gap downstream of the groove due to the above-mentioned feeding process. This process is not considered in the drag torque prediction models that are currently being used by the clutch manufacturers. Simultaneously, midway between the grooves, a reverse flow in radial direction is present. This reverse flow is arguably being fed from the outward facing radial flow in the groove at larger radii, as there is no air in the gap. However, the inhomogeneity of radial fluxes across the circumference can be the cause why previous studies found an earlier start of aeration using grooved rotor disks, as compared to smooth rotor disks.

For the design and modelling process of an open wet clutch, the wall shear stress is a decisive quantity. Here, the Defocusing PTV approach reveals that the local wall shear stress changes significantly. Midway between the grooves the curvature of the velocity profile was found to be positive, yielding a wall shear stress that lies approximately 4% lower compared to the reference value of the ideal linear profile. Unlike this, in the vicinity of the groove, the wall shear stress increases to up to 15% above the stress value of an ideal linear velocity profile. Thus, it can be concluded that a detailed knowledge of the interaction between the topology of the cavity roller and the resulting modification of the velocity profile, which is equivalent to a modification of the shear stresses at the opposite disk, is of utmost importance for future, efficiency enhanced groove designs.

Finally, the insights and conclusions of this study clearly underline the value of particle imaging techniques for velocity measurements in industrial applications and might, moreover, contribute towards a deeper understanding of cause-effect relations between the various groove geometries and their respective flow topologies and the resulting drag torque of open wet clutches." [LFMK21]

6 Experimental fluid flow analysis - broader insights and understanding

This chapter extends the current findings of the previous chapters in two ways. First, the favored technique DPTV is tested on its robustness and limitations. Therefore, different magnifications are tested to aim at a broader FOV, which would combine the benefits of the LDV-PS approach and the accuracy of DPTV. Second, a flow analysis with this more beneficial set-up is conducted considering the entire radial spacing of the radial-grooved disk. Additionally, an inclined groove is tested which has the potential of an earlier aeration as outlined in [62]. Here, the velocities are compared in-detail to gain some guidelines for a systematic groove pattern analysis.

Parts of this chapter are based on the conference publication *Defocusing PTV applied to an open wet clutch – from macro to micro* [LFK22]. Where findings were already published, this is clearly marked and indicated as related quotations. Changes within these quotations are only made for a consistent nomenclature.
A missing feature of the explorated measurement techniques so far are a complete overview of the entire region from the inner to the outer disk. Both techniques, as used in Chapter 4 and Chapter 5, need to be traversed to provide a complete velocity field throughout the entire disk. To compensate this disadvantage, the technique DPTV is extended with the

use of various magnifications to test its flexibility. The aim is a broader applicability.

6.1 Accuracy considerations and magnification range of DPTV

To extend the applicability of DPTV for an open wet clutch, different magnifications and lens configurations are tested. The aim is to reach a high spatial accuracy, but also a broad FOV, to capture the region between the inner and outer radius. To address more complex groove patterns, the illumination direction is changed from a light sheet approach – as used in Chapter 5 – to an incident light approach, where the laser illuminates the region from a slight angle compared to the camera viewing direction and no cylindrical lens is used in front of the laser.

6.1.1 Measurement principle

As a recap, the theoretical background for the conducted defocusing experiments is described in Section 2.3.2 with Equation (2.11). "Since each commercial lens has correcting-glass elements for minimizing a vast array of aberrations (e.g. field curvature, spherical aberration, chromatic aberration), the exact intensity distribution – and thus diameter – relies on the lens and various further factors. A direct implementation of Equation (2.11) would lead to unacceptably strong deviations and errors of the position estimation. However, this theoretical consideration might lead to a first estimate and paves the ground for a justified overall approach. A partial derivation of Equation (2.11) in regard to z^* leads to a theoretical defocusing sensitivity δ_s. This dimensionless value appears as theoretical quality factor and can be used for defocusing approaches in general. A formulation of this value can be stated as

$$\delta_\mathrm{s} = \frac{\partial d_\mathrm{i}}{\partial z^*} = \frac{M D_\mathrm{a}}{s_0} \left(= \frac{s^{XY}}{s^Z} \right) . \tag{6.1}$$

To overcome the void between the theoretical consideration and the desire to extract meaningful results, the present study uses the *in situ* calibration approach of [26], where the extracted diameter is locally transformed in physical units on the basis of known boundary conditions in terms of particle displacements. The introduced theoretical defocusing sensitivity δ_s can also be expressed with help of the reproduction scale s^{XY} and the dimensional defocusing sensitivity s^Z.

6.1.2 Experimental set-up

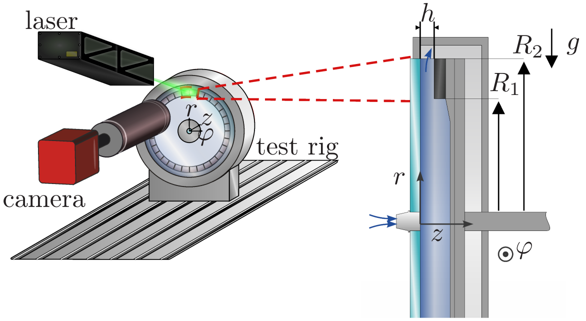

Figure 6.1: Sketch of the experimental set-up (left) and the test rig (right) for the conducted DPTV experiments. (Figure adopted from [LFK22].)

An overview of the experimental set-up is given in Figure 6.1 on the left, while a more detailed view of the clutch geometry is shown on the right. The stator is made from glass with a thickness of 3 mm to allow an optical access for viewing and illuminating the clutch gap. The rotor is made from aluminum, whereas exchangeable polymer clutch disks can be added depending on preference. The disks are manufactured by 3d printing (*Formlabs Form 3L*, layer thickness 50 µm), to allow for complex geometries and fine details of the groove patterns. The clutch geometry is characterized by the following parameters: (1) the inner radius $R_1 = 82.5\,\mathrm{mm}$; (2) the outer radius $R_2 = 93.75\,\mathrm{mm}$; (3) the gap height $h = 400\,\mu\mathrm{m}$ between the clutch surface and the stator; (4) in case of the radially grooved clutch: the groove parameters, which are the width of $W = 1.35$ mm at the groove bottom, the groove height of $H = 1.0$ mm, and the pitch between the grooves of 11.25 ° along the perimeter. To suppress light reflections on the clutch surface, fluorescent melamine resin based seeding particles with a mean diameter of $d_\mathrm{p} = 9.84\,\mu\mathrm{m}$ were used to seed the white mineral oil (CAS No: 8042-47-5, $\rho_0 = 850\,\mathrm{kg/m^3}$, $\nu = 16 \times 10^{-6}\,\mathrm{m^2/s}$), which is supplying the clutch. The seeding particles, emitting a wave length of $\lambda_\mathrm{em} = 584$ nm and were excited at a wave length of $\lambda = 532\,\mathrm{nm}$ with a double-pulsed *Quantel Evergreen* Nd:YAG laser (210 mJ). A band pass filter ($\lambda = 590 \pm 10$ nm) was placed between the camera sensor and the measurement domain, to only capture the fluorescent light of the particles."[LFK22] The volumetric flow rate was adjusted to $Q = 1.6$ l/min and the rotational speed was set to $\Omega = 12.6$ 1/s.

To investigate different optical configurations, the *pco.edge 5.5* sCMOS camera was equipped with a variety of objective lens combinations, including a *Zeiss Makro-Planar* $f_\mathrm{n} = 50\,\mathrm{mm}$ and a *Questar QM 1* telescope, which is further referred to as a long-distance microscope. A detailed analysis of the optical characteristics of the lens combinations is outlined in the following.

6.1.3 Optical characteristics

Depending on the required spatial resolution, the optical set-up can be adapted in terms of varying magnifications. However, changing the optics in turn changes the imaging characteristics. Therefore, certain key parameters are assessed that characterize a defocusing PTV set-up in this section, including the magnification M, the reproduction scale s^{XY}, the FOV size, and the defocusing sensitivity s^{Z}. The latter parameter denotes the relation between the change of the particle-image diameter over the particle z location, i.e. along the optical axis. In principle, this means that a stronger change of the particle-image diameter over a certain z distance means that the particle z location can be determined more accurately.

Altogether four different magnifications were investigated, where the first configuration with the smallest M comprised a *Zeiss Makro-Planar* $f_\mathrm{n} = 50\,\mathrm{mm}$ at the shortest possible working distance together with a 20 mm distance ring to yield the largest possible magnification, which was still capturing the entire radial extent of the clutch gap. An overview of the parameters of all optical configurations is given in Table 6.1, while Figure 6.2 illustrates the FOV extent in comparison to the clutch geometry. The three larger-magnified configurations comprised a *Questar QM 1* long-distance microscope as imaging optics, which was positioned at shortest possible distance of 56 cm. Here, the magnification was adjusted by adding magnifying lenses between the camera and the lens. Note that the FOV size for the *Zeiss* 50 mm configuration was cropped due to optical distortions in the image corners, whereas for the *Questar* configurations the entire sensor was used.

In terms of the accuracy of the particle z-location determination, the defocusing sensitivity s^{Z}, listed in the last column of Table 6.1, is a decisive factor. With increasing magnification s^{Z} decreases, meaning with a certain change of the particle z location, the particle-image diameter increases/decreases by a larger amount. However, it becomes apparent that s^{Z} does not scale linearly with M, since for the first two set-ups (*Zeiss* 50 mm and *Questar* + 2×), the M ratio yields around 6, while s^{Z} ratio yields around 3 (cp. first two rows in Table 6.1). This is due to the fact that with different lens configurations quantities such as the aperture diameter, D_a, change. As can be seen from Equation (2.11), D_a changes the slope of the relation between z and the particle-image diameter. Considering only at the *Questar* configurations, also *Questar* + 6× does not scale linearly with the magnification. The reason for this is the addition of magifiying lenses, which actually changes the largest opening diameter of the light path D_a. The subsequent section addresses the accuracy of the particle z location in relation to the defocusing sensitivity s^Z and classifies the results in the current literature.

Table 6.1: Optical parameters for the different optical configurations, where s^{XY} denotes the reproduction scale and s^Z the defocusing sensitivity.

configuration	M [-]	FOV [mm^2]	s^{XY} [µm/pixel]	s^Z [µm/pixel]
● *Zeiss* 50 mm	0.8	12 × 12	7.57	67.1
● *Questar* + 2×	5.2	3.2 × 2.7	1.25	23.4
● *Questar* + 3×	7.6	2.2 × 1.8	0.86	15.5
● *Questar* + 6×	15	1.1 × 0.9	0.43	9.0

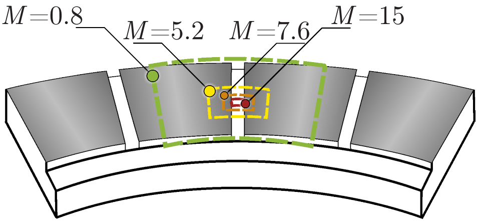

Figure 6.2: Overview of the FOV locations and the corresponding magnifications, M, for all the optical configurations listed in the first column of Table 6.1. (Figure adopted from [LFK22].)

6.2 Results

6.2.1 Particle location uncertainty

As already generally outlined from a theoretical perspective in Section 6.1.1, a stronger rate of change of the particle-image diameter over the particle z location, i.e. along the optical axis, yields an increased resolution. That is, from a theoretical point of view, higher magnifications, which leads to lower s^Z-values as already shown in Table 6.1, might have a lower uncertainty of the particle location.

However, changing the optical configuration also changes the imaging characteristics and, therefore, the appearance of the particle images. Thus, the intensity distribution of the particle images change and with this the signal-to-noise ratio (SNR), among other factors. For the optical configurations presented in this study, the relation between s^Z and the uncertainty of the particle z location determination are assessed in the following to find whether the theoretical consideration is meaningful.

To do so, the assumption that the velocity component u_z is close to zero in the vicinity of the stator is made, which is justified as shown by [LFMK21]. Due to the measurement uncertainty, for a single particle track a non-zero u_z velocity is estimated, such that the standard deviation of the velocity component in z direction can be calculated and transferred into a location uncertainty σ_z (in µm), and an uncertainty of the particle-image diameter σ_{d_i} (in pixel). This standard deviation is a measure of the uncertainty of the particle-image diameter determination, which effectively denotes the uncertainty of the particle z location determination. Table 6.2 gives an overview of the uncertainty values, showing that σ_{d_i} is the lowest with a value of 0.24 pixels, for the *Zeiss* lens. The diameter uncertainty is one order of magnitude larger for the *Questar* configurations, reaching up to almost 11 pixels. Intuitively, given the better defocusing sensitivity at larger magnifications, one might come to the simple suggestion that the particle z location is still better, even if the particle-image diameter uncertainty is larger. However, it becomes apparent that using the *Zeiss* lens is beneficial not only for measuring a larger FOV, but also concerning the particle z-location determination. Furthermore, σ_z is 3 times lower as compared to the *Questar* $M = 5.2$ and $M = 7.6$ configurations. The uncertainty is almost 6 times lower as for the $M = 15$ configuration. In relation to the measurement depth of around 1500 µm, the uncertainty of the particle z location yields only 1.1% for the *Zeiss* lens.

Table 6.2: For the different optical configurations: the uncertainty of the particle-image diameter determination, $2\sigma_{d_\mathrm{i}}$, and the related uncertainty of the particle z location determination, $2\sigma_z$.

configuration	M [-]	$2\sigma_{d_\mathrm{i}}$ [pixel]	$2\sigma_z$ [µm]
● *Zeiss* 50 mm	0.8	0.24	16.4
● *Questar* + 2×	5.2	2.12	49.6
● *Questar* + 3×	7.6	3.12	48.4
● *Questar* + 6×	15	10.98	98.8

The lower performance of the *Questar QM 1* optics has a variety of reasons. One is that the minimum working distance of around 560 mm is relatively large: compared to a microscope objectives with a small working distance of less than 10 mm used in [24], at a similar magnification (13 vs. 15, here), the defocusing sensitivity was $s^{\mathrm{Z}} = 2.05$ µm/pixel, whereas here a value of only 9.0 was achieved. Moreover, the optical characteristics of the *Questar* lead to particle image shapes where the defocused ring is spread out over around 20 pixels combined with a very noisy intensity distribution that barely exceeds the background intensity (see Figure 6.3 for the examples of the intensity distribution). In terms of the SNR this results in a significant detriment relative to the *Zeiss* lens, since for the latter, the defocused ring has a width of around 3 pixels with a very distinct intensity distribution. These conditions are perfect for determining the edge location of the particle images with high accuracy. Comparing the σ_{d_i} values achieved in this experiment using the *Zeiss* lens against what was found by [26], it becomes apparent that the uncertainty here is significantly lower, ~ 0.25 pixel vs. ~ 1 pixel before, even though the optical configuration was similar. However, in the current experiment seeding particles with a diameter of 10 µm were used in a liquid flow, whereas in the previous study an air flow using DEHS particles with a diameter of around 0.35 µm was used. As a result the SNR was lower and so is the accuracy of the diameter estimation, which is also observed when comparing the *Questar* configurations with the *Zeiss* configuration in the present study. " [LFK22]

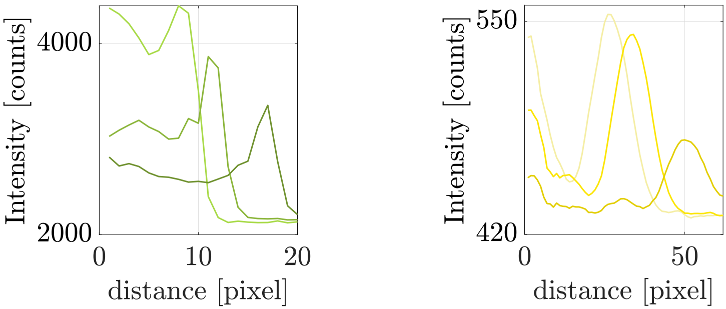

(a) ● $M = 0.8$; **(b)** ● $M = 5.2$;

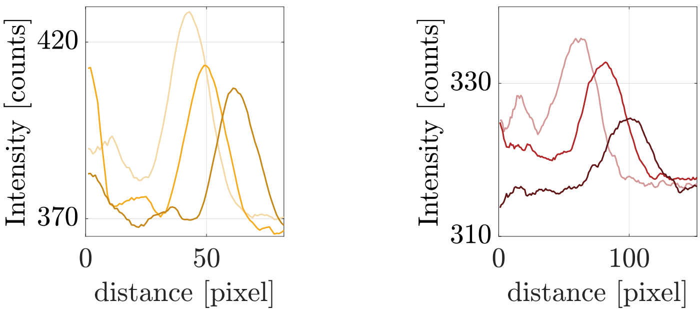

(c) ● $M = 7.6$; **(d)** ● $M = 15$;

Figure 6.3: Radial intensity distribution of three exemplary particle images for each magnification. (Figure adopted from [LFK22].)

6.2.2 Fluid mechanic accuracy considerations

The previous sections focused on the accuracy of each magnification in terms of particle location, while the present section takes the fluid mechanic results into consideration and compares the velocity uncertainties. The smallest magnification enables an investigation of groove-to-groove interactions. “This is important knowledge in terms of an applicability for clutch manufacturers, since this part up-to-now could only be reached with

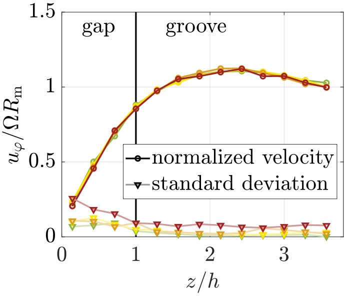

Figure 6.4: Comparison of the circumferential velocity u_φ and the standard deviation σ_{u_φ} at $\varphi R_\mathrm{m}/W = 0.5$ along z for all magnifications (● $M = 0.8$; ● $M = 5.2$; ● $M = 7.6$; ● $M = 15$). (Figure adopted from [LFK22].)

numerical efforts. A considerably wide FOV with an accuracy that is sufficient to depict the most important fluid mechanic phenomena, is beneficial for this flow scenario. The largest magnification displays only a fracture of the groove, thus the particles have a significant lower intensity as shown in Figure 6.3 compared to the particles of the smallest magnification.

Figure 6.4 shows the circumferential velocity in the middle of the groove at $\varphi R_\mathrm{m}/W = 0.5$ for all FOVs. To enable a fair comparison between all set-ups the same amount of particles were used (≈ 500). The z-values were divided in 100 µm divisions. Additionally, the standard deviation σ_{u_φ} is shown for each magnification and z-bin. As already indicated earlier in Section 6.2.1, the trend of a lower uncertainty for the smallest magnification is not only visible for the spatial consideration, but also within the velocity data. The highest magnification yields the largest velocity uncertainty. The reason being similar to the already discussed spatial accuracy. The standard deviation in the gap region is mainly introduced to the higher velocity gradient and a finite fragmentation of the z-binning. For the largest magnification additionally some outliers at low z-coordinates make a noticeable influence. Note, that the error is relatively constant within the groove. Only for the highest magnification a slight increase at the largest z/h-values is visible, which indicates a too low SNR at this part for this specific parameter combination.” [LFK22]

6.3 Groove geometry analysis

An adequate precision in space and velocity has been thoroughly elaborated in the previous considerations. The following section focuses on different radial positions and different groove geometries. The already introduced radial groove is analyzed in more detail, additionally an inclined groove with the same dimensions (groove height $H = 1\,\mathrm{mm}$, groove width $W = 1.35$ mm), but a rotation of 30° along the z-axis in negative direction is considered. The volumetric flow rate was set to $Q = 1.6$ l/min and the gap height to $h = 400\,\mu\mathrm{m}$.

For the following considerations only the data with the lowest magnification of $M = 0.8$ are used, since these experiments combine a large field-of-view with the lowest uncertainty and are consequently best suited for a broader analysis.

First, an overview of the flow field in the radial groove at the mean radius R_m is presented to bring the current findings into context with the results presented in the previous chapters. Second, detailed analyses in the groove region and of the radial flow are outlined.

6.3.1 Radial groove at the mean radius R_m

Figure 6.5 provides an overview of the flow situation in the clutch gap for the mean radius R_m. The shown contours indicate the radially averaged values ($r = R_\mathrm{m} \pm 0.25\,\mathrm{mm}$) of the normalized circumferential, radial and axial velocities in the $\varphi - z$-plane. Recap that the white contours corresponds to zero velocity in the case of u_r and u_z, and to the speed of the disk $\Omega R_\mathbf{m}$ in the case of the circumferential velocity u_φ.

The captured FOV combines both advantages of the previous Chapters 4 and 5. From a fluid mechanic perspective the large FOV comes with the benefit that a continuous analysis over a large circumferential section

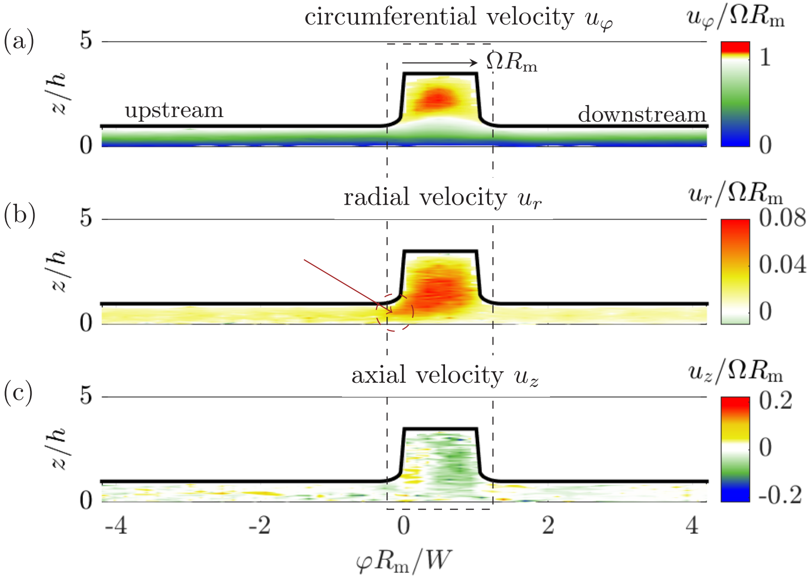

Figure 6.5: Normalized velocity at mean radius $r = R_\mathrm{m}$ for (a) circumferential, (b) radial and (c) axial direction. The black dashed line (- -) indicates the region between $\varphi R/W \in [-0.2; 1.2]$, where the following detailed groove analysis is located. The red arrow ($\longrightarrow$) and the corresponding red dashed circle indicate the upstream extent, where radial flow spills into the gap.

appears possible – in contrast to the FOV in Chapter 5. Generelly, the smooth, ungrooved gap region shows the *Couette-like* behavior as already discussed in the previous chapters in detail. In agreement to earlier findings in Chapter 4 and 5 the circumferential velocity component in combination with the axial component indicate the cavity vortex. The slight differences between the radial velocity in the present experiment and the findings of Chapter 5 can be explained with a higher volumetric flow rate Q and a smaller gap height h. Attention can be drawn to the higher radial velocity in the groove, which clearly extends upstream into the gap; see red arrow and corresponding description in Figure 6.5.

To gain a deeper insight into the cause-effect relationships and the underlying flow mechanisms, such as the vortex-gap-flow interaction, the following section considers the grooved part. The black dashed line in Figure 6.5 indicates the subset within the FOV, which will be evaluated more thoroughly in the following *groove analysis*.

6.3.2 Detailed groove analysis

Figure 6.6 compares the flow through the radial groove at the (a) inner, (b) outer and (c) the mean radius, respectively. Additionally, the mean radius of the inclined grooved is added in Figure 6.6d. Contours of radial velocity u_r are superimposed by vectors of $u_\varphi - \Omega R$ and u_z. To reach a direct comparison level, the color map of u_r and the vector lengths are consistent throughout all sub-figures, but consequently deviate from the previous figure. All velocity components use data of their corresponding radially averaged values ($r = R_1 + 0.5\,\mathrm{mm}$, $r = R_2 - 0.5\,\mathrm{mm}$ and $r = R_\mathrm{m} \pm 0.25\,\mathrm{mm}$) in the $\varphi - z$-plane. To quantify the spatial extent of these geometry modifications a separatrix [23] is added, which originates at the backward facing edge of the groove to depict the separation between the gap flow and the cavity flow in the groove. The dataset as shown in Figure 6.5 is repeated in Figure 6.6c for comparison purposes. With help of the vectors and the subtraction of ΩR_m the cavity vortex becomes visible within the groove. When comparing the rotational movement at the mean radius with the inner and outer radius (Figure 6.6a and 6.6b) it becomes apparent that the vortex is less distinct at the inner radius. This indicates a certain development of the cavity vortex along the radial direction of the groove. Since the feeding mechanism of this vortex is the *Couette-like* flow in circumferential direction, this finding is in agreement with the generally depicted flow situation of the gap flow. Special emphasis can be drawn to the radial flow at the outer radius R_2 in Figure 6.6b, which is about two-times larger at its maximum value in the groove. Note, this might be one possible reason for the separatrix position, as explained later in

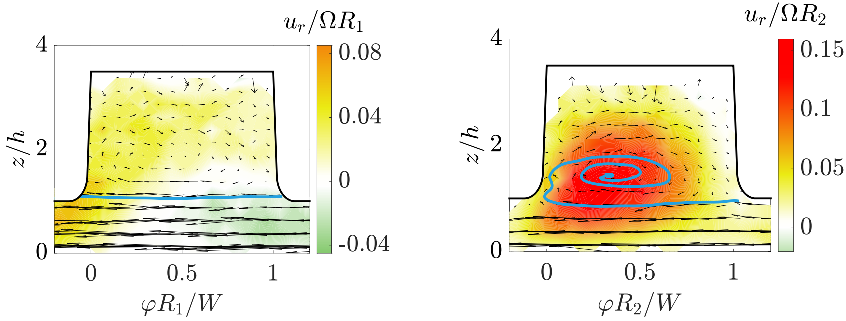

(a) radial groove; inner radius R_1 (b) radial groove; outer radius R_2

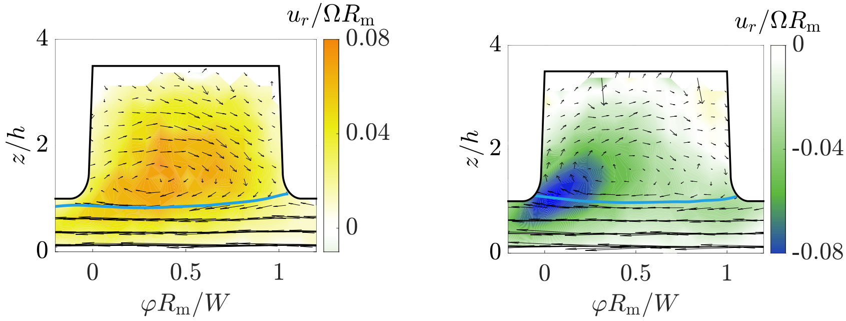

(c) radial groove; mean radius R_m (d) inclined groove; mean radius R_m

Figure 6.6: Radial flow contours and $(u_\varphi - \Omega R_\mathrm{m})$-$u_z$-vectors depicted in the grooved area of $\varphi R/W \in [-0.2; 1.2]$. At the (a) inner, (b) outer (c) mean radius of the radial groove. (d) mean radius of the inclined groove. A separatrix (—) is added to depict the separation of the vortex and the gap flow. At the inner radius (a) there are no significant gap-groove-fluxes. At the mean radius (c) the flux is directing into the gap. At the outer radius (b) the flux is indicating into the groove.

detail. At the inner radius this streamline reaches from the right to the left groove indicating a clear separation of the gap and the groove. At the mean radius the separatrix reaches well into the gap as already discussed in the previous chapter. However, at the outer radius it stays in the groove and is drawn into the vortex center, which coincides with the main radial outflow. This analysis uncovers a complex interaction between groove's region with its cavity roller and the remaining gap flow, since at the mean radius the vortex – and with it fluid from the groove– extends into the gap, while at the outer radius fluid from the gap is drawn into the groove.

Figure 6.6d indicates the flow in an inclined groove. Recap that this geometry option shows an earlier aeration in a drag-torque diagram as outlined in [62] and imitates the direction of the streamline as already discussed in Chapter 3.4 as beneficial for an earlier aeration, since air enters the gap at lower circumferential velocities.

The cavity vortex in the inclined groove is not as distinct as in the radial groove. This is mainly caused by the groove's inclination. The cavity roller is, however, still present at this groove geometry. So, even with an inclination by 30°, this vortex is still the dominant flow topology in the grooved clutch gap. The extension of the vortical structure into the gap is only slightly pronounced indicated by the separatrix, similar to Figure 6.6a. The main difference to the radial groove – a direct comparison at the same radius is Figure 6.6c – is the radial flow, which is facing inwards i.e. in negative r-direction. This presents one main difference in comparison to the radial groove. The highest absolute values of $0.08\,/\Omega R_\mathrm{m}$ can be found at the upstream region of the inclined groove.

To analyze the radial flow as main indicator of the aeration process in a more concise way Figure 6.7 shows the radial velocities along the entire captured FOV for the (a) inner and (b) outer radius of the radial groove and (c) the mean radius of the inclined groove. In contrast to the groove analysis in Figure 6.6 the smooth part of the gap is depicted in addition.

The maximum magnitude of radial velocity u_r at the inner radius R_1 (Figure 6.7a) is equivalent to the u_r-magnitude at the mean radius – Figure 6.5 is a direct comparison –, but the position is clearly different since it appears in the gap at a circumferential value of $-0.5 - 0\ \varphi R_1/W$. In

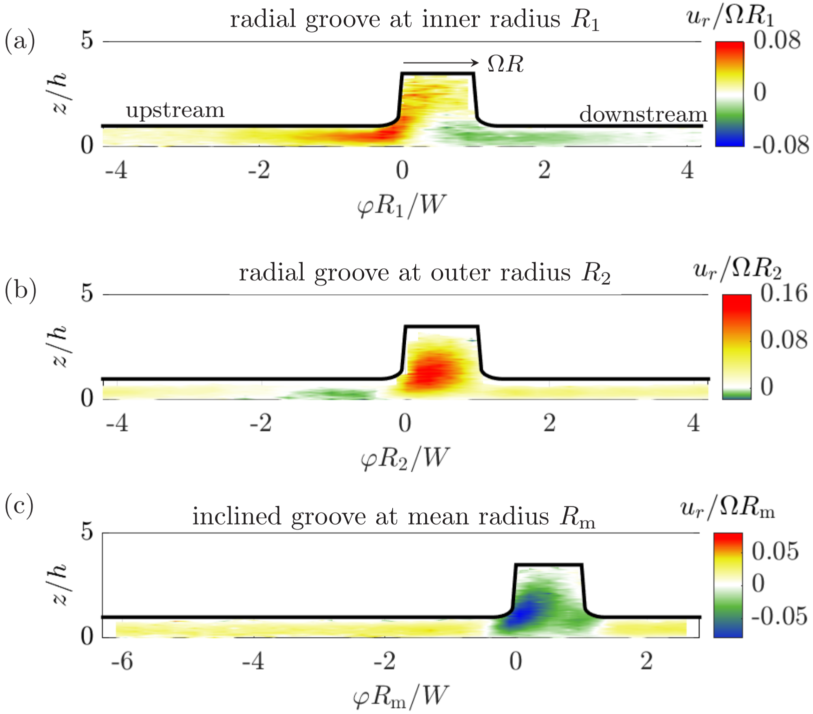

Figure 6.7: Radial flow contours along the entire FOV for (a) the inner radius (b) the outer radius of the radial groove and (c) the mean radius of the inclined groove.

addition, a radial flow with negative sign – which means the fluid is passing towards the clutch inside – is clearly visible in the groove and towards the downstream region of the gap. Recap the already discussed radial flow at the outer diameter (Figure 6.7b), which is about two-times larger at its maximum value in the groove. In addition to this finding, clear regions of negative velocity are visible at the upstream region of the groove up-to a value of $-2\,\varphi R_2/W$. In combination with the velocity distribution at the mean radius and the insights from Chapter 5, where a lower volumetric flow rate leads to a similar reverse flow already at the mean radius, two main conclusions can be drawn. First, the analytical theory that no reverse flow is present before the start of aeration can no longer be justified. Second, the flow in the groove and in the gap clearly interact over a larger distance. As there is no air in the gap, the reverse flow must be compensated from the outward facing radial component in the groove. Figure 6.7c, which shows the radial flow of the inclined groove, stresses this insight further. Negative velocities in the groove must be compensated with the positive fluxes of the flow in the gap. Here, the inward-facing regions are located primarily in the groove, which might be an indicator for the mentioned earlier aeration as described in [62].

The mentioned back flow in the groove is a clear deviation from existing analytical models [70, 78], since such flow situations in terms of an aeration prediction cannot be represented adequately. For the design and modeling process this is beneficial knowledge, since the radial flow strongly links to the physical process of aeration. A complete understanding can, thus, only be reached with a FOV that spans across the entire radius and multiple experiments with increasing angular velocities Ω up-to the two-phase flow. As major take-home from the present experiments the following can be summarized: (i) as quantified by the separatrix a radial-dependent vortex-gap flow interaction exists for the radial groove, which requires further analysis to be conducted along the entire radial dimensions of the clutch disk. (ii) An interaction of the radial outflow with the circumferential flow can be concluded, since, even at the outer radius of the radial groove, significant inward-facing radial velocity components exist, but no air was sucked into the gap. This finding can be explained either with a direct compensation of a flow from the groove to the upstream region or – more likely – with a change of (angular) momentum caused by the geometry of the revolving groove and the dominant radial outflow. Further detailed analyses must be done in order to reach a higher level of comprehension.

6.4 Concluding remarks (regarding the broader analysis)

The present chapter broadens the applicational use of the technique DPTV for the open wet clutch flow, shows first results for a FOV that spans from the inner to the outer radius and provides a first comparison between different groove geometries. “With this experimental open wet clutch flow investigation a large magnification range from macroscopic to microscopic consideration was successfully conducted. It was possible to show, that all four magnification levels were able to depict the fluid flow and the ongoing phenomena in an open wet clutch. Furthermore, defocusing PTV offers its unrestricted suitability for such a flow scenario. Defocused particles with only around 10 counts difference to the background were successfully detected for the largest magnification. It has be shown that, for defocusing PTV, larger magnifications do not necessarily yield a higher accuracy in the particle z location determination, along the optical axis. In fact, using a *Zeiss* macro objective lens at $M = 0.8$ outperformed a *Questar QM1* long-distance microscope ($M = 5 - 15$, depending on the configuration) by at least a factor of 3 in terms of the particle z location uncertainty. As a result of the larger minimum working distance and the inferior imaging quality of the *Questar*, the signal-to-noise ratio of the particle images was significantly lower as in the case of the *Zeiss* lens, leading to a significantly higher uncertainty of the particle-image diameter determination. For future defocusing PTV experiments it seems appropriate to not only consider the defocusing sensitivity as decisive factor, but also take the intensity and the corresponding gradients into account. Analog findings have been made for the fluid mechanic outcomes. All four magnification levels were able to depict the gap flow and the ongoing vortex phenomena in the groove. For a quantitative comparison along the z coordinate the fluid flow in the middle of the groove was chosen. The velocity uncertainty increases with increasing magnification. However, the increase of velocity uncertainty along z for larger magnifications wasn’t as strong as the afore-elaborated

z-location uncertainty increase. This can be traced back to the fact, that the entire measurement depth was considered, instead only the part near the stator.
The demand of a FOV, which spans the region between the inner and the outer radius as well as an intra-groove consideration with a much smaller FOV has been met with this technique. The tested approach of defocusing particle tracking velocimetry is thus considered particularly suitable for such industry-based flow scenarios and appears qualified for further investigations of the flow in an open wet clutch across the board of utilized groove geometries." [LFK22] The comparative fluid mechanic analysis of both different groove geometries and flow locations along a single groove geometry reveals the persistence of the cavity vortex in the groove and the *Couette-like* flow in the smooth part of the gap with a considerably distance to the groove region. The vortical structure, however, influences the flow in the smooth part of the gap, which is quantified by use of the separatrix at each radius level. The analytical theory that no reverse flow is present before the start of aeration was proven to be wrong indicated by the groove region of the inclined groove and also the smooth part of the radial groove at the outer radius. Additionally, a doubled radial velocity – in terms of maximum magnitude – at the outer radius compared to the mean radius is revealed, which might be interesting knowledge for clutch flow simulation efforts to model a realistic image of the pressure boundary condition.

7 Conclusions and outlook

The present thesis focuses on the fluid flow in an open wet clutch. Particularly, an in-depth theoretical consideration with corresponding dimensionless description builds the basis for subsequent experimental efforts, where two novel experimental techniques and their feasible levels are thoroughly elaborated. The conclusions of each approach are summarized at the end of the respective chapters. Therefore, only the major – and partly overarching – conclusions are recapitulated at this point.

To gain some general cause-effect relations a fluid-mechanic based simplification of the Navier–Stokes equations and the vorticity equation is conducted to receive an analytical solution for the circumferential and radial direction in the clutch gap under consideration of gravity without the presence of grooves. This adds valuable information beyond the level of all already existing mainly empirical models. With these precise analytical equations not only an estimate of the gravitational influence is possible – which was neglected in previous studies – but now also an effective tool for advanced aeration studies exists, which includes centrifugal, pressure-driven and gravitational force components as main contributors. For the present study this knowledge was used to explain the occurring negative u_r-velocities at the experimental investigations. The analytical approach finishes with a consideration of grooves within the analytically-solvable environment, such that an equivalent gap height is introduced as modeling concept. It is recommended for future work – might it be analytical, numerical or experimental – to use these novel findings as starting point.

Additionally, the flow parameters under consideration are brought to a dimensionless frame-of-reference and six dimensionless quantities are introduced for this problem, which leads to the simple, yet robust and universal, dependencies of $\zeta_\mathrm{m} = \pi/Re_\mathrm{l}$ and $Q^* = \pi/20$. Beneficial use might gain the $\zeta_\mathrm{m} - Re_\mathrm{l}$-diagram, where the moment coefficient and the Reynolds number are favorable quantities, when compared to the dimensional $T_\mathrm{s} - \Omega$-diagram of drag torque over angular velocity. As a consequence, drag torque analyses are now possible across geometry variations, since the novel description allows for a detailed comparison, such that deviations can be quantified. It is suggested to use the dimensionless description for future open wet clutch research, because it enables the opportunity to directly compare experimental and numerical efforts and provides a validation option, when linked with the analytical solutions.

As the insights of the analytical consideration are limited in terms of different groove patterns two experimental measurement techniques are assessed, both of which are adapted and customized to fit to this flow scenario. Either technique supports different requirements under consideration, such that in combination they evolve their full potential. First, the laser-based technique Laser Doppler Velocimetry profile sensor (LDV-PS) is used to extract a 1D3C velocity profile out of two consecutive 1D2C measurements. The analytically-derived velocity distribution in the smooth part of the gap is successfully validated. Moreover, the groove features a cavity vortex and the maximum of the radial outflow is located within the groove. An estimation of the wall shear stress can be successfully extracted and reveals a higher value in the grooved region compared to the analytical solution. The technique is clearly recommended for industry-relevant flow-diagnostics applications, since no complex post-processing and evaluation is necessary in order to achieve sufficiently-precise velocity information. However, when the elimination of velocity-dependent effects is necessary, newly-developed post-processing steps can compensate the uncertainty for lower velocities. The technique acquires a 360° information of the disk and can thus play an essential role, when investigating more complex groove patterns.

As second experimental technique Defocusing Particle Tracking Velocimetry (DPTV) is used to gain a deeper insight into cause-effect relations within the groove. A quantitative analysis of the vortex and the corresponding separatrix, that divides the gap and the groove, yields valuable insights in this sub-millimeter flow scenario. Furthermore, the wall shear stress was found to increase significantly ($\approx 15\%$) above the stress value of an ideal linear velocity profile. It can be, therefore, concluded that a detailed knowledge of the interaction between the topology of the cavity vortex and the resulting modification of the velocity profile is of utmost importance for future, efficiency enhanced groove designs. From a metrological point of view, the wall shear stress can be extracted precisely, which paves the way to a more accurate – since local – description and has the power to replace the integral drag torque as decisive parameter. This particle-tracking technique enables a robust and flexible use in research and is thus entirely recommended for such sub-millimeter gap flow scenarios. Furthermore, the combined use of both laser-based techniques, LDV-PS and DPTV, covers a large potentially-interesting area of consideration and is suitable for a broader use in open wet clutch research.

DPTV shows particular flexibility during operation, which is why it is chosen for a broader metrological analysis with systematically increasing FOVs. This study reveales the result, that a consideration throughout the entire relevant radius range and over a larger circumferential range is possible with this technique. Additionally, the incident light approach is successfully implemented to address more complex groove patterns. These experiments underline the value of particle imaging techniques for velocity measurements in industrial applications and contribute towards a deeper understanding of cause-effect relations between various groove geometries and their respective flow topologies inside open wet clutches. The subsequently performed experiments focus consequently on a comparative fluid mechanic analysis of a larger radial region and different groove geometries. The cavity vortex is analyzed at three exemplary chosen positions along the radial distance and reveals a varying interaction with the gap flow. The inclined groove shows an inward-facing radial velocity in the groove, which can be connected with the promoted aeration behavior of this geometric configuration. Future work should address such influences in more detail with a study along different angular velocities.

The main fluid mechanic insights gained throughout this entire work are the analytically-derived flow solutions, the dimensionless description and the flow topologies discovered within the radial groove with both experimental techniques. These achievements and insights are summarized and depicted in Figure 7.1 for visual purposes. The analytical description outlines the expected flow field, when no grooves are applied or when the smooth part of a grooved disk is considered. This solution serves as ground base for the experimental work, such as differences to this ideal situation could be quantified, like the slight curvature of the circumferential velocity as discovered by the DPTV experiments. The dimensionless numbers helped to classify the used experimental set-up and pick the right gap height to also consider gravitational impacts. Furthermore, this way of description offers a comparison option for future experiments at different test-rigs and with different geometrical or fluid properties. The experiments conducted throughout the thesis reveal formerly hidden flow structures and their effects on the drag torque and aeration process. The complex interaction between the gap flow and the groove clearly makes a thorough elaboration of the flow in the groove essential, when considering the cause-effect relations of the aeration process.

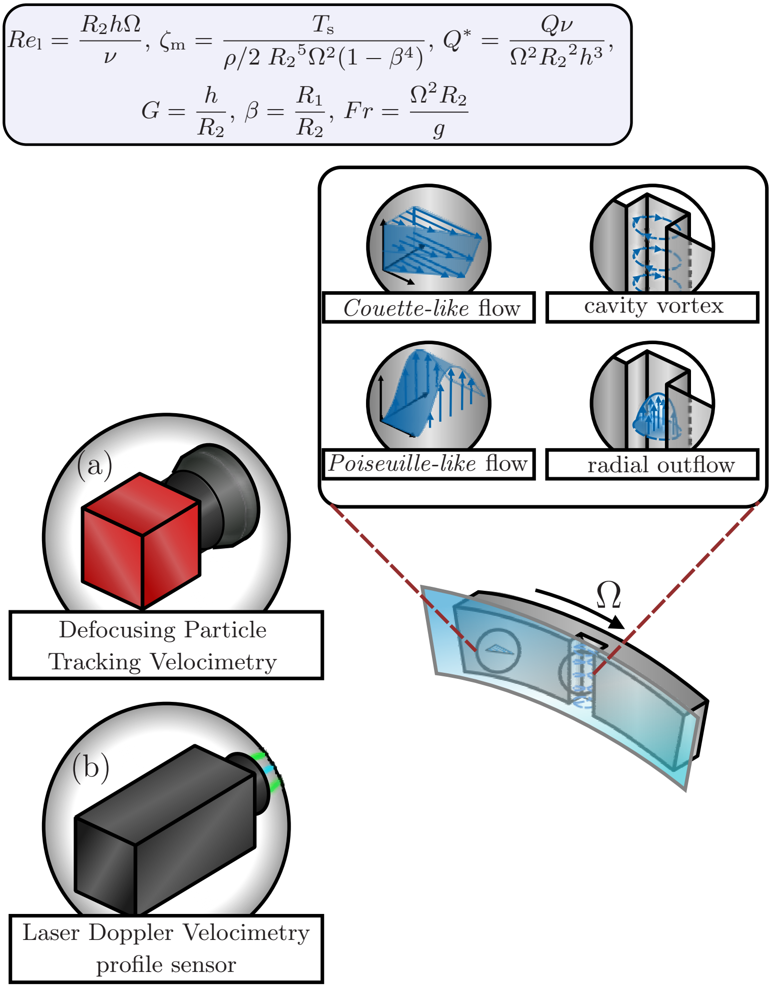
$Re_\mathrm{l} = \frac{R_2 h \Omega}{\nu}$, $\zeta_\mathrm{m} = \frac{T_\mathrm{s}}{\rho/2\ {R_2}^5 \Omega^2 (1-\beta^4)}$, $Q^* = \frac{Q\nu}{\Omega^2 {R_2}^2 h^3}$,
$G = \frac{h}{R_2}$, $\beta = \frac{R_1}{R_2}$, $Fr = \frac{\Omega^2 R_2}{g}$
Couette-like flow
cavity vortex
Poiseuille-like flow
radial outflow
(a)
Defocusing Particle Tracking Velocimetry
(b)
Laser Doppler Velocimetry profile sensor
Ω

Figure 7.1: Overview of the measurement techniques and fluid mechanic insights generated throughout this work. (a) and (b) symbolizes both tested measurement techniques. The radial and circumferential flows show the analytical and experimental findings.

As a perspective remark, the current investigations provide substantial novel knowledge for the fluid flow in an open wet clutch from the theoretical way of description up-to the insights gained throughout both measurement techniques. However, further studies must also take the two-phase flow character into account. When reaching angular velocities, that are fast enough to let air into the gap, additional measurement techniques might be of need. First forward-looking tests are already conducted with the laser-optical technique *interferometric particle imaging* (IPI) in combination with DPTV [LBK22]. Both phases, liquid and gaseous, might furthermore also be tracked simultaneously. An additional outlook from the metrological perspective for DPTV is an advanced particle recognition, which is already tested in [DLP$^+$22]. This might lead to a much higher possible seeding density for this technique, which becomes beneficial for a time-resolved consideration.

On a final note, the combination of LDV-PS and DPTV can be clearly emphasized as industry-relevant flow diagnostic tool to provide additional value to sub-millimeter flow scenarios in general. These techniques might be used throughout many fluid-carrying systems, where the acting principles of energy transfer have similar dimensions than for the exemplary open wet clutch.

Acronyms and symbols

Acronyms

DEHS	Di-Ethyl-Hexyl-Sebacat
DPTV	Defocusing Particle Tracking Velocimetry
FOV	field of view
LDA	Laser Doppler Anemometry
LDV	Laser Doppler Velocimetry
LDV – PS	Laser Doppler Velocimetry Profile Sensor
PIV	Particle Image Velocimetry
POD	proper orthogonal decomposition
PTV	Particle Tracking Velocimetry
SNR	signal-to-noise ratio
WSS	wall shear stress

Latin letter -Upper case

A	area
A_{I}	image area
A_{P}	particle image area

D	image diameter
D_{a}	projected aperture diameter
D_{hy}	hydraulic diameter
Fr	Froude number
G	gap ratio
H	height of the groove
I	intensity
M	magnification
M_1	point for Γ_1 criterion
N_{p}	particle image density
N_{ppp}	number of particles per pixel
N_{S}	source density
P_1	point for Γ_1 criterion
P	perimeter of the cross section
Q	volumetric flow rate
Q^*	dimensionless volumetric flow rate
R	radius
R_1	inner radius
R_2	outer radius
R_{m}	mean radius
Re	Reynolds number
Re_{r}	rotational Reynolds number

Re_g	gap Reynolds number
Re_l	lubrication Reynolds number
S	area
Stk	Stokes number
T_s	drag torque
W	width of the groove
X	sensor spatial coordinate
Y	sensor spacial coordinate
Z	sensor axial coordinate

Latin letter - Lower case

a_g	ratio of grooved and ungrooved area
d	diameter
d_w	wire diameter
d_i	image diameter
d_p	particle diameter
d_f	fringe distance
$d_{\mathrm{f},i}$	fringe distances for $i = 1, 2$
f	frequency
f_i	frequencies for $i = 1, 2$
f_n	focal length
$f_\#$	focal number

$f_\varphi(r,\varphi)$	integration function dependent of r and φ
$f_r(r,\varphi)$	integration function dependent of r and φ
g	gravitational acceleration
g_r	gravitational acceleration in radial direction
g_φ	gravitational acceleration in circumferential direction
h	gap height
h_{eq}	equivalent gap height
l_{c}	characteristic length
n	rotational speed
n_{e}	unit vector
n_{r}	refractive index
p	pressure
q	volume flow rate per unit depth
$q(z)$	ratio of Doppler frequencies
r	radial coordinate
s_{o}	distance between lens and object plane
s_{i}	distance between lens and image plane
s^{XY}	reproduction scale
s^{Z}	slope of defocusing function
t	time
u	velocity
u_{c}	characteristic velocity

u_f	fluid velocity
u_m	velocity vector
u_p	particle velocity
u_φ	circumferential velocity
u_r	radial velocity
u_z	axial velocity
x	spacial coordinate
x_1	spatial coordinate
x_2	spatial coordinate
x_3	spatial coordinate
x^*	spatial coordinate of object plane
y^*	spatial coordinate of object plane
z	axial coordinate
z^*	axial coordinate of object plane

Greek letters - Upper case

Γ	ratio of analytical terms
Γ_1	vortex identification criterion
Ω	angular velocity
Ω_1	angular velocity of inner shaft
Ω_2	angular velocity of outer shaft
Ω_c	critical angular velocity

Greek letters - Lower case

α	ratio of characteristic velocities
α_1	angle
β	radii ratio
β_1	angle
δ_s	theoretical defocusing sensitivity
ζ_m	moment coefficient
θ_M	angle
λ	wave length of light
λ_e	emission wave length
μ	dynamic viscosity
μ_f	dynamic viscosity of fluid
ν	kinematic viscosity
ρ	fluid density
ρ_p	particle density
ρ_o	oil density
σ	uncertainty
τ	shear stress
$\tau_{\varphi z}$	shear stress in φ and z-direction
τ_f	characteristic time of fluid
τ_p	characteristic time of particle

τ_{w}	wall shear stress (WSS)
ϕ	calibration function
φ	circumferential coordinate
ω	vorticity

Mathematical operators

$\partial\,(...)$	partial derivative
$\mathbf{a}$	vector
$\mathcal{O}(...)$	order of magnitude
∇	nabla operator
$(.)^{\sigma}$	uncertainty of the parameter (.)

List of Figures

1.1 Scheme of a multi-disk wet clutch in idling state. 3

2.1 (a) Scheme of an open wet clutch with the most important geometric parameters and the fluid properties. (b) Distribution of the drag torque T_s along the angular velocity Ω with the start of aeration highlighted. 11
2.2 Different typical groove geometries as used in wet clutches. . . 12
2.3 Four flow regimes as proposed by Daily & Nece [19]. Flow regime I (laminar) and III (turbulent) have merged boundary layers, while regime II (laminar) and IV (turbulent) have separated boundary layers. The green region shows the application range for a typical open wet clutch flow. (Diagram adapted from [69].) 13
2.4 Intersection of two laser beams for the classical LDV principle with corresponding beam waists centered and a uniform spacing of the interference fringes. 18
2.5 Intersection of two laser beams for both profile sensor components depicted separately ((a) convergent part and (b) divergent part) with coordinate system, beam waist positions and corresponding fringe distance as a function of z. At the profile sensor set-up these to components overlap. 20
2.6 Scheme of defocusing explained with two particles. The red one is located at the focal plane and imaged sharp. The blue has a distinct distance to the focal plane and is imaged as out-of-focus particle image with a much lower peak intensity as shown in the diagrams. 23

2.7 Overview of the optical geometry with image and object side coordinate system. Adapted from Olsen and Adrian [67]. 24
2.8 Raw images of defocused particles acquired with different focal lengths and lens types (a) 50 mm (b) 105 mm (c) Questar Longdistance microscope 25
2.9 Explanation of the voting algorithm for a circular Hough transform. Each edge point (●) of the circular object to detect (—) vote with a presumed radius. All voting circles (– –) being part of the actual circular object accumulates in the center (●). Only three edge points and one radius are shown for clarity. Figure based on [4]. 29

3.1 Velocity components at $r = R_2$ for the parameters shown in Table 3.2 (a) normalized radial velocity, (b) normalized circumferential velocity. (Figure adapted from [LNG$^+$20].) . . 41
3.2 Drag torque T_s as a function of angular velocity Ω for three different, arbitrary chosen parameter combinations: (Figure adapted from [LNG$^+$20].) 🟦 : $h = 250\ \mu\mathrm{m}, Q = 1\ \mathrm{l/min}, R_2 = 0.09375\ \mathrm{m}$; 🟥 : $h = 350\ \mu\mathrm{m}, Q = 3\ \mathrm{l/min}, R_2 = 0.1172\ \mathrm{m}$; 🟩 : $h = 450\ \mu\mathrm{m}, Q = 5\ \mathrm{l/min}, R_2 = 0.1406\ \mathrm{m}$. 46
3.3 (a) dimensionless quantities moment coefficient ζ_m over Reynolds number Re_l (b) Product $\zeta_\mathrm{m} Re_\mathrm{l}/\pi$ over Q^* of the parameter combination used in Figure 3.2. (Figure adapted from [LNG$^+$20].) 46
3.4 (a) Dimensionless formulation of the point of aeration (maximum of corresponding drag torque curve) in a dimensionless representation for experimental data acquired by [62, 71]. All experimental data lie in the vicinity of the analytically derived theoretical value π/Re_l. (b) Experimental data of the aeration start in comparison to the theoretical value of Q^*_crit. Here the data deviates significantly. (Figure adapted from [LNG$^+$20].) 47
3.5 Geometric dimensions and designation of the disk and groove. (Figure adopted from [LNG$^+$20].) 49

3.6 A systematic comparison of both evaluated models with different parameters. ● : present approach using hydraulic diameter concept; ▼ : approach of Pahlovy *et al.* [70] (Figure adopted from [LNG+20].) 52
3.7 (a) normalized circumferential velocity in a disk-fixed frame of reference (b) normalized radial velocity; The velocity values at $0.7 - 0.9\,h$ are color coded to fit to Figure 3.8. (Figure adopted from [LNK+21].) 54
3.8 Normalized relative velocity $u_\varphi - \Omega r$ and u_r for different heights above the rotating disk. ((a) ● $0.7\,z/h$, (b) ● $0.8\,z/h$ and (c) ● $0.9\,z/h$) The colors correspond to the z/h-levels in Figure 3.7. (d) streamlines originating at $r = R_1$ and the corresponding normalized height. (Figure adopted from [LNK+21].) 55

4.1 Equipment of the used LDV-PS. The first two components provide one velocity component and the spacial information, the third component with parallel fringes provides a second velocity component. (Figure adopted from [LPK22].) 60
4.2 The linearized calibration curve q, used for this LDV profile sensor together with the associated fringe spacings $d_{\mathrm{f},i}$ over x_3 for both spanned fringe patterns. (Figure adopted from [LPK22].) 62
4.3 Scheme of an open clutch with all relevant parameters and the region of interest for the LDV investigation and both conducted experimental set-ups; (a) wire for uncertainty conducts, (b) radial groove for flow measurement. (Figure adopted from [LPK22].) 64
4.4 LDV set-up scheme with both orientations for the LDV-PS ($\alpha_1 = 30°$). The insert explains the conversion from the measured signal to the $\{r, \varphi, z\}$-system. The dominant u_r-component is positive (blue arrow) and the u_z-value tends towards zero (indicated as blue dot). u_φ is pointing orthogonal to the sketch plane. (Figure adopted from [LPK22].) 66

4.5 All measured wire velocities and positions for a constant record length. Higher velocities meet the expected spatial uncertainty, lower velocities reveal more location estimation scatter, thus requiring a broader sample size. (Figure adopted from [LPK22].) 69

4.6 Proportion of counts for the most important quantities received for the wire experiment (diameter $d_{\mathrm{w}} = 10\,\mu\mathrm{m}$, nominal angular velocity $\Omega = \partial\varphi/\partial t = 12.57$ 1/s, radial position on the disk $R_{\mathrm{m}} = 88.1\,\mathrm{mm}$). (a) circumferential velocity u_φ; (b) radial velocity u_r; (c) circumferential angle φ; (d) spatial position z within the gap. (Figure adopted from [LPK22].) 72

4.7 (a) Gap profile of normalized circumferential velocity for various gap Reynolds numbers Re_{g}. Adapted from Lance & Rogers [54]. (b) Sketch of the expected velocity profile (in a disk-fixed coordinate system) in the radial groove. The cavity roller as principle of explanation is added for clarity. The dashed line shows the linear Couette flow as comparison. 74

4.8 Velocity component u_φ and z-position of all detected particles of the flow measurements in the smooth part of the gap flow (•) superimposed to the standard deviation z^σ for different velocities u_φ of the conducted wire experiment (●). The green particles (•) indicate the region, which is considered for the wall shear stress measurements in subsection 4.2.4. (Figure adopted from [LPK22].) 76

4.9 (●) Registered particles across circumference and in the gap region; (a) particle locations for one section $\varphi = 7° - 18.25°$. The particles in the groove are color coded and the dimensions W (groove width) and h (gap height) are added for comparison. The dashed lines show $z/h = 0$ and $z/h = 1$. (b) $u_\varphi(z)$ velocity profile for all registered particles within the groove section and fitted profiles for the four color-coded slices of Figure 4.9a. Additionally added: groove width W, groove height H, gap height h and the dashed line at ΩR_m. (●) Detections originating from the rotor are excluded for further calculations. (Figure adopted from [LPK22].) 77
4.10 Overview of the selected flow field. Contours in a $\varphi - z$ coordinate system of normalized circumferential, radial and axial velocity components, namely u_φ, u_r, u_z. (Figure adopted from [LPK22].) 78
4.11 Angular resolved wall shear stress (WSS) distribution (——). The WSS for the smooth part of the gap is around 3% lower, compared to the WSS of an ideal linear profile (– –). The WSS in the vicinity of the groove (■) is significantly higher, due to the edge and the cavity roller. (Figure adopted from [LPK22].) 81

5.1 Visualisation of Eq. (2.11) for the input parameters of the present particle imaging approach. The red curve shows the image diameter d_i of the mean particle diameter as function of z^*. Physical particle-size deviations are emphasized as a dark gray 3σ margin. This margin vanishes for reasonable distance to the focal plane. (Figure adopted from [LFMK21].) 87
5.2 Picture of the experimental set-up comprised of the clutch model, laser light source and imaging equipment. (Figure adopted from [LFMK21].) 89

5.3 Location of the two fields of view. FOV I is located midway between two grooves. FOV II captures the groove region. In radial direction, the center of the FOVs is aligned with R_m. (Figure adopted from [LFMK21].) 90

5.4 Sketch of the measurement volume between the glass plate (stator) and the radially grooved rotating disk; the relevant geometry parameters are added to the sketch. (Figure adopted from [LFMK21].) 92

5.5 Random double frame raw image, color-coded and inverted for clarity. blue: frame 1; orange: frame 2. The circle pairs directly indicate larger particle displacements with increasing distance from the focal plane. (Figure adopted from [LFMK21].) 94

5.6 Processed displacements ΔX and diameters d of FOV I for both circle 🟩 and edge 🟧 detection approaches (M=7). (Figure adopted from [LFMK21].) 95

5.7 Sub-pixel distribution of diameter d and displacement ΔX of the registered particle images for both circle 🟩 and edge 🟧 detection approaches ($M = 7$). (Figure adopted from [LFMK21].) 97

5.8 Overview of the recorded flow fields: Contours of radially averaged components of normalized circumferential, radial and axial velocity (u_φ, u_r and u_z) are shown for FOV I ($M = 7.0$) on the left and FOV II ($M = 4.2$) on the right. White contour color is chosen for $u_\varphi = \Omega R_\mathrm{m}$, $u_r = 0$ and $u_z = 0$. (Figure adopted from [LFMK21].) 99

5.9 Flow field in the $r - z$ plane of the gap in the smooth region of FOV I. A quasi-*Couette-like* flow is superimposed with vectors of additional radial velocity contributions ($M = 7$). (Figure adopted from [LFMK21].) 100

5.10 Sketch of the expected flow topology for intra-groove velocity in circumferential direction in lab-fixed (i.e. stator-fixed) and rotor-fixed frames of reference. The expected velocity maximum $u_\mathrm{max} > \Omega r$ is caused by a cavity vortex in the groove. (Figure adopted from [LFMK21].) 101

5.11 (a) Detected data points in a $\varphi - z$-coordinate system. Groove edges and gap height are indicated with vertical and horizontal green lines, respectively; colored particles in the groove region are further converted to separate velocity profiles per color (see Figure 5.12); (b) corresponding velocity information $u_\varphi(z)$ for all detected particle-image pairs for FOV II (M=4.2). (Figure adopted from [LFMK21].) . 102
5.12 Normalized velocity profiles $u_\varphi(z)$ in the rotor-fixed frame of reference for various normalized circumferential locations $\varphi R_\mathrm{m}/W$ inside the groove of the rotor (M=4.2); color coding identical to Figure 5.11. (Figure adopted from [LFMK21].) 103
5.13 Cavity roller in the rotor-fixed frame of reference. Contours of radial velocity u_r are superimposed by Γ_1-isolines (—) and vectors of $u_\varphi - \Omega R_\mathrm{m}$ and u_z. (●) indicates the Γ_1 vortex-center location. A separatrix (—) originated at the backward facing edge is added to indicate the separation of the gap- and cavity-flow domains ($M = 4.2$). (Figure adopted from [LFMK21].) 105
5.14 Comparison of measured velocity profiles from different circumferential locations with the ideal linear profile (- -). Ungrooved region of FOV I at $\varphi R_\mathrm{m}/W = -4.97 \pm 0.11$ (●); ungrooved region of FOV II immediately next to the groove at $\varphi R_\mathrm{m}/W = 1.47 \pm 0.11$ (●); center part of the groove (FOV II) at $\varphi R_\mathrm{m}/W = 0.67 \pm 0.11$ (●). The insert emphasizes the different slopes of $u_\varphi(h)$ in vicinity above the stator plate and indicates the linear approximation for the WSS estimate ($M = 7$). (Figure adopted from [LFMK21].) 106
5.15 The wall shear stress (WSS) increases by up to 15 % in the vicinity of the groove (red line, FOV II), as compared to the WSS of an ideal linear profile. Unlike that, the WSS in the ungrooved gap area, represented by FOV I (green line), lies around 4 % below that of the ideal linear reference ($M = 7$). (Figure adopted from [LFMK21].) 108

6.1 Sketch of the experimental set-up (left) and the test rig (right) for the conducted DPTV experiments. (Figure adopted from [LFK22].) 113
6.2 Overview of the FOV locations and the corresponding magnifications, M, for all the optical configurations listed in the first column of Table 6.1. (Figure adopted from [LFK22].) 116
6.3 Radial intensity distribution of three exemplary particle images for each magnification. (Figure adopted from [LFK22].) 120
6.4 Comparison of the circumferential velocity u_φ and the standard deviation σ_{u_φ} at $\varphi R_\mathrm{m}/W = 0.5$ along z for all magnifications (● $M = 0.8$; ● $M = 5.2$; ● $M = 7.6$; ● $M = 15$). (Figure adopted from [LFK22].) 121
6.5 Normalized velocity at mean radius $r = R_\mathrm{m}$ for (a) circumferential, (b) radial and (c) axial direction. The black dashed line (--) indicates the region between $\varphi R/W \in [-0.2; 1.2]$, where the following detailed groove analysis is located. The red arrow ($\longrightarrow$) and the corresponding red dashed circle indicate the upstream extent, where radial flow spills into the gap. 123
6.6 Radial flow contours and $(u_\varphi - \Omega R_\mathrm{m})$-$u_z$-vectors depicted in the grooved area of $\varphi R/W \in [-0.2; 1.2]$. At the (a) inner, (b) outer (c) mean radius of the radial groove. (d) mean radius of the inclined groove. A separatrix (—) is added to depict the separation of the vortex and the gap flow. At the inner radius (a) there are no significant gap-groove-fluxes. At the mean radius (c) the flux is directing into the gap. At the outer radius (b) the flux is indicating into the groove. 125
6.7 Radial flow contours along the entire FOV for (a) the inner radius (b) the outer radius of the radial groove and (c) the mean radius of the inclined groove. 127

7.1 Overview of the measurement techniques and fluid mechanic insights generated throughout this work. (a) and (b) symbolizes both tested measurement techniques. The radial and circumferential flows show the analytical and experimental findings. 135

List of Tables

3.1 Characteristic velocities and length scales for the order-of-magnitude analysis conducted in Equation (3.1-3.3). . 32
3.2 Quantities of corresponding physical values for all relevant open clutch parameters. (Table adopted from [LNK$^+$21].) . . . 41

4.1 Parameters of the LDV–PS used for this study. 62
4.2 Orientation of the LDV-PS system against the z-axis to measure and/or determine the velocity components u_φ, u_r and u_z at the desired perimeter. 67
4.3 All measured wire velocities with corresponding standard deviations of location and velocity. 70

6.1 Optical parameters for the different optical configurations, where s^{XY} denotes the reproduction scale and s^Z the defocusing sensitivity. 116
6.2 For the different optical configurations: the uncertainty of the particle-image diameter determination, $2\sigma_{d_\mathrm{i}}$, and the related uncertainty of the particle z location determination, $2\sigma_z$.118

List of Publications

Journal articles

[DLP^{+}22] Maximilian Dreisbach, Robin Leister, Matthias Probst, Pascal Friederich, Alexander Stroh, and Jochen Kriegseis. Particle detection by means of neural networks and synthetic training data refinement in defocusing particle tracking velocimetry. *Measurement Science and Technology*, 33(12):124001, 2022. URL: https://doi.org/10.1088/1361-6501/ac8a09.

[LBK22] Robin Leister, Andreas Brümmer, and Jochen Kriegseis. Laser-Optical Shear-Flow Analysis across the Annular Gap of a Simplified Displacement Compressor Model. *IOP Conference Series: Materials Science and Engineering - International Conference on Screw Machines (ICSM 2022)*, 1267(1):012003, 2022. URL: https://dx.doi.org/10.1088/1757-899X/1267/1/012003, `doi:10.1088/1757-899X/1267/1/012003`.

[LFMK21] Robin Leister, Thomas Fuchs, Philipp Mattern, and Jochen Kriegseis. Flow-structure identification in a radially grooved open wet clutch by means of defocusing particle tracking velocimetry. *Experiments in Fluids*, 62(2): Article: 29, 2021. URL: https://doi.org/10.1007/s00348-020-03116-0.

[LNG^{+}20] Robin Leister, Amir F. Najafi, Davide Gatti, Jochen Kriegseis, and Bettina Frohnapfel. Non-dimensional characteristics of open wet clutches for advanced drag torque and aeration predictions. *Tribology International*, 152:106442, 2020. URL: https://doi.org/10.1016/j.triboint.2020.106442.

[LNK$^+$21] Robin Leister, Amir F. Najafi, Jochen Kriegseis, Bettina Frohnapfel, and Davide Gatti. Analytical modeling and dimensionless characteristics of open wet clutches in consideration of gravity. *Forschung im Ingenieurwesen*, 85(4):849–857, 2021. URL: https://doi.org/10.1007/s10010-021-00545-z.

[LPK22] Robin Leister, Saskia Pasch, and Jochen Kriegseis. On the Applicability of LDV Profile-Sensors for periodic Open Wet Clutch Flow Scenarios. *Experiments in Fluids*, 63(8): Article: 134, 2022. URL: https://doi.org/10.1007/s00348-022-03487-6.

Conference contributions

[DLP$^+$21] Maximilian Dreisbach, Robin Leister, Matthias Probst, Pascal Friederich, Alexander Stroh, and Jochen Kriegseis. Particle detection by means of machine learning in defocusing PTV. In *14th International Symposium on Particle Image Velocimetry – ISPIV*, 1-4 August, 2021, [online] URL: https://doi.org/10.18409/ispiv.v1i1.182, 2021.

[LFK22] Robin Leister, Thomas Fuchs, and Jochen Kriegseis. Defocusing PTV applied to an open wet clutch -– from macro to micro. In *20th International Symposium on Application of Laser and Imaging Techniques to Fluid Mechnaics–Lisbon Laser 2022*, 11-14 July, 2022, Lisbon, Portugal, 2022.

[LK19] Robin Leister and Jochen Kriegseis. 3D-LIF experiments in an open wet clutch by means of defocusing PTV. In *13th International Symposium on Particle Image Velocimetry – ISPIV*, 22-24 July, 2019, Munich, Germany, 2019.

[LK21] Robin Leister and Jochen Kriegseis. DPTV-based analysis of the flow-structure/wall-shear interplay in open wet clutches. In *14th International Symposium on Particle Image Velocimetry – ISPIV*, 1-4 August, 2021, [online] URL: https://doi.org/10.18409/ispiv.v1i1.178, 2021.

[LKF^{+}21] Robin Leister, Jochen Kriegseis, Bettina Frohnapfel, Davide Gatti, and Amir F. Najafi. Analytical modeling and dimensionless characteristics of open wet clutches in consideration of gravity (presentation). In *VDI-Fachtagung Kupplungen und Kupplungssysteme in Antrieben (2021)*, 24.-25. November 2021, Ettlingen, Germany URL: https://doi.org/10.51202/9783181023822-129, 2021.

[LNKF19] Robin Leister, Amir F. Najafi, Jochen Kriegseis, and Bettina Frohnapfel. Modelling concepts of open wet clutch flows - a theoretical approach (poster). 46th Leeds-Lyon Symposium on Tribology (2019) 2.–4. September 2019, Lyon, France, 2019.

[LPF^{+}21] Robin Leister, Saskia Pasch, Bettina Frohnapfel, Jochen Kriegseis, Philipp Mattern, and Thomas Fuchs. Hochaufgelöste, optische Geschwindigkeitsmessungen in einer radialgenuteten, offenen, nasslaufenden Lamellenkupplung (in German). In *VDI-Fachtagung Kupplungen und Kupplungssysteme in Antrieben (2021)*, 24.-25. November 2021, Ettlingen, Germany URL: https://doi.org/10.51202/9783181023822-313, 2021.

Bibliography

[1] R. J. Adrian. Scattering particle characteristics and their effect on pulsed laser measurements of fluid flow: speckle velocimetry vs particle image velocimetry. *Appl. Opt.*, 23(11):1690–1691, 1984. doi: 10.1364/AO.23.001690. URL `http://opg.optica.org/ao/abstract.cfm?URI=ao-23-11-1690`.

[2] R. J. Adrian and J. Westerweel. *Particle Image Velocimetry*. Cambridge University Press, Cambridge, United Kingdom, 2011. URL `https://www.cambridge.org/9780521440080`.

[3] H.-E. Albrecht, M. Borys, N. Damaschke, and C. Tropea. *Laser Doppler and Phase Doppler Measurement Techniques*. Springer Berlin, Heidelberg, Germany, 2003. URL `https://doi.org/10.1007/978-3-662-05165-8`.

[4] T. Atherton and D. Kerbyson. Size invariant circle detection. *Image and Vision Computing*, 17(11):795–803, 1999. ISSN 0262-8856. URL `https://www.sciencedirect.com/science/article/pii/S0262885698001607`.

[5] F. Bandini, B. Lüthi, S. Peña-Haro, C. Borst, J. Liu, S. Karagkiolidou, X. Hu, G. G. Lemaire, P. L. Bjerg, and P. Bauer-Gottwein. A drone-borne method to jointly estimate discharge and manning's roughness of natural streams. *Water Resources Research*, 57(2), 2021. URL `https://doi.org/10.1029/2020wr028266`.

[6] R. Barnkob and M. Rossi. General defocusing particle tracking: fundamentals and uncertainty assessment. *Experiments in Fluids*, 61(4), 2020. URL `https://doi.org/10.1007/s00348-020-2937-5`.

[7] R. Barnkob, C. J. Kähler, and M. Rossi. General defocusing particle tracking. *Lab on a Chip*, 15(17):3556–3560, 2015. URL `https://doi.org/10.1039/C5LC00562K`.

[8] A. B. Basset. *A Treatise on Hydrodynamics vol II.* Cambridge, Deighton, Bell and Co, George Bell and sons, Cambridge, United Kingdom, 1888.

[9] C. Bayer, K. Shirai, L. Büttner, and J. Czarske. Measurement of acceleration and multiple velocity components using a laser doppler velocity profile sensor. *Measurement Science and Technology*, 19(5):055401, 2008. URL `https://doi.org/10.1088/0957-0233/19/5/055401`.

[10] S. Burgmann, M. Dues, B. Barwari, J. Steinbock, L. Büttner, J. Czarske, and U. Janoske. Flow measurements in the wake of an adhering and oscillating droplet using laser-doppler velocity profile sensor. *Experiments in Fluids*, 62(47), 2021. URL `https://doi.org/10.1007/s00348-021-03148-0`.

[11] L. Büttner and J. Czarske. Determination of the axial velocity component by a laser-doppler velocity profile sensor. *J. Opt. Soc. Am. A*, 23(2):444–454, 2006. doi: 10.1364/JOSAA.23.000444. URL `http://josaa.osa.org/abstract.cfm?URI=josaa-23-2-444`.

[12] F. Bürkle, F. Moyon, L. Feierabend, J. Wartmann, A. Heinzel, J. Czarske, and L. Büttner. Investigation and equalisation of the flow distribution in a fuel cell stack. *Journal of Power Sources*, 448:227546, 2020. ISSN 0378-7753. URL `https://doi.org/10.1016/j.jpowsour.2019.227546`.

[13] L. Büttner and J. Czarske. Spatial resolving laser doppler velocity profile sensor using slightly tilted fringe systems and phase evaluation.

Measurement Science and Technology, 14(12):2111–2120, 2003. URL `https://doi.org/10.1088/0957-0233/14/12/010`.

[14] C. Cierpka and C. J. Kähler. Particle imaging techniques for volumetric three-component (3d3c) velocity measurements in microfluidics. *Journal of Visualization*, 15(1):1–31, 2012. URL `https://doi.org/10.1007/s12650-011-0107-9`.

[15] C. Cierpka, R. Segura, R. Hain, and C. J. Kähler. A simple single camera 3c3d velocity measurement technique without errors due to depth of correlation and spatial averaging for microfluidics. *Measurement Science and Technology*, 21(4):045401, 2010. URL `https://doi.org/10.1088/0957-0233/21/4/045401`.

[16] H. Cui, S. Yao, Q. Yan, S. Feng, and Q. Liu. Mathematical model and experiment validation of fluid torque by shear stress under influence of fluid temperature in hydro-viscous clutch. *Chinese Journal of Mechanical Engineering*, 27(1):32–40, 2014. URL `https://doi.org/10.3901/cjme.2014.01.032`.

[17] J. Czarske. Laser doppler velocity profile sensor using a chromatic coding. *Measurement Science and Technology*, 12(1):52–57, 2001. URL `https://doi.org/10.1088/0957-0233/12/1/306`.

[18] J. Czarske, L. Büttner, T. Razik, and H. Müller. Boundary layer velocity measurements by a laser doppler profile sensor with micrometre spatial resolution. *Measurement Science and Technology*, 13(12):1979, 2002. URL `http://stacks.iop.org/0957-0233/13/i=12/a=324`.

[19] J. W. Daily and R. E. Nece. Chamber dimension effects on induced flow and frictional resistance of enclosed rotating disks. *Journal of Basic Engineering*, 82(1):217–230, 1960. URL `https://doi.org/10.1115/1.3662532`.

[20] R. O. Duda and P. E. Hart. Use of the hough transformation to detect lines and curves in pictures. *Commun. ACM*, 15(1):11–15, 1972. ISSN 0001-0782. URL `https://doi.org/10.1145/361237.361242`.

[21] G. Elsinga, F. Scarano, B. Wieneke, and B. van Oudheusden. Double-frame 3D-PTV using a tomographic predictor. *Experiments in Fluids*, 41(6):933–947, 2006. URL `https://doi.org/10.1007/s00348-006-0212-z`.

[22] R. L. Fish. Using the sae #2 machine to evaluate wet clutch drag losses. *SAE Transactions*, 100:1041–1054, 1991. ISSN 0096736X, 25771531. URL `http://www.jstor.org/stable/44632092`.

[23] J. F. Foss. Surface selections and topological constraint evaluations for flow field analyses. *Experiments in Fluids*, 37:883–898, 2004. URL `https://doi.org/10.1007/s00348-004-0877-0`.

[24] T. Fuchs and C. J. Kähler. Single axis volumetric µPTV for wall shear stress estimation. In C. J. Kähler, R. Hain, S. Scharnowski, and T. Fuchs, editors, *Proceedings of the 13th International Symposium on Particle Image Velocimetry*, 2019. URL `https://athene-forschung.unibw.de/doc/129386/129386.pdf`.

[25] T. Fuchs, R. Hain, and C. J. Kähler. Three-dimensional location of micrometer-sized particles in macroscopic domains using astigmatic aberrations. *Optics Letters*, 39(5):1298–1301, 2014. URL `https://doi.org/10.1364/OL.39.001298`.

[26] T. Fuchs, R. Hain, and C. J. Kähler. In situ calibrated defocusing ptv for wall-bounded measurement volumes. *Measurement Science and Technology*, 27(8):084005, 2016. URL `http://stacks.iop.org/0957-0233/27/i=8/a=084005`.

[27] T. Fuchs, R. Hain, and C. J. Kähler. Uncertainty quantification of three-dimensional velocimetry techniques for small measurement depths. *Experiments in Fluids*, 57(5):73, 2016. URL `https://doi.org/10.1007/s00348-016-2161-5`.

[28] D. Gabor. A new microscopic principle. *Nature*, 161(4098):777–778, 1948. URL `https://doi.org/10.1038/161777a0`.

[29] L. Graftieaux, M. Michard, and N. Grosjean. Combining PIV, POD and vortex identification algorithms for the study of unsteady turbulent swirling flows. *Measurement Science and Technology*, 12:1422–1429, 2001. URL `https://doi.org/10.1088/0957-0233/12/9/307`.

[30] S. I. Green, editor. *Fluid vortices*. Fluid mechanics and its applications ; 30. Kluwer Academic Publishers, Alphen aan den Rijn, Netherlands, Dordrecht [u.a.], 1995. ISBN 0792333764; 9780792333760. URL `https://doi.org/10.1007/978-94-011-0249-0`.

[31] D. Gropper, L. Wang, and T. J. Harvey. Hydrodynamic lubrication of textured surfaces: A review of modeling techniques and key findings. *Tribology International*, 94:509 – 529, 2016. URL `https://doi.org/10.1016/j.triboint.2015.10.009`.

[32] L. Gräf and L. Kleiser. Flow-field analysis of anti-kidney vortex film cooling. *Journal of Thermal Science*, 21(1):66–76, 2012. URL `https://doi.org/10.1007/s11630-012-0520-y`.

[33] D. Grötsch, R. Niedenthal, K. Völkel, H. Pflaum, and K. Stahl. Effiziente CFD-Simulationen zur Berechnung des Schleppmoments nasslaufender Lamellenkupplungen im Abgleich mit Prüfstandmessungen. *Forschung im Ingenieurwesen*, 83:227–237, 2019. ISSN 1434-0860. URL `https://doi.org/10.1007/s10010-019-00302-3`.

[34] D. Grötsch, R. Niedenthal, K. Völkel, H. Pflaum, and K. Stahl. Volume of fluid vs. cavitation CFD-models to calculate drag torque in multi-plate clutches. In *SAE Technical Paper Series*. SAE International, apr 2020. URL `https://doi.org/10.4271/2020-01-0495`.

[35] H. Hashimoto, S. Wada, and Y. Murayama. The performance of a turbulent-lubricated sliding bearing subject to centrifugal effects. In *Trans. Jpn, Society Mechanical Engineering*, volume 49, pages 1753–1761, 1984.

[36] K. D. Hinsch. Three-dimensional particle velocimetry. *Measurement Science and Technology*, 6(6):742–753, 1995. URL `https://doi.org/10.1088/0957-0233/6/6/012`.

[37] N. Holzer, D. Frey, and B. Matthes. Schleppmomente an nasslaufenden lamellenbremsen. *VDI Berichte*, 1323:469–490, 1997.

[38] J. Hong, M. Toloui, L. P. Chamorro, M. Guala, K. Howard, S. Riley, J. Tucker, and F. Sotiropoulos. Natural snowfall reveals large-scale flow structures in the wake of a 2.5-MW wind turbine. *Nature Communications*, 5(1), 2014. URL `https://doi.org/10.1038/ncomms5216`.

[39] J. Hou, F. Kaiser, A. Sciacchitano, and D. E. Rival. A novel single-camera approach to large-scale, three-dimensional particle tracking based on glare-point spacing. *Experiments in Fluids*, 62(5), 2021. URL `https://doi.org/10.1007/s00348-021-03178-8`.

[40] P. V. C. Hough. Machine Analysis of Bubble Chamber Pictures. *Proceedings, 2^{nd} International Conference on High-Energy Accelerators and Instrumentation*, C590914:554–558, 1959. URL `https://s3.cern.ch/inspire-prod-files-5/53d80b0393096ba4afe34f5b65152090`.

[41] J. Huang, J. Wei, and M. Qiu. Laminar flow in the gap between two rotating parallel frictional plates in hydro-viscous drive. *Chinese Journal of Mechanical Engineering*, 25(1):144–152, 2012. URL `https://doi.org/10.3901/CJME.2012.01.144`.

[42] S. Iqbal, F. Al-Bender, B. Pluymers, and W. Desmet. Experimental characterization of drag torque in open multi-disks wet clutches. *SAE International Journal of Fuels and Lubricants*, 6(3):894–906, 2013. ISSN 19463952, 19463960. URL `https://doi.org/10.4271/2013-01-9073`.

[43] S. Iqbal, F. Al-Bender, B. Pluymers, and W. Desmet. Mathematical model and experimental evaluation of drag torque in disengaged wet clutches. *ISRN Tribology*, 2013:16, 2013. URL `https://doi.org/10.5402/2013/206539`.

[44] S. Iqbal, F. Al-Bender, B. Pluymers, and W. Desmet. Model for predicting drag torque in open multi-disks wet clutches. *Journal of Fluids Engineering*, 136(2):021103, 2013. URL `https://doi.org/10.1115/1.4025650`.

[45] H. Kao and A. Verkman. Tracking of single fluorescent particles in three dimensions: use of cylindrical optics to encode particle position. *Biophysical Journal*, 67(3):1291–1300, 1994. URL `https://doi.org/10.1016/s0006-3495(94)80601-0`.

[46] Y. Kato, T. Murasugi, H. Hirano, and T. Shibayama. Fuel economy improvements through tribological analysis of the wet clutches and brakes of an automatic transmission. In *Society of Automotive Engineers of Japan*, volume 16, pages 57–60, 1993.

[47] H. Kitabayashi, C. Y. Li, and H. Hiraki. Analysis of the various factors affecting drag torque in multiple-plate wet clutches. In *SAE Technical Paper Series*. SAE International, 2003. URL `https://doi.org/10.4271/2003-01-1973`.

[48] N. H. Kling, J. Kriegseis, L. Opfer, and P. Rogler. Dual-plane stereo-astigmatism: a novel method to determine the full velocity gradient tensor in planar domain. *Measurement Science and Technology*, 31(8):085202, 2020. URL `https://doi.org/10.1088/1361-6501/ab7283`.

[49] F. Kreith and H. Viviand. Laminar Source Flow Between Two Parallel Coaxial Disks Rotating at Different Speeds. *Journal of Applied Mechanics*, 34(3):541–547, 1967. ISSN 0021-8936. URL `https://doi.org/10.1115/1.3607741`.

[50] J. Kriegseis, P. Mattern, and M. Dues. Combined planar piv and lda profile-sensor measurements in a rotor-stator disk configuration. *18th International Symposium on the Application of Laser and Imaging Techniques to Fluid Mechanics, Lisbon, Portugal, July 4-7,*, 2016. URL `http://ltces.dem.ist.utl.pt/lxlaser/lxlaser2016/finalworks2016/papers/01.11_3_268paper.pdf`.

[51] T. v. Kármán. Über laminare und turbulente reibung. *ZAMM - Journal of Applied Mathematics and Mechanics / Zeitschrift für Angewandte Mathematik und Mechanik*, 1(4):233–252, 1921. URL `https://onlinelibrary.wiley.com/doi/abs/10.1002/zamm.19210010401`.

[52] C. J. Kähler, S. Scharnowski, and C. Cierpka. On the uncertainty of digital PIV and PTV near walls. *Experiments in Fluids*, 52(6):1641–1656, 2012. URL `https://doi.org/10.1007/s00348-012-1307-3`.

[53] J. König, K. Tschulik, L. Büttner, M. Uhlemann, and J. Czarske. Analysis of the electrolyte convection inside the concentration boundary layer during structured electrodeposition of copper in high magnetic gradient fields. *Analytical Chemistry*, 85(6):3087–3094, 2013. URL `https://doi.org/10.1021/ac302601t`.

[54] G. N. Lance and M. H. Rogers. The axially symmetric flow of a viscous fluid between two infinite rotating disk. *Proceedings of the Royal Society of London. Series A, Mathematical and Physical Sciences*, 266 (1324):109–121, 1962. ISSN 00804630. URL `http://www.jstor.org/stable/2414223`.

[55] B. Launder, S. Poncet, and E. Serre. Laminar, transitional, and turbulent flows in rotor-stator cavities. *Annual Review of Fluid Mechanics*, 42(1):229–248, 2010. URL `https://doi.org/10.1146/annurev-fluid-121108-145514`.

[56] F. A. Lloyd. Parameters contributing to power loss in disengaged wet clutches. *SAE Transactions*, 83:2498–2507, 1974. ISSN 0096736X, 25771531. URL `http://www.jstor.org/stable/44657508`.

[57] H. G. Maas, A. Gruen, and D. Papantoniou. Particle tracking velocimetry in three-dimensional flows. *Experiments in Fluids*, 15(2):133–146, 1993. URL `https://doi.org/10.1007/bf00190953`.

[58] C. D. Meinhart, S. T. Wereley, and J. G. Santiago. PIV measurements of a microchannel flow. *Experiments in Fluids*, 27(5):414–419, 1999. URL `https://doi.org/10.1007/s003480050366`.

[59] M. Mendez, M. Raiola, A. Masullo, S. Discetti, A. Ianiro, R. Theunissen, and J.-M. Buchlin. Pod-based background removal for particle image velocimetry. *Experimental Thermal and Fluid Science*, 80:181 – 192, 2017. ISSN 0894-1777. URL `https://doi.org/10.1016/j.expthermflusci.2016.08.021`.

[60] G. Morrison, M. Johnson, D. Swan, and R. Deotte. Advantages of orthogonal and non-orthogonal three-dimensional anemometer systems. *Flow Measurement and Instrumentation*, 2(2):89–97, 1991. ISSN 0955-5986. URL `https://www.sciencedirect.com/science/article/pii/095559869190016K`.

[61] T. Neupert and D. Bartel. High-resolution 3d cfd multiphase simulation of the flow and the drag torque of wet clutch discs considering free surfaces. *Tribology International*, 129:283 – 296, 2019. URL `https://doi.org/10.1016/j.triboint.2018.08.031`.

[62] T. Neupert, E. Benke, and D. Bartel. Parameter study on the influence of a radial groove design on the drag torque of wet clutch discs in comparison with analytical models. *Tribology International*, 119: 809–821, 2018. ISSN 0301679X. URL `https://doi.org/10.1016/j.triboint.2017.12.005`.

[63] N. Nishino, N. Kasagi, and M. Hirata. Three-dimensional particle tracking velocimetry based on automated digital image processing. *Journal of Fluids Engineering*, 111(4):384–391, 1989. URL `https://doi.org/10.1115/1.3243657`.

[64] W. Novak, J. Ryborz, P. Fietkau, B. Bertsche, and H. Naunheimer. *Fahrzeuggetriebe*. Springer-Verlag GmbH, Heidelberg, Germany, 2019. URL `https://www.ebook.de/de/product/37605951/wolfgang_novak_joachim_ryborz_peter_fietkau_bernd_bertsche_harald_naunheimer_fahrzeuggetriebe.html`.

[65] C. Oerleke and W. Funk. LeerlaufverhaIten ölgekühlter Lamellenkupplungen - Abschlußbericht. *Forschungsvorhaben 290 Lamellenkupplungen - FVA-Forschungsreport*, Berichtzeitraum 1995 - 1998, 2000.

[66] C. Oerleke and W. Funk. Einflußgrößen auf die Schleppmomente schnelllaufender Lamellenkupplungen in Automatengetrieben. *VDI-Berichte*, Nr. 1786:469–488, 2003.

[67] M. G. Olsen and R. J. Adrian. Out-of-focus effects on particle image visibility and correlation in microscopic particle image velocimetry. *Experiments in Fluids*, 29(7):S166–S174, 2000. URL `https://doi.org/10.1007/s003480070018`.

[68] K. L. Orloff and P. K. Snyder. Laser Doppler anemometer measurements using nonorthogonal velocity components: error estimates. *Appl. Opt.*, 21(2):339–344, 1982. URL `http://www.osapublishing.org/ao/abstract.cfm?URI=ao-21-2-339`.

[69] J. M. Owen and R. H. Rogers. *Flow and Heat Transfer in Rotating-Disc Systems, Rotor-Stator Systems.* Flow and Heat Transfer in Rotating-Disc Systems. John Wiley and Sons, Taunton, England/New York US, Research Studies Press, Ltd., 1989. ISBN 9780863800900. URL `https://books.google.de/books?id=SNZSAAAAMAAJ`.

[70] S. Pahlovy, S. Mahmud, M. Kubota, M. Ogawa, and N. Takakura. Multiphase drag modeling for prediction of the drag torque characteristics in disengaged wet clutches. *SAE International Journal of Commercial Vehicles*, 7(2):441–447, 2014. URL `https://doi.org/10.4271/2014-01-2333`.

[71] S. Pahlovy, S. Mahmud, M. Kubota, M. Ogawa, and N. Takakura. Prediction of drag torque in a disengaged wet clutch of automatic transmission by analytical modeling. *Tribology Online Japanes Society of Tribologists*, 11(2):121–129, 2016. URL `https://doi.org/10.2474/trol.11.121`.

[72] S. Pahlovy, S. Mahmud, M. Kubota, M. Ogawa, and N. Takakura. Development of an analytical model for prediction of drag torque characteristics of disengaged wet clutches in high speed region. In *SAE Technical Paper Series*, SAE Technical Paper. SAE International400 Commonwealth Drive, Warrendale, PA, United States, 2017. doi: 10.4271/2017-01-1132. URL `https://doi.org/10.4271/2017-01-1132`.

[73] F. Pereira, J. Lu, E. Castaño-Graff, and M. Gharib. Microscale 3d flow mapping with µDDPIV. *Experiments in Fluids*, 42(4):589–599, 2007. URL `https://doi.org/10.1007/s00348-007-0267-5`.

[74] A. E. Perry and M. S. Chong. A description of eddying motions and flow patterns using critical-point concepts. *Annual Review of Fluid Mechanics*, 19:125–155, 1987. URL `https://doi.org/10.1146/annurev.fl.19.010187.001013`.

[75] A. K. Prasad. Stereoscopic particle image velocimetry. *Experiments in Fluids*, 29(2):103–116, 2000. URL `https://doi.org/10.1007/s003480000143`.

[76] A. K. Prasad, R. J. Adrian, C. C. Landreth, and P. W. Offutt. Effect of resolution on the speed and accuracy of particle image velocimetry interrogation. *Experiments in Fluids*, 13:105–116, 1992. URL `https://doi.org/10.1007/BF00218156`.

[77] M. Raffel, C. E. Willert, F. Scarano, C. J. Kähler, S. T. Wereley, and J. Kompenhans. *Particle Image Velocimetry - A Practical Guide.* Springer International Publishing, Heidelberg, Germany, 2018. ISBN 3319688529. URL `https://doi.org/10.1007/978-3-319-68852-7`.

[78] G. Rao. *Modellierung und Simulation des Systemverhaltens nasslaufender Lamellenkupplungen.* Dissertation (in german), Technische Universität Dresden, Dresden, 2010. URL `https://nbn-resolving.org/urn:nbn:de:bsz:14-qucosa-77098`.

[79] J. Rockström, W. Steffen, K. Noone, Å. Persson, F. S. Chapin III, E. Lambin, T. M. Lenton, M. Scheffer, C. Folke, H. J. Schellnhuber, et al. Planetary boundaries: exploring the safe operating space for humanity. *Ecology and society*, 14(2), 2009. URL `https://www.ecologyandsociety.org/vol14/iss2/art32/`.

[80] J. Rockström, W. Steffen, K. Noone, Å. Persson, F. S. Chapin, E. F. Lambin, T. M. Lenton, M. Scheffer, C. Folke, H. J. Schellnhuber, B. Nykvist, C. A. de Wit, T. Hughes, S. van der Leeuw, H. Rodhe, S. Sörlin, P. K. Snyder, R. Costanza, U. Svedin, M. Falkenmark, L. Karlberg, R. W. Corell, V. J. Fabry, J. Hansen, B. Walker, D. Liverman, K. Richardson, P. Crutzen, and J. A. Foley. A safe operating space for humanity. *Nature*, 461(7263):472–475, 2009. URL `https://doi.org/10.1038/461472a`.

[81] B. Ruck. *Laser-Doppler-Anemometrie.* AT-Fachverlag, Stuttgart, Germany, 1987. ISBN 3921681006. (in German).

[82] P. G. Saffman. *Vortex Dynamics.* Cambridge Monographs on Mechanics. Cambridge University Press, Cambridge, United Kingdom, 1993. URL `https://doi.org/10.1017/CBO9780511624063`.

[83] C. W. Schade. Effects of transmission fluid on clutch performance. In *Farm, Construction and Industrial Machinery Meeting.* SAE International, feb 1971. URL `https://doi.org/10.4271/710734`.

[84] D. Schanz, A. Schröder, S. Gesemann, D. Michaelis, and B. Wieneke. 'Shake The Box': A highly efficient and accurate Tomographic Particle Tracking Velocimetry (TOMO-PTV) method using prediction of particle positions. In *PIV13; 10th International Symposium on Particle Image Velocimetry – ISPIV.* Conference proceedings, TU Delft, Delft, 2013. URL `http://resolver.tudelft.nl/uuid:212b0c2d-3210-482f-b751-91d98d5ea43d`.

[85] D. Schanz, S. Gesemann, and A. Schröder. Shake-The-Box: Lagrangian particle tracking at high particle image densities. *Experiments*

in Fluids, 57(5), 2016. URL `https://doi.org/10.1007/s00348-016-2157-1`.

[86] S. Scharnowski and C. J. Kähler. Particle image velocimetry - Classical operating rules from today's perspective. *Optics and Lasers in Engineering*, 135:106185, 2020. ISSN 0143-8166. doi: https://doi.org/10.1016/j.optlaseng.2020.106185. URL `https://www.sciencedirect.com/science/article/pii/S0143816619318287`.

[87] H. Schlichting and K. Gersten. *Boundary-Layer Theory*. Springer Berlin, Heidelberg, Germany, 2017. URL `https://doi.org/10.1007/978-3-662-52919-5`.

[88] P. N. Shankar and M. D. Deshpande. Fluid mechanics in the driven cavity. *Annual Review of Fluid Mechanics*, 32(1):93–136, 2000. URL `https://doi.org/10.1146/annurev.fluid.32.1.93`.

[89] K. Shirai, C. Bayer, A. Voigt, T. Pfister, L. Büttner, and J. Czarske. Near-wall measurements of turbulence statistics in a fully developed channel flow with a novel laser doppler velocity profile sensor. *European Journal of Mechanics - B/Fluids*, 27(5):567–578, 2008. ISSN 0997-7546. doi: 10.1016/j.euromechflu.2007.12.001. URL `https://www.sciencedirect.com/science/article/pii/S0997754607001124`.

[90] K. Shirai, Y. Yaguchi, L. Büttner, J. Czarske, and S. Obi. Highly spatially resolving laser doppler velocity measurements of the tip clearance flow inside a hard disk drive model. *Experiments in Fluids*, 50(3):573–586, 2011. URL `https://doi.org/10.1007/s00348-010-0959-0`.

[91] K. Shirai, L. Büttner, S. Obi, and J. Czarske. An experimental study on the flow behavior near the read-and-write arm in a hard disk drive model with a shroud opening. *Microsystem Technologies*, 19(9):1519–1527, 2013. URL `https://doi.org/10.1007/s00542-013-1847-3`.

[92] J. H. Spurk and N. Aksel. *Fluid Mechanics*. Springer International Publishing, Heidelberg, Germany, 2020. URL `https://doi.org/10.1007/978-3-030-30259-7`.

[93] W. S. G. (Student). The probable error of a mean. *Biometrika*, 6 (1):1–25, 1908. ISSN 00063444. URL `http://www.jstor.org/stable/2331554`.

[94] Y. Takagi, Y. Okano, M. Miyayaga, and N. Katayama. Numerical and physical experiments on drag torque in a wet clutch. *Tribology Online*, 7(4):242–248, 2012. URL `https://doi.org/10.2474/trol.7.242`.

[95] M. Tauviqirrahman, R. Ismail, J. Jamari, and D. J. Schipper. A study of surface texturing and boundary slip on improving the load support of lubricated parallel sliding contacts. *Acta Mechanica*, 224:365 – 381, 2013. URL `https://doi.org/10.1007/s00707-012-0752-7`.

[96] C. Tropea. Laser doppler anemometry: recent developments and future challenges. *Measurement Science and Technology*, 6(6):605–619, 1995. URL `https://doi.org/10.1088/0957-0233/6/6/001`.

[97] C. Tropea, A. L. Yarin, and J. F. Foss, editors. *Springer Handbook of Experimental Fluid Mechanics*. Springer Berlin, Heidelberg, Germany, 2007. URL `https://doi.org/10.1007/978-3-540-30299-5`.

[98] UNFCCC. Paris Agreement - United Nations, Dez. 2015. URL `https://treaties.un.org/pages/ViewDetails.aspx?src=TREATY&mtdsg_no=XXVII-7-d&chapter=27&clang=_en`. UNTC Treaty No XXVII 7.d.

[99] C. E. Willert and M. Gharib. Three-dimensional particle imaging with a single camera. *Experiments in Fluids*, 12(6):353–358, 1992. ISSN 1432-1114. URL `https://doi.org/10.1007/BF00193880`.

[100] M. Wu, J. W. Roberts, and M. Buckley. Three-dimensional fluorescent particle tracking at micron-scale using a single camera. *Experiments in Fluids*, 38(4):461–465, 2005. URL `https://doi.org/10.1007/s00348-004-0925-9`.

[101] W. Wu, B. Xiao, J. Hu, S. Yuan, and C. Hu. Experimental investigation on the air-liquid two-phase flow inside a grooved rotating-disk

system: Flow pattern maps. *Applied Thermal Engineering*, 133:33–38, 2018. ISSN 1359-4311. URL `https://www.sciencedirect.com/science/article/pii/S1359431117320628`.

[102] L. P. Yarin. *The Pi-theorem : applications to fluid mechanics and heat and mass transfer*. Experimental fluid mechanics. Springer Berlin, Heidelberg, Germany, 2012. ISBN 9783642195648; 3642195644. URL `https://doi.org/10.1007/978-3-642-19565-5`.

[103] Y. Yeh and H. Z. Cummins. localized fluid flow measurements with an He–Ne laser spectrometer. *Applied Physics Letters*, 4(10):176–178, 1964. URL `https://doi.org/10.1063/1.1753925`.

[104] S. Y. Yoon and K. C. Kim. 3d particle position and 3d velocity field measurement in a microvolume via the defocusing concept. *Measurement Science and Technology*, 17(11):2897–2905, 2006. URL `https://doi.org/10.1088/0957-0233/17/11/006`.

[105] Y. Yuan, E. A. Liu, J. Hill, and Q. Zou. An improved hydrodynamic model for open wet transmission clutches. *Journal of Fluids Engineering*, 129(3):333, 2007. URL `https://doi.org/10.1115/1.2427088`.

[106] X. Zhou. *Study of drag torque in a two-speed dual clutch transmission electric vehicle powertrain system*. PhD thesis, UTS-University of Technology Sydney, Sydney, 2014. URL `https://opus.lib.uts.edu.au/handle/10453/30336`.